Microfabricated and Micromolded 3D Retinal Scaffolds for Reconstruction of Outer Retina: Designs, Materials, Fabrications, and Optimizations

By

Inkyu Lee

A dissertation submitted in partial fulfillment of

the requirements for the degree of

Doctor of Philosophy

(Electrical Engineering)

at the

UNIVERSITY OF WISCONSIN-MADISON

2021

Date of final oral examination: 09/17/2021

The dissertation is approved by the following members of the Final Oral Committee:

Zhenqiang Ma, Professor, Electrical and Computer Engineering

Shaoqin Gong, Professor, Biomedical Engineering

Hongrui Jiang, Professor, Electrical and Computer Engineering

David M. Gamm, Associate Professor, Ophthalmology and Visual Sciences

Dedicated to everyone who has supported me through my years at the UW-Madison

Acknowledgement

It has been a fabulous journey at the University of Wisconsin-Madison for the last five years. My life has changed a lot since I came here in Madison in 2016 and all the experiences I have had made me grow one step further not only as a scholar, but also as a person.

There are many people I would like to thank. First of all, I would like to express my deepest gratitude to my advisor, Professor Zhenqiang (Jack) Ma, who has supported me and given me helpful advice throughout my doctoral course. The passion and efforts towards research that he has shown inspired and motivated me to work harder and further focus on my research to achieve my goals during my doctoral course. I also would like to say thank you to my co-advisor, Professor Shaoqin (Sarah) Gong, and a wonderful collaborator, Professor David Gamm, for their insightful perspective and guidance that they have shown for the last 4 years in our collaborative research. I believe that the lessons from them are invaluable for me and will be extremely helpful for when I work with others from different research fields from mine in the future. Furthermore, I would like to thank Professor Hongrui Jiang, who is one of my committee members, for his meaningful feedback and discussion on completing my degree. I hope to have the opportunity to build upon our current relationship and also further discuss new research topics in the future.

I am also grateful to my wonderful colleagues in my research group: Dr. Hyungsoo Kim, Dr. Jisoo Kim, Dr. Jihye Bong, Dr. Jeongpil Park, Dr. Sang June Cho, Dr. Kwangeun Kim, Dr. Tong June Kim, Dr. Yei Hwan Jung, Dr. Huilong Zhang, Dr. Dong Liu, Dr. Zhenyang Xia, Wei Lin, Jiarui Gong, Shuoyang Qiu, Jie Zhou, Donghyeok Kim, Hokyung Jang, and Daniel Vincent. I'm much obliged to you all for everything you all have done for me. Special thanks go to Dr. Juhwan Lee, Seunghwan Min, Dr. Ruosen (Alex) Xie, Dr. Allison Ludwig, Dr. Agustin Madrigal,

Abstract

Recent advances in human pluripotent stem cell (hPSC) technology have enabled the generation of a virtually unlimited supply of any type of cell found in the human body. Thus, several new therapeutic strategies are now being investigated to treat degenerative retinal diseases, including age-related macular degeneration, Stargardt macular dystrophy, and retinitis pigmentosa. One promising strategy is to transplant hPSC-derived photoreceptors (PRs) or retinal pigment epithelium (RPE) cells into the subretinal space through a simple bolus injection. However, this approach is not adequate in order to address the underlying challenges in achieving a highly polarized and well organized outer retinal architecture as a uniform level of organization and polarization of cells cannot be attained via the bolus injection. Furthermore, this approach may lead to a disorganized cell mass and it carries the additional risk of cells refluxing into the vitreous cavity where they can have unintended and potentially severe consequences (e.g., epiretinal membrane formation). Moreover, the dissociated cell injection is difficult to control, precluding precise targeting of the focal areas of damage. Therefore, new technologies that enable donor cells to be delivered in a precise and well organized fashion need to be developed.

Tissue engineering scaffolds are three-dimensional (3D) constructs that provide the structural support for cell attachment and subsequent tissue development. Numerous scaffolds have been developed and utilized for various tissue engineering applications by providing an appropriate environment for the regeneration of functional tissues and organs. For instance, hydrogels, as injectable polymeric matrices, can enable the 3D growth of cells, albeit in an unorganized fashion. Solid and porous polymer thin films have also been explored for tissue engineering

applications. However, retinal scaffolds—particularly, PR scaffolds with 3D micropatterned structures with feature sizes below 20 µm—can hardly be found in the literature until our recent report in 2018 on a wine glass-shaped PR scaffold made of biocompatible and biodegradable elastomer films, such as poly(glycerol-sebacate), also known as PGS, fabricated via a unique microfabrication process coupled with a micromolding process. The diameter of the "through hole" in our wine-glass PR scaffold was only 5 µm and the space between the cell reservoirs was 1 µm. The lack of a well-defined micropatterned scaffold was attributed to the following: (a) current scaffold fabrication techniques, such as solvent casting or 3D printing, are unable to produce highly-organized 3D microstructured patterning with sufficient resolution (e.g., with a feature size below 10 µm), and (b) the complexity required for cell patterning and transplantation has yet to be achieved. Commonly reported tissue-engineering scaffolds typically have feature sizes on a sub-millimeter scale, and they often consist of disorganized pores incapable of promoting PR polarization. Another major limiting factor is that most polymeric biomaterials are incompatible with conventional multi-step microfabrication processes involving the organic solvents and high temperatures that are required in order to produce complex, highly ordered 3D structures at a microscale level.

In 2018, our collaborative team engineered the first-generation PR scaffold with a 3D micropatterned wine glass design. To achieve highly organized 3D wine glass-shaped microstructures on biodegradable and biocompatible polymer films with micron-sized features (e.g., 5 µm), we developed a micromolding technique that can transfer lithographically defined micropatterns, produced via cutting-edge microfabrication techniques, to flexible polymer films. The wine glass-shaped PR scaffold provided for the capture of PRs, as well as guidance of PR basal axon extensions. However, this design did not support the close association of multiple

layers of hPSC-PRs and, overall, demonstrated a high burden of synthetic biomaterial relative to the cell payload. Furthermore, as of yet, there is no study for delivering PR+RPE bilayer on a single scaffold, which is required to treat advanced AMD, the last stage of macular degeneration. Therefore, a need exists for strategies to deliver both dense populations of PRs alone and in combination with RPE cells to a discrete region of the retina, particularly for macular diseases that affect high-acuity central vision such as AMD.

In this dissertation, in an effort to address these challenges, two types of tissue engineering scaffolds, an "ice cube tray"-shaped PR scaffold (discussed in Chapter 2) and a "honeycomb"-shaped outer retinal scaffold (discussed in Chapter 3), are introduced. More specifically, while the ice cube tray scaffold is designed as a second-generation scaffold to deliver high-density PRs and to reduce the overall biomaterial burden (i.e., the volume of biomaterial used to generate a single scaffold), the honeycomb scaffold, as a third-generation scaffold, is designed to deliver a dual construct of PRs and RPE cells and further improve the production yield of scaffold fabrication. In each chapter, simultaneous development and optimization of (1) the morphology (i.e., shape and sizes) of the scaffold design, (2) the formulation and curing process of the scaffolding elastomers (i.e., materials optimization), and (3) the scaffold fabrication processes (i.e., good manufacturing practices (GMP)-compliant process development) are discussed in more depth.

Table of Contents

List of Figures

Chapter 1. Overview of stem cell delivery scaffold for retinal regenerative therapy

1.1. Introduction

The retina is a multi-layered sensory tissue located at the rear of the eye as shown in Figure 1.1, and at the outermost layer of the retina there exist specialized cells called photoreceptors (PRs), which consist of two types of cells: cones and rods.
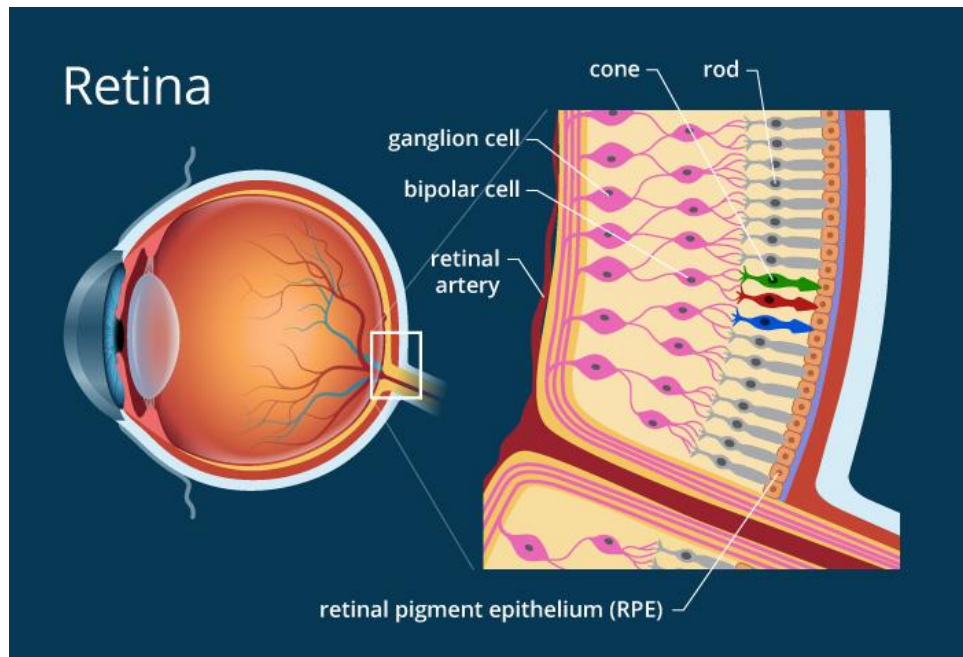
Figure 1.1. Anatomical features of the eye and layers of the retina as a drawing.[1]

These cells function by sensing light and/or color and delivering the signal back to the brain through the optic nerve. While cones detect color through bright light, rods are sensitive to low-light levels.[2] Rods aid in night vision and identifying black and white hues. While the PRs play a significant role in capturing and transducing photons into electro-chemical signals that travel along the optic nerve to the brain, retinal pigment epithelium (RPE) cells, located between the

PRs and the vascular choroid, closely interact with the PRs for the maintenance of visual function (i.e., delivering nutrients to the PRs from the choroid, and taking waste materials from the PRs and delivering them to the choroid). Interactions between both cell types are essential for visual function, thus they should be maintained in a highly organized fashion for the preservation of healthy vision.

All blinding disorders of the outer retina involve the dysfunction and loss of PRs, either alone (as occurs in many forms of retinitis pigmentosa (RP)) or with the involvement of the RPE cells (as found with the prevalent disorder, age-related macular degeneration otherwise known as AMD) as shown in Figure 1.2, and these types of retinal degenerative diseases result in visual impairment and eventually blindness.[2]
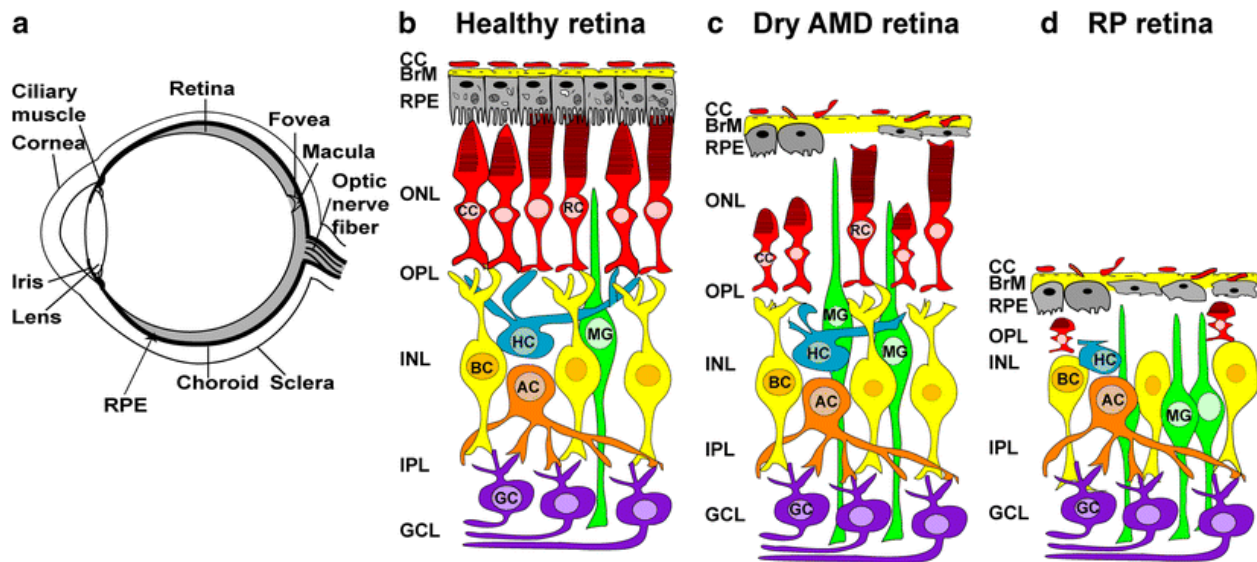
Figure. 1.2. (a) Schematic illustration of a cross-section through a human eye. (b) Schematic diagram of healthy retinal circuits. Mammalian retina consists of six major types of neuronal cells – rod cells (RC) and cone cells (CC), horizontal cells (HC), bipolar cells (BC), amacrine cells (AC) and retinal ganglion cells (RGC). The Müller cell (MC) are the glial cell that span

across the retina and their somata. RPE provides metabolic and transport functions essential for homeostasis of the neural retina. Bruch's membrane (BrM) is a highly specialized and multi-laminar structure separating RPE from the choroid and mediates exchange of oxygen and nutrients between vasculature of choroid and neural retina. RPE and the Bruch's membrane form the outer blood–retinal barrier. Choroidal capillaries (CC) are the blood capillaries present in choroid that supply oxygen and nourishment to the outer layer of the retina. (c) Schematic diagram of dry AMD retinal circuit. In Dry AMD, there is progressive atrophy of RPE, BrM and choriocapillaris (CC) in the macula. As a result, RPE cells stop providing support functions and the PRs in the macula die, resulting in a loss of central vision. (d) Schematic diagram of RP retinal circuit: In RP, rod PRs die, which trigger dramatic changes in the morphology of second order neurons (horizontal cells, bipolar cells and amacrine cells). As a result of the rapid rod degeneration, rod-driven bipolar and horizontal cell axon terminals retract their fine dendrites, and rod bipolar cell axon terminals assume immature synaptic structures. Defects extend to the cone circuit during the late phase of degeneration.[3]

According to The Macular Degeneration Partnership, the number of patients suffering from AMD to date has been continuously on the rise with an estimate of 200,000 new diagnoses annually[4, 5] and is expected to continue to rise in the future due to the rapidly aging global population (e.g., As stated by the Bright Focus Foundation, as many as 11 million people in the United States have some form of AMD[6] and this number is expected to double to nearly 22 million by 2050[7, 8]). However, despite the prevalence and serious nature of the disease, definitive cures for AMD (i.e., replacement of lost PRs and/or RPE cells) have not been developed yet.

This chapter provides a current account of the developments in retinal regeneration. Retinal

regeneration including gene- and cell-based therapies and tissue engineering approaches will be covered in the following sections. In particular, the regeneration techniques of PRs along with RPE cells will be discussed as they are the cells mainly involved in the majority of pathologies inducing blindness.

1.2. Degenerative retinal diseases

Retinal diseases widely vary in terms of symptoms, diagnosis, and treatment. Some of the most common retinal diseases include AMD, RP, Stargardt's disease, Retinal Tears, Macular Holes, Retinal Detachment, Diabetic Retinopathy, etc. Two retinal diseases that ultimately lead to blindness are "AMD," the most common cause of legal blindness among older Americans, and "RP," a rarer, inherited disease, and treatment options for them are currently limited. These diseases are caused by the degeneration of the retina over time. For this reason, they are appropriate targets for strategies of retinal regenerative therapy.

1.2.1. Age-related macular degeneration (AMD)

AMD is the top cause of vision loss in people over 50. More than 11 million people in the U.S. have some form of AMD, and this number is expected to reach almost 22 million by 2050 due to the increasing size of the elderly population. The disease is the result of genetic and environmental factors, and it gradually results in the loss of sharp, central vision with age. The loss of central vision occurs due to degeneration of the macula, the center of the retina that allows one to see detail, as shown in Figure 1.3.[9] A common symptom of AMD is the presence of drusen, or yellow deposits under the retina around the macular region. Although the AMD does not result in pain, the effects on vision can severely affect the quality of life.
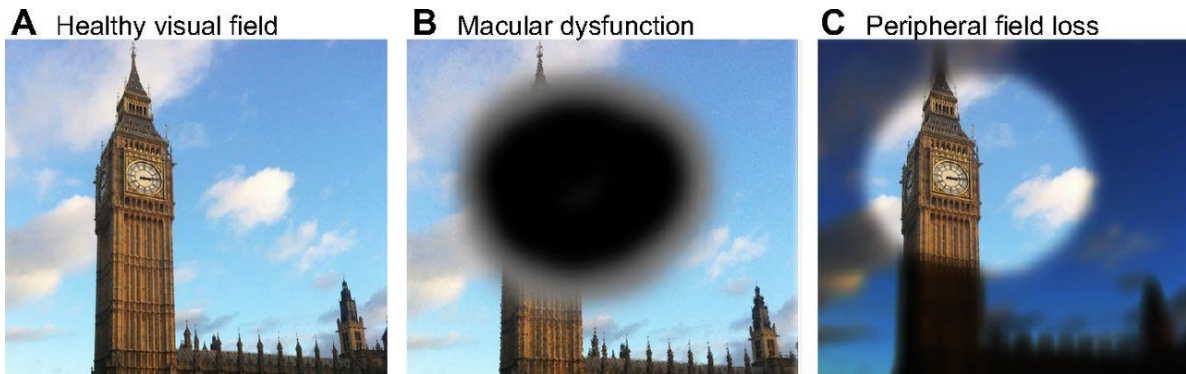
Figure 1.3. *The effects of RPE damage on visual field. (A) The visual fields in normal subjects. (B) The visual field in the case of macular diseases, such as AMD and Stargardt's disease. (C) The tunnel visual field experienced in individuals with RP.*[9]

There are two types of AMD, dry AMD and wet AMD. 90% of patients with AMD suffer from the dry form of the disease, which involves the slow and gradual shrinkage of the retina and degeneration of retinal layers. The patients suffer severe visual handicaps due to the gradual loss of central vision. The remaining 10% of patients with AMD have the wet form of the disease. This type is much more serious, and 90% of those who have this form of AMD suffer from blindness. In wet AMD, new blood vessels grow under the retina and leak blood and fluid. This fluid permanently damages the light-sensitive retinal cells and results in central vision loss. Factors associated with AMD are aging, obesity, heredity, hypertension, smoking, lighter eye color, and drug side effects. There is currently no cure for AMD and no way to completely stop its development. However, there are some treatments that may slow the progression of disease. There is no FDA-approved treatment for dry AMD, but Vitamins A, C, E, and other nutritional supplements, as well as sunglasses with UV protection, may slow its progression. Treatments for wet AMD that are aimed at stopping abnormal blood vessel growth include FDA-approved drugs Lucentis, Macugen, Avastin, and Visudyne used with Photodynamic Therapy.

1.2.2. Retinitis pigmentosa (RP)

RP is the most common inherited cause of blindness in people between the ages of 20 and 60 worldwide.[10, 11] Around 500,000 people in the United States suffer some level of visual impairment from RP, and, of those, 20,000 are totally blind. RP is a degenerative disease of the retina that affects the PRs, particularly rod cells, which control a person's ability to see in dimly lit surroundings as shown in the Figure 1.3c.[9, 12] Vision loss is gradual and may result in diminished or lost peripheral vision or blindness. Similar to dry AMD, there are currently no treatments available for RP,[12] although supplements of Vitamin A may delay the vision loss. Individuals with RP might also consider using low vision devices that help to magnify and illuminate objects. Clearly, there is a need for treatment of retinal diseases that deteriorate PR cells and result in blindness. Although no visually beneficial treatments exist for AMD and RP, a number of approaches are under investigation, including the development of cell-scaffold composites for tissue engineering. RPE transplants and retinal prosthesis are also being developed to enhance retinal function in patients suffering from retinal degenerative disease.

1.2.3. Potential therapies to address vision loss affecting the outer retina

Current therapies under investigation for blinding disorders include cell replacement therapy, gene therapy, optogenetics, and bionic prosthetics. However, each therapy has its limitations. Gene therapy aims to treat inherited disease only at stages preceding RPE or PR cell death, and is therefore not suitable for patients with substantial cell loss. Optogenetics and prosthetics bypass PRs altogether, but are primarily end stage interventions in patients who have no or bare light perception, as opposed to macular vision loss alone. For optogenetics in particular, little is known about the potential visual impact of coercing cell types other than PRs, such as bipolar

cells or ganglion cells, to become artificially light sensitive, since most or all of the horizontal and vertical processing that takes place within the retina is not engaged with this approach. The same is true for visual prosthetics, where bionic chips translate light into an electrical signal to stimulate downstream neurons. With this approach, rudimentary visual percepts can be generated (i.e. phosphenes), but it is not currently possible to restore higher acuity vision. Unlike these other approaches, outer retina cell replacement therapy has the potential to treat blinding outer retinal disease and injury as it offers the opportunity to directly replace the PRs and/or RPE cells that are damaged or lost, assuming that high purity, authentic human PRs and RPE can be produced and safely and accurately delivered to the area of injury.

1.3. Human pluripotent stem cell (hPSC) technology

hPSCs have the ability to generate all cell types present in adult organisms, therefore harboring great potential for the in vitro study of differentiation and for the development of cell-based therapies. hPSCs provide a novel and promising source of biological material for modeling retinal development and devising cell-based treatments for degenerative retinal diseases. hPSCs can be differentiated to form all PR subtypes, including rods and short, medium, and long wavelength cones. Following several months of maturation, hPSC-PRs polarize to form axon terminals and inner and outer segments, have a gene expression profile comparable to native human PRs, possess a characteristic electrophysiological signature, and respond to light stimulation. Likewise, hPSC-RPE cells form a polarized, fully functional monolayer, with demonstrated capabilities for polarized growth factor secretion, PR outer segment phagocytosis, waste and water removal, retinoid recycling, and tight junction formation.

Several clinical trials using hPSC-RPE are currently underway for the treatment of AMD.

However, currently, there is no bona fide hPSC-PR therapy in clinical trials. Several Phase I/IIa clinical studies are ongoing in the US and abroad to investigate potential cell therapies for the treatment PR-based disorders such as RP; however, these studies involve the transplantation of non-PR cell types, including fetal retinal progenitor cells (RPCs) and mesenchymal stem cells, for which the potential mechanism of action is unknown and presumed to be delivery of trophic molecules rather than direct replacement of degenerated PRs.

1.4. Current status of retinal cell replacement therapy

Retinal degeneration due to the dysfunction and loss of PRs, either alone or in combination with RPE cells, is currently untreatable. However, there are several therapies in development that utilize diverse strategies. These therapies include the delivery of stem cells or progenitor cells to the outer retina, via injection of cell suspensions or based on tissue engineering scaffolds.

1.4.1. Delivery of cell suspensions via an injection

The injection of cell suspensions (e.g., PRs or RPE cells) into the subretinal space is a very simple and fast way to replace degenerating or dysfunctional cells. [13] However, delivering cell suspensions into the subretinal space by injection does not lead to high levels of cell survival due to the shear forces involved in the process.[14] Furthermore, it often suffers from reflux during transplantation, poor cell survival, disorganization, migration, and differentiation to restore visual function to a level measurable in animal models by electroretinography (ERG). Thus, in reality, the bolus injection of cells is not considered an ultimate solution to treat retinal degeneration.

1.4.2. Cell delivery on a scaffold

Tissue engineering scaffolds are three-dimensional (3D) constructs that provide the structural support for cell attachment and subsequent tissue development. In the last two decades, research has found that delivering the cells on a scaffold improves cell survival and differentiation ability. A cornerstone of tissue engineering is the design of scaffolds on which cells can be cultured and the subsequent delivery of the cell-scaffold composite to the relevant location of degeneration. In the case of retinal tissue engineering, stem cells or RPCs are cultured on scaffolds and transplanted to the subretinal space. It is theorized that this process promotes cell survival, integration, and differentiation. However, in order to be used in transplantation, the scaffold must be biocompatible and mechanically compatible with the retina. Many recent advances in material processing and fabrication enable precise control of the scaffold design and material properties to imitate natural tissue microenvironments. Regulation of properties including topography, adhesion molecules, and soluble factors enables better control of cell behavior and host tissue response.

The concept of cell delivery through a scaffold was further advanced by combining computer-aided design and microfabrication processing technologies to manipulate scaffold architecture, including parameters such as porosity and topography. Micro-electromechanical systems (MEMS) technology, a process technology used to create tiny integrated devices or systems that combine mechanical and electrical components, allows for more precise control of scaffold features and more uniform, reproducible pore size and shape. The micropatterned substrates can be designed to encourage cell attachment, migration, and differentiation into the appropriate phenotype. Moreover, the microfabrication processing allows for a scaffold design that is closer to the original retinal architecture, increasing the possibility of PR synapses

reconstruction. This technology has been applied to a variety of polymers to create scaffolds for RPC grafting.

One study evaluated the effects of non-degradable poly(methyl mathacrylate) (PMMA) scaffolds 6 µm thin on the survival, migration, and differentiation of RPCs.[15] It showed that porous micropatterned PMMA scaffolds demonstrate enhanced RPC adhesion and cell migration into the host retina as compared to smooth, non-porous scaffolds. Photolithography and reactive ion etching were used to make an 11 µm pore diameter with 63 µm in between pores. The study showed that even though porous and non-porous scaffold exhibit biocompatibility, cell survival, and adherence, the porous scaffold allows for better attachment of cells up to four weeks after transplantation to the subretinal space. Furthermore, the pores provided a stimulus from migration into the native retinal layers. The non-porous scaffolds had limited retention of RPCs. In another example of precisely designed pore structures, Neeley et al. fabricated a PGS scaffold for RPC grafting using standard microfabrication and replica molding techniques.[16] The scaffold, 45 µm in thickness, consisted of a uniform porous structure with 50 µm pores, approximately the thickness of the scaffold. It exhibited mechanical properties well suited for the retina, including Young's modulus (1.66 ± 0.23 MPa) and maximum elongation at failure of $113 \pm 22\%$. RPCs strongly adhered to the scaffold and proliferated. Immunohistochemistry revealed the presence of some mature cell markers at various time points after cell seeding, indicating cell differentiation. This study further demonstrated the ability of RPCs to attach to polymer scaffolds in the subretinal transplantation process as well as the potential of using a porous design. The cells are able to attach to the scaffold via cell anchorage mechanisms to the pores and embedment inside the pores. This also allows other surrounding RPCs to attach to the scaffold via cell-cell contact.

1.4.3. Disadvantages of current strategies

There are a number of disadvantages of the methods described above, warranting the need for further development of practical solutions for stem cell delivery to the subretinal space. As described above, bolus injection of stem cells has too many shear forces in the delivery process, thereby diminishing cell survival and proliferation. Thus, scaffolds are a necessary element of retinal regenerative therapy, but they should be able to carry a large number of cells and have an organized, defined structure. Bulk, porous scaffolds of various size pores can carry a large number of cells, but the cells are not able to migrate out of the scaffold easily. Cells are also distant from each other as well as from the host environment. These scaffolds are thick and may be disruptive to the native retinal tissue. Furthermore, they are not reproducible in design. Thin film 2-D platforms allow for enhanced cell migration out of the scaffold, but they are only able to carry a limited layer of cells. In addition, this layer can be sheared off relatively easily during the transplantation process. Clearly, there is a need for a precise, uniform device design that can hold a large number of cells and allow for cell survival and migration.

1.5. Scaffold fabrication techniques

1.5.1. Solvent casting

Solvent casting techniques have been widely used in ocular tissue engineering.[17] They consist of dissolving a polymer in a suitable solvent followed by casting and solvent evaporation.[18] The fabricated scaffold is a non-porous, homogeneous film. In retinal tissue engineering, these films were seeded with RPE cells in order to reconstruct the RPE layer and replace Bruch's membrane for AMD treatment, thus preventing PR loss.[19, 20] The prosthetic Bruch's membrane fabricated by solvent casting showed a similar thickness to the human

Bruch's membrane and facilitated implantation and orientation of the cellular graft in the subretinal space. Furthermore, as the polymer degraded, transplanted RPE cells re-established interactions with the natural Bruch's membrane.[19] The film surface was modified to improve the long-term survival of a functional RPE monolayer.[21, 22] Singh et al. fabricated silk fibroin scaffolds coated with type I collagen, which facilitated the development and survival of a functional RPE monolayer in vitro for 90 days.[21] Hasirci et al. utilized oxygen plasma treatment to make a film surface hydrophilic, thus improving cell attachment and spreading.[22] However, the non-porous structure of the film, did not match the open fibrillar structure of the original Bruch's membrane, which hindered nutrient diffusion from the choroid in vivo. In order to create a porous scaffold, a solvent casting/particle leaching (SC/PL) method was used in biomedical applications.[23] In the SC/PL technique, the solvent in which the polymer is dissolved contains porogens, which are leachable particles and used for making pores in molded structures.[24] This method enables the manufacture of high-porosity scaffolds (up to 93%) in a simple and cost-effective manner.[23] Using the SC/PL method, prosthetic Bruch's membranes were successfully created for RPE transplantation.[25, 26] Furthermore, the influence of scaffold pore size on cell differentiation into the retinal precursor has been studied in order to establish an improved cell therapy strategy.[27] However, the low reproducibility of the SC/PL technique makes it unsuited for retinal tissue engineering applications.[28]

1.5.2. Electrospinning

Electrospinning is another technique that has been explored in the field of retinal tissue engineering. The electrospinning process has been indicated as a promising technique in the fabrication of a prosthetic Bruch's membrane as it is able to recapitulate the nanofibrous structure

of a native Bruch's membrane.[29] Certainly, using the electrospinning technique the production of 3D thin nanofibrous membranes is possible by employing natural and synthetic polymers.[30] These fibrillar networks are highly permeable for solutes, and therefore enabling cell adhesion and proliferation[30] The morphological properties of electrospun membranes (i.e., thickness, fiber size, and orientation) can be fine-tuned through a simple change of the specific parameters of the electrospinning process including the polymer concentration, solution flow rate, and collector distance.[31]

Solution electrospinning has been used in order to generate a prosthetic Bruch's membrane for engineering an RPE layer. The hypothesis is that the RPE monolayer engineered on thin electrospun membranes could be used as an effective therapy for those who have blinding disorders or experience deficiencies associated with RPE and Bruch's membrane degeneration.

Synthetic and natural polymers such as poly(lacticacid) (PLA), Poly-ε-caprolactone (PCL) and poly(lactic-co-glycolic acid) (PLGA), silk fibroin and silk fibroin-PCL-gelatin were utilized for making electrospun Bruch's membrane-like scaffolds.[32-36] Usually, a blend of natural and synthetic materials is electrospun as synthetic polymers show outstanding mechanical properties and a controlled degradation rate, while pure naturally-derived polymers promote cell adhesion and proliferation. Warnke et al. succeeded in fabricating ultrathin nanofibrous scaffolds using collagen and PLGA, which closely imitated the structure of a natural Bruch's membrane.[32] Human RPE cells seeded onto these scaffolds formed a functional monolayer with a typical cobblestone morphology and abundant sheet-like microvilli on their apical surfaces. However, no conclusive results of the scaffold mechanics and permeability were reported.[32] Belgio et al. created a Bruch's membrane-like membrane composed of a blend of *Bombyx mori* silk fibroin and PCL for the purposes of studying the pathological mechanisms of AMD in a 3D in vitro

model.[36] The fabricated scaffolds displayed similarities with a human Bruch's membrane in regards to the architecture, mechanical properties, and permeability.[36] Through these in vitro studies, the feasibility of employing electrospun membranes as a prosthetic Bruch's membrane on which a functional RPE monolayer is formed were demonstrated. As such, RPE patches consisting of electrospun scaffolds, which were previously seeded with RPE cells, have been further studied in vivo. The RPE patches were demonstrated to be biocompatible when implanted in animal models without exhibiting any adverse reactions.[33, 34] In another study, Sharma et al. also accessed the functionality of clinical-grade iPSC-RPE patches, this time in rats and in a porcine laser-injured model.[24] From their findings, the use of the scaffolds improved the patch integration and efficacy over the cell suspension.[35] In fact, an increased PR preservation was encountered in animals transplanted with the patch in respect to those injected with the cell suspension. This study has led to a phase I/II clinical trial (NCT04339764) based on patch subretinal transplantation in patients suffering from advanced stages of dry AMD.

Despite many advantages of the electrospinning technique, it still has a limited microarchitecture controllability. In order to overcome this stumbling block, melt electrowriting (MEW) has been recently developed.[37] MEW enables the controlled deposition of a polymer melt fiber starting from a digital model, thus combining melt electrospinning and additive manufacturing principles. To date, this innovative method has been used in vascular, bone and skin tissue engineering, but there are currently no research on a retinal use.[38]

1.5.3. 3D printing

3D printing (sometimes referred to as Additive Manufacturing (AM)) technique has been brought into the tissue engineering field to address the lack of fine control of structural aspects. It

is the computer-controlled sequential layering of materials to create 3D shapes,[39] and thus allows of fabrication of complicated geometries with multimaterial parts.[39] 3D printing plays an important role in developing individualized treatments, surgical planning, and the testing deployment of devices in realistic pathways owing to its potential to produce patient-specific 3D structures in a cost- and time-effective way.[40]

3D bioprinting is the most recent promising progression of 3D printing in the medical sector. 3D bioprinting is a novel biofabrication approach that allows for the precise positioning of non-living materials, similar to 3D printing, and living materials in a prescribed 3D hierarchical organization.[41] 3D bioprinting aims for creating 3D bioengineered objects which can be used in regenerative medicine, pharmacokinetics, and basic cell biology research.[41] Such 3D bioprinted constructs can subsequently be cultured in bioreactor systems to obtain mature functional tissues and organs.[42] A few examples of 3D bioprinted scaffolds are represented by synthetic skin to be transplanted onto patients with burn injuries, heart valve replication, and bionic ears.[43-45] Currently, there are mainly three types of bioprinting systems−laser-based, inkjet-based, and extrusion-based technologies−characterized by a high deposition accuracy, stability, and cell viability. [41]

Laser-based technology utilizes a pulsed laser source and an optical path in order to focus a laser on a target from which bioink is printed and deposited onto a substrate. The target is composed of a glass slide, a metal slide, and bioink. The laser is focused through the glass slide onto the metal slide inducing a vaporization of the metal-absorbing layer, thus resulting in the production of a jet of bioink. Many researchers have demonstrated that cells were highly viable after laser-based 3D bioprinting.[46] However, cell placement accuracy can be challenging and, in addition, this technology is expensive and relatively slow.

Inkjet-based bioprinting is an inexpensive and simple to use technology while offering a relatively high resolution and cell viability.[46] In inkjet bioprinting, small droplets of bioink are ejected from a nozzle through microheater or piezoelectric systems and then dispensed onto a substrate.[46] Inkjet bioprinting was investigated to seed RGCs and glial cells. The technology did not affect the survival and the growth of rat RGCs and glial cells compared with cells seeded onto tissue culture plates.[47] This result opens the way for developing a printed construct to be used in retinal regeneration. Having said that, however, the use of inkjet-printed structures for tissue engineering is still limited by their low mechanical properties and their long term durability. Furthermore, clogging issues are common with viscous bioink owing to the presence of the nozzle.[46]

The extrusion-based technology relies on the extrusion of continuous filaments of bioink through a nozzle using a driving force, i.e., a piston, a screwing system or pneumatic pressure. It is the most versatile bioprinting process as it enables the printing of the broadest range of bioink viscosities.[46] Additionally, it allows clinically relevant constructs to be obtained in terms of size and shape. However, the rheological requirements of the bioink are stringent.[48] Extrusion-based bioprinting was investigated to produce a 3D in vitro model of the RPE and PR layers.[49] The RPE cell line was bioprinted with a precise pattern and allowed to form a monolayer in 14 days followed by the bioprinting of the PR cell line.[49] Such a bioprinted construct could be meaningful for biomedical applications such as disease research and high-throughput screening.

1.5.4. Microfabrication

Microfabrication is the technique of fabricating miniature structures on a micrometer-sized scale using a variety of fabrication processes such as photolithography, etching, and deposition.

The earliest microfabrication techniques were usually used for integrated circuit fabrication, but in the last decade, microfabrication has emerged as a promising alternative to the conventional manufacturing methods in the field of biomedicine.[50] Microfabrication allows the formation of precise and complex 2D and 3D micro- and nano-architectures, and the master fabricated by microfabrication can be employed to create a polymer negative mold typically of polydimethylsiloxane (PDMS) for a polymeric scaffold fabrication.[50] RPCs were successfully seeded onto structures fabricated through microfabrication.[16, 51, 52] The microfabricated topography enhanced the attachment, organization, and differentiation of the progenitor cells.[51] Hence, these structures could be used for PR replacement in the treatment of PR degeneration.

Lu et al. also developed a mesh-supported submicron parylene-C membrane as an artificial Bruch's membrane and tested it in vitro for an RPE cell culture as a potential treatment for dry AMD.[53] Furthermore, in vivo studies demonstrated the safety and potential of a parylene membrane as an RPE scaffold.[54] In particular, the implantation of the membrane previously seeded with cells was compared with the injection of a cell suspension. The results showed that cell survival was greater in animals that were transplanted with the cell membrane patch than those that received the cell suspension. Moreover, when injected, cells were observed as clumps whereas an RPE monolayer was visible in rats transplanted with the patch. These findings suggest that this approach may improve visual function at least in the short term in a few patients suffering from advanced stages of dry AMD. Currently, there is an ongoing clinical trial at phase I/IIa (NCT02590692) to study the safety of subretinal implantation of human embryonic stem cells seeded onto a parylene membrane.[55]

1.6. References

1. Heiting, G. The Retina: Where Vision Begins. 2019 [cited September 2, 2021] Available from: https://www.allaboutvision.com/resources/retina.htm

2. Barden, A. Photoreceptors and their function in the eye. 2021 [cited September 2, 2021] Available from: https://www.allaboutvision.com/eye-care/eye-anatomy/photoreceptors/

3. Singh, R. *et al.* Pluripotent stem cells for retinal tissue engineering: current status and future prospects. *Stem cell reviews and reports* **14,** 463-483 (2018).

4. Maguire, M. G. Comparing treatments for age-related macular degeneration: safety, effectiveness and cost. *LDI issue brief* **17,** 1-4 (2012).

5. Caroline R. Baumal, M. D. Wet Age-Related Macular Degeneration: Treatment Advances to Reduce the Injection Burden. *Supplements and Featured Publications* **26,** (2020).

6. Foundation, B. Age-Related Macular Degeneration: Facts & Figures. 2019 [cited September 2, 2021] Available from: https://www.brightfocus.org/macular/article/age-related-macular-facts-figures

7. He, W., Goodkind, D. & Kowal, P. R. An aging world: 2015. United States Census Bureau Washington, DC (2016).

8. Rein, D. B. *et al.* Forecasting age-related macular degeneration through the year 2050: the potential impact of new treatments. *Archives of ophthalmology* **127,** 533-540 (2009).

9. Ramsden, C. M. *et al.* Stem cells in retinal regeneration: past, present and future. *Development* **140,** 2576-2585 (2013).

10. Alswailmi, F. K. Global prevalence and causes of visual impairment with special reference to the general population of Saudi Arabia. *Pakistan journal of medical sciences* **34,** 751 (2018).

11. Hartong, D. T., Berson, E. L. & Dryja, T. P. Retinitis pigmentosa. *The Lancet* **368,** 1795-1809 (2006).

12. Parfitt, D. *et al.* The heat-shock response co-inducer arimoclomol protects against retinal degeneration in rhodopsin retinitis pigmentosa. *Cell death & disease* **5,** e1236-e1236 (2014).

13. Humayun, M. S. *et al.* Human neural retinal transplantation. *Investigative ophthalmology & visual science* **41,** 3100-3106 (2000).

14. Young, M. J. Stem cells in the mammalian eye: a tool for retinal repair. *Apmis* **113,** 845-857 (2005).

15. Tao, S. *et al.* Survival, migration and differentiation of retinal progenitor cells transplanted on micro-machined poly (methyl methacrylate) scaffolds to the subretinal space. *Lab on a Chip* **7,** 695-701 (2007).

16. Neeley, W. L. *et al.* A microfabricated scaffold for retinal progenitor cell grafting. *Biomaterials* **29,** 418-426 (2008).

17. Chirila, T. V., Barnard, Z., Harkin, D. G., Schwab, I. R. & Hirst, L. W. Bombyx mori silk fibroin membranes as potential substrata for epithelial constructs used in the management of ocular surface disorders. *Tissue Engineering Part A* **14,** 1203-1211 (2008).

18. Siemann, U. Solvent cast technology–a versatile tool for thin film production. *Scattering methods and the properties of polymer materials*. Springer, 2005, pp 1-14.

19. Giordano, G. G. *et al.* Retinal pigment epithelium cells cultured on synthetic biodegradable polymers. *Journal of Biomedical Materials Research: An Official Journal of The Society for Biomaterials and The Japanese Society for Biomaterials* **34,** 87-93 (1997).

20. Lai, J.-Y. & Li, Y.-T. Evaluation of cross-linked gelatin membranes as delivery carriers for retinal sheets. *Materials Science and Engineering: C* **30,** 677-685 (2010).

21. Galloway, C. A. *et al.* Characterization of human iPSC-RPE on a prosthetic Bruch's membrane manufactured from silk fibroin. *Investigative ophthalmology & visual science* **59,** 2792-2800 (2018).

22. Tezcaner, A., Bugra, K. & Hasırcı, V. Retinal pigment epithelium cell culture on surface modified poly (hydroxybutyrate-co-hydroxyvalerate) thin films. *Biomaterials* **24,** 4573-4583 (2003).

23. Prasad, A., Sankar, M. R. & Katiyar, V. State of art on solvent casting particulate leaching method for orthopedic scaffoldsfabrication. *Materials Today: Proceedings* **4,** 898-907 (2017).

24. Subia, B., Kundu, J. & Kundu, S. Biomaterial scaffold fabrication techniques for potential tissue engineering applications. *Tissue engineering* **524,** 142-157 (2010).

25. Shadforth, A. M., George, K. A., Kwan, A. S., Chirila, T. V. & Harkin, D. G. The cultivation of human retinal pigment epithelial cells on Bombyx mori silk fibroin. *Biomaterials* **33,** 4110-4117 (2012).

26. McHugh, K. J., Tao, S. L. & Saint-Geniez, M. Porous poly (ε-caprolactone) scaffolds for retinal pigment epithelium transplantation. *Investigative ophthalmology & visual science* **55,** 1754-1762 (2014).

27. Worthington, K. S., Wiley, L. A., Guymon, C. A., Salem, A. K. & Tucker, B. A. Differentiation of induced pluripotent stem cells to neural retinal precursor cells on porous poly-lactic-co-glycolic acid scaffolds. *Journal of Ocular Pharmacology and Therapeutics* **32,** 310-316 (2016).

28. Janik, H. & Marzec, M. A review: Fabrication of porous polyurethane scaffolds. *Materials Science and Engineering: C* **48,** 586-591 (2015).

29. Hotaling, N. A. *et al.* Nanofiber scaffold-based tissue-engineered retinal pigment epithelium to treat degenerative eye diseases. *Journal of Ocular Pharmacology and Therapeutics* **32,** 272-285 (2016).

30. Rahmati, M. *et al.* Electrospinning for tissue engineering applications. *Progress in Materials Science* **117,** 100721 (2021).

31. Beachley, V. & Wen, X. Effect of electrospinning parameters on the nanofiber diameter and length. *Materials Science and Engineering: C* **29,** 663-668 (2009).

32. Warnke, P. H. *et al.* Primordium of an artificial Bruch's membrane made of nanofibers for engineering of retinal pigment epithelium cell monolayers. *Acta biomaterialia* **9,** 9414-9422 (2013).

33. Xiang, P. *et al.* A novel Bruch's membrane-mimetic electrospun substrate scaffold for human retinal pigment epithelium cells. *Biomaterials* **35,** 9777-9788 (2014).

34. Surrao, D. C. *et al.* Design, development and characterization of synthetic Bruch's membranes. *Acta biomaterialia* **64,** 357-376 (2017).

35. Sharma, R. *et al.* Clinical-grade stem cell–derived retinal pigment epithelium patch rescues retinal degeneration in rodents and pigs. *Science translational medicine* **11,** (2019).

36. Belgio, B., Boschetti, F. & Mantero, S. Towards an In Vitro Retinal Model to Study and Develop New Therapies for Age-Related Macular Degeneration. *Bioengineering* **8,** 18 (2021).

37. Dalton, P. D. Melt electrowriting with additive manufacturing principles. *Current Opinion in Biomedical Engineering* **2,** 49-57 (2017).

38. Saidy, N. T. *et al.* Melt Electrowriting of Complex 3D Anatomically Relevant Scaffolds. *Frontiers in bioengineering and biotechnology* **8,** 793 (2020).

39. Gleadall, A., Visscher, D., Yang, J., Thomas, D. & Segal, J. Review of additive manufactured tissue engineering scaffolds: relationship between geometry and performance. *Burns & trauma* **6,** (2018).

40. Aimar, A., Palermo, A. & Innocenti, B. The role of 3D printing in medical applications: a state of the art. *Journal of healthcare engineering* **2019,** (2019).

41. Moroni, L. *et al.* Biofabrication strategies for 3D in vitro models and regenerative medicine. *Nature Reviews Materials* **3,** 21-37 (2018).

42. Mantero, S., Sadr, N., Riboldi, S., Lorenzoni, S. & Montevecchi, F. A new electro-mechanical bioreactor for soft tissue engineering. *Journal of Applied Biomaterials and Biomechanics* **5,** 107-116 (2007).

43. He, P. *et al.* Bioprinting of skin constructs for wound healing. *Burns & trauma* **6,** (2018).

44. Vukicevic, M., Mosadegh, B., Min, J. K. & Little, S. H. Cardiac 3D printing and its future directions. *JACC: Cardiovascular Imaging* **10,** 171-184 (2017).

45.   Mannoor, M. S. *et al.* 3D printed bionic ears. *Nano letters* **13,** 2634-2639 (2013).

46.   Li, J., Chen, M., Fan, X. & Zhou, H. Recent advances in bioprinting techniques: approaches, applications and future prospects. *Journal of translational medicine* **14,** 1-15 (2016).

47.   Lorber, B., Hsiao, W.-K., Hutchings, I. M. & Martin, K. R. Adult rat retinal ganglion cells and glia can be printed by piezoelectric inkjet printing. *Biofabrication* **6,** 015001 (2013).

48.   Schwab, A. *et al.* Printability and shape fidelity of bioinks in 3D bioprinting. *Chemical reviews* **120,** 11028-11055 (2020).

49.   Shi, P., Tan, Y. S. E., Yeong, W. Y., Li, H. Y. & Laude, A. A bilayer photoreceptor-retinal tissue model with gradient cell density design: a study of microvalve-based bioprinting. *Journal of tissue engineering and regenerative medicine* **12,** 1297-1306 (2018).

50.   Tran, K. T. & Nguyen, T. D. Lithography-based methods to manufacture biomaterials at small scales. *Journal of Science: Advanced Materials and Devices* **2,** 1-14 (2017).

51.   Steedman, M. R., Tao, S. L., Klassen, H. & Desai, T. A. Enhanced differentiation of retinal progenitor cells using microfabricated topographical cues. *Biomedical microdevices* **12,** 363-369 (2010).

52.   Redenti, S. *et al.* Engineering retinal progenitor cell and scrollable poly (glycerol-sebacate) composites for expansion and subretinal transplantation. *Biomaterials* **30,** 3405-3414 (2009).

53.   Lu, B., Zhu, D., Hinton, D., Humayun, M. S. & Tai, Y.-C. Mesh-supported submicron parylene-C membranes for culturing retinal pigment epithelial cells. *Biomedical microdevices* **14,** 659-667 (2012).

54.   Diniz, B. *et al.* Subretinal implantation of retinal pigment epithelial cells derived from human embryonic stem cells: improved survival when implanted as a monolayer. *Investigative ophthalmology & visual science* **54,** 5087-5096 (2013).

55.   Kashani, A. H. *et al.* A bioengineered retinal pigment epithelial monolayer for advanced, dry age-related macular degeneration. *Science Translational Medicine* **10,** (2018).

Chapter 2. Second generation ice cube tray-shaped scaffolds for high-density photoreceptor replacement

This chapter was previously published by the American Association for the Advancement of Science (AAAS).[1]

2.1. Introduction

Solid and porous polymeric thin film scaffolds supporting hPSC-derived neural retina cell growth have been developed in recent years to overcome problems inherent to bolus cell suspension injections.[2-13] Despite these advances, two of the core engineering challenges these scaffolds are intended to address—cell disorganization and low or unpredictable cell payloads—have remained largely unsolved. We recently developed a 'wineglass' design scaffold that succeeded in orienting a single layer of individually spaced hPSC-PRs.[13] However, this design did not support the close association of multiple layers of hPSC-PRs, and overall demonstrated a high burden of synthetic biomaterial relative to the cell payload. A need therefore exists for strategies to deliver dense populations of PRs to a discrete region of the retina, particularly for macular diseases that affect high-acuity central vision like AMD. With these primary engineering goals in mind, we developed an ultrathin biodegradable scaffold patterned with micron-level precision, constructed specifically to improve cell payload and reduce biomaterial burden (i.e., the volume of biomaterial used to generate a single 5-mm diameter scaffold with a thickness of 30 µm), while maintaining optimal mechanical properties for subretinal applications. Herein we describe 1) the development and optimization of the 3D microstructure shape and size (i.e., scaffold design), 2) the scaffold fabrication processes (i.e., scale-up manufacturing), 3) the formulation and curing of the elastomeric stamp (i.e., material optimization), and 4) the cell seeding method leading to the production of an hPSC-PR patch aimed at reconstructing the outer neural retina.

2.2. Scaffold design

We sought to engineer a biocompatible and biodegradable scaffold capable of capturing a high density of PRs. In the retina of humans and other vertebrates, PRs are exclusively found in the outer nuclear layer (ONL), which is approximately 8-10 cell nuclei thick and approximately 30 µm in height, with PR cell densities ranging from tens of thousands to hundreds of thousands in the macular region of healthy human retinas.[14-18] In designing the scaffold, we drew upon our previous experience with the first-generation scaffold possessing wineglass-shaped cell capture wells.[13] While the wineglass PR scaffold introduced key advancements in biomaterial scaffold engineering, including the potential to promote PR polarization, its cell carrying capacity was low (1-2 cells/well) in comparison to the relatively high volume of synthetic biomaterial. Therefore, an "ice-cube tray"-shaped scaffold was designed as a second-generation scaffold to maximize cell payload while also reducing overall biomaterial burden (Table 2.1).

	Wineglass scaffold design[13]	Ice cube tray scaffold design
Overall thickness [µm]	25	30
Space between through-holes [µm]	16	10
Through-holes [µm]	5 diameter, 10 depth (1 hole per capture well)	5 diameter, 5 depth (9 holes per capture well)
Capture well reservoir volume [mm^3]	0.177 x 10^{-5}	2.103 x 10^{-5}
Scaffold biomaterial volume (based on a 5 mm diameter scaffold) [mm^3]	0.34	0.169 (**50% less biomaterial**)
Young's modulus [MPa]	1.18	1.3

Table 2.1. *Structural and mechanical specifications for wineglass and ice cube tray scaffolds.*

Specifically, the second generation ice cube tray scaffold was comprised of two layers: 1) a reservoir layer (i.e., cell capture well layer) in which PRs are seeded, and 2) a base layer with regularly placed through-holes to facilitate fluid and nutrient transport (Figure 2.1).[19]
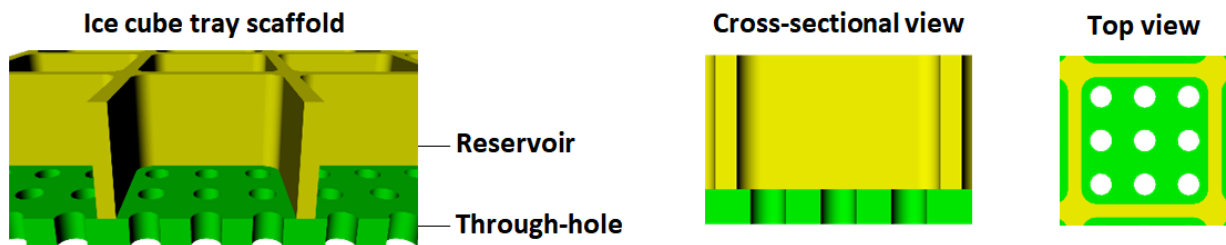
Figure 2.1. Schematic illustration of the ice cube tray PR scaffolds designed to have a reservoir layer for cell capture and retention and a through-hole layer for exchange of fluid, waste products, and nutrients both in vitro and during scaffold degradation in vivo.

Reservoirs were designed to have sufficient volume and height (i.e., length/width/height 29/29/25 µm) to enable capture of multiple PRs in an individual reservoir (Figure 2.2). Furthermore, to promote cell seeding inside the wells as opposed to along the top of the walls, the reservoir wall width was designed as thin as possible (~3 µm) while retaining structural integrity. Similarly, to prevent cells (whose nuclei average 6 µm in diameter) from escaping through the perforated base layer, the through-hole diameter was also minimized (~5 µm). The desired scaffold thickness was near that of the native macular ONL (~30 µm), which is also consistent with recent arguments that scaffolds with a thickness less than 50 µm can enable interactions between seeded neuroretinal cells and the host RPE. [17, 20, 21]
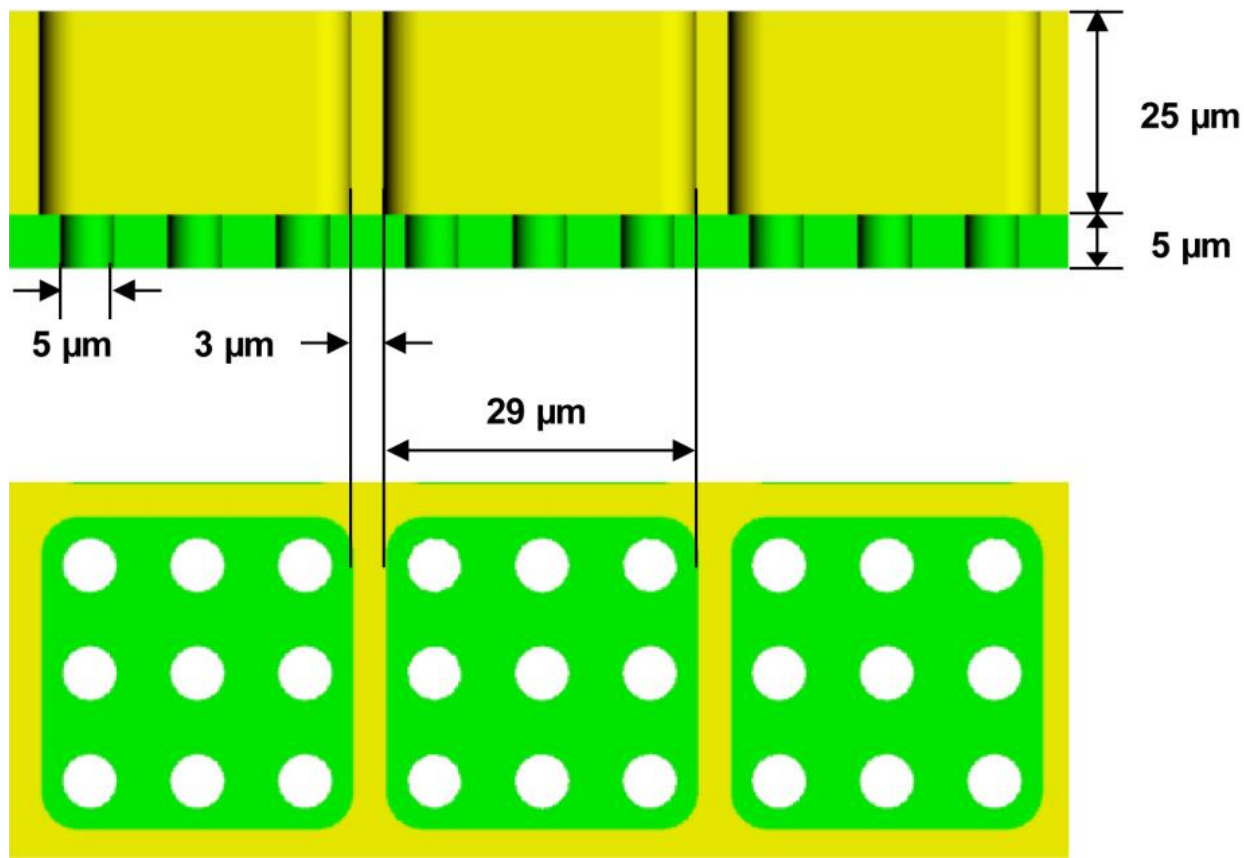
Figure 2.2. *Schematic illustration of the ice cube tray Si master mold. Detailed dimensions of the through-hole layer (green) and the reservoir layer (yellow) are as shown.*

2.3. Biomaterial selection for scaffold fabrication

Desirable retinal scaffold characteristics include the use of fully biodegradable materials possessing mechanical properties compatible with those of the human retina, both of which are important for clinical translation. The retina has a Young's modulus of just 0.02 MPa,[22] making this tissue extremely flexible as well as fragile. A higher modulus (>1 MPa) has been shown to enhance surgical handling of RPE scaffolds[23] without sacrificing safety or performance following implantation in the SRS. We thus sought to develop a scaffold with a Young's

modulus slightly above 1.0 MPa, balancing the need for rigidity during transplantation with flexibility to conform to the curvature of the eye upon delivery. The ideal biomaterial and its degradation products should also have proven compatibility with retinal tissue so as not to induce damage to surrounding host cells in vivo. Furthermore, the scaffold material must form thin (ideally <50 µm to facilitate interactions with RPE),[20] stable films and be amenable to the formation of precise, three-dimensional PR capture well geometries during the micromolding process. Poly(glycerol-sebacate) (PGS) was selected as the biomaterial of choice due to its retinal biocompatibility,[24, 25] known degradation behavior in the subretinal space (<30-60 days),[25, 26] and suitable Young's modulus (1.18-1.66 MPa).[13, 26] Furthermore, PGS undergoes gradual hydrolytic and enzymatic degradation to generate sebacic acid and glycerol, both of which are natural mammalian metabolites that are fully eliminated via physiologic mechanisms. [26, 27] Lastly, PGS provides the ideal combination of relatively rapid degradation in vivo with slow degradation in vitro.[26] We did not observe scaffold degradation after hPSC-PR seeding for up to 30 days in culture,[13] which offers a wide time window to seed and maintain scaffolds while making arrangements for transplantation.

2.4. Scaffold manufacturing process

2.4.1. Fabrication of Si master

With the aforementioned desirable scaffold characteristics in mind, the second-generation outer retinal scaffold with an ice cube tray structure was fabricated using microfabrication and micromolding techniques, which are among the most promising approaches currently used in drug and cell delivery systems.[28, 29] Figure 2.3 depicts the process workflow for fabricating PGS ice cube tray PR scaffolds.
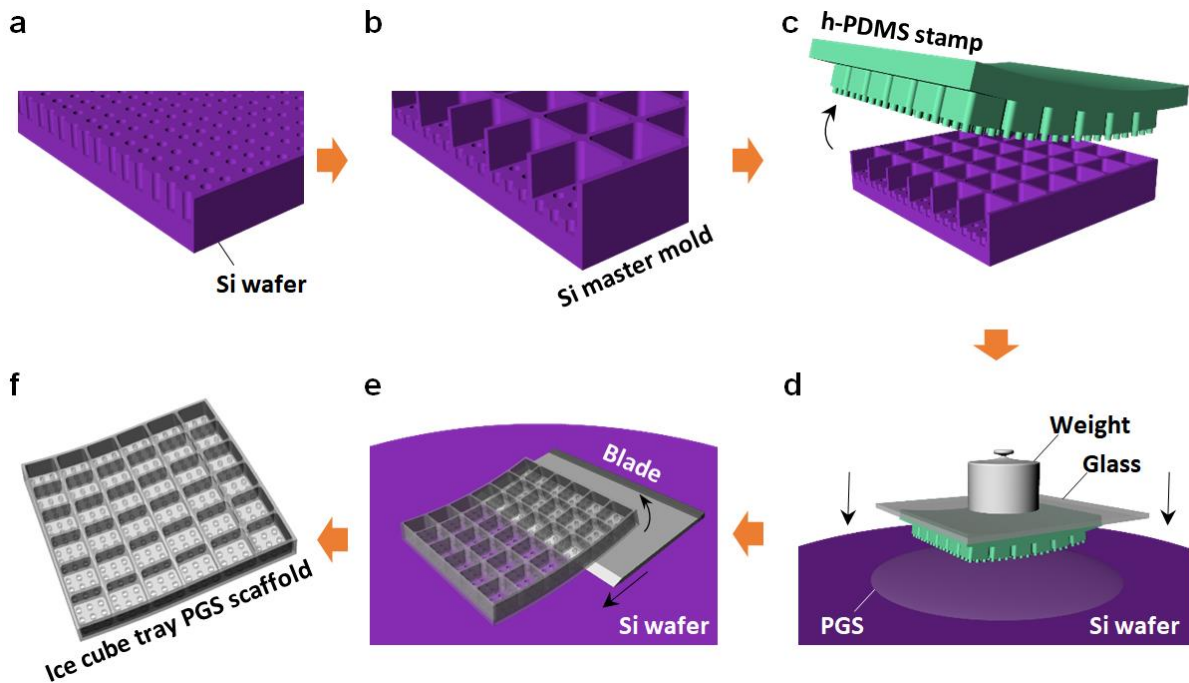
Figure 2.3. *Schematic illustration of the procedure to fabricate the ice cube tray PR scaffolds using a PGS prepolymer. a) Through-hole and b) reservoir etching processes of a Si master mold. c) Molding and demolding processes of a h-PDMS stamp from the Si master mold. d) Mounting and demounting processes of the h-PDMS stamp for fabricating a PGS ice cube tray PR scaffold. e) Delamination process of the scaffold using a razor blade. f) Final PGS ice cube tray PR scaffold.*

First, to fabricate a reusable silicon (Si) master mold with two distinctly patterned layers, a dense array of Si microstructures (through-holes and reservoirs) was created using photolithography and deep reactive ion etching (DRIE), a highly anisotropic etch process optimal for creating steep-sided holes or trenches in Si wafers (Figure 2.3a and b). [30] Here, during the DRIE process, RIE-lag effect and microloading effect were manipulated to achieve desired structure dimensions. RIE-lag effect refers to the dependency of etch rate on feature size

(e.g., smaller features result in slower etch rates), while the microloading effect describes the relationship between local etch rate and pattern density (i.e., features in areas of high pattern density experience more competition for reactants, leading to a gradient in reactant flux and slower etch rate).[31] While generating the Si master mold, through-holes underwent two etching steps: a primary etching step and a secondary etching step (Figure 2.4).
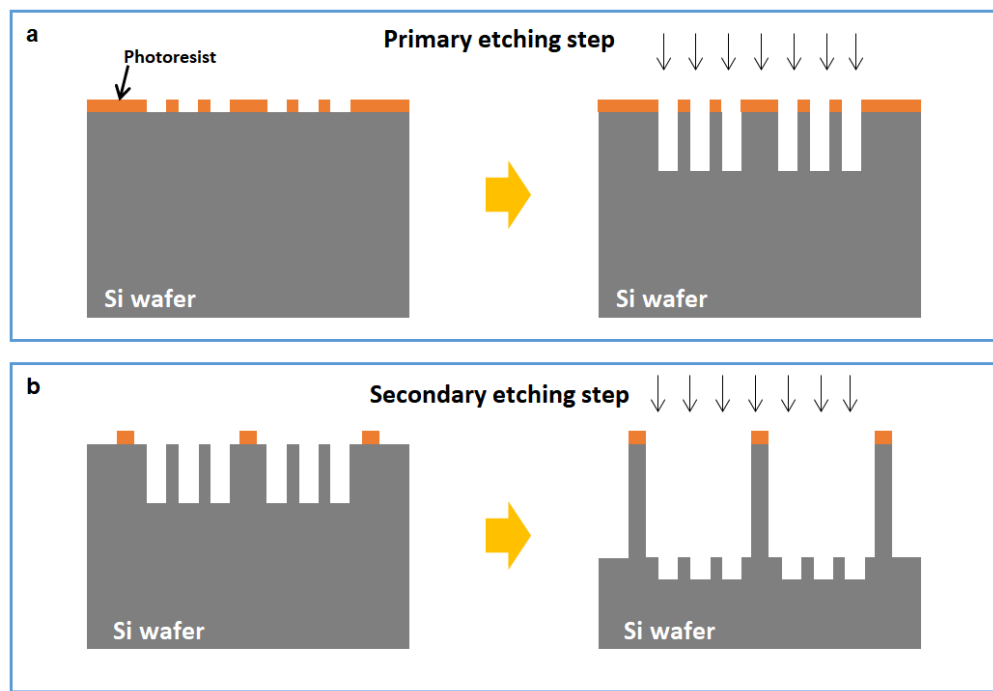
Figure 2.4. *Schematic illustration of a) the primary etching step and b) the secondary etching step. Both the microloading and RIE-lag effects influence the etch rate in each step.*

The etch rates of the through-holes in each step differed due to the microloading effect, with the primary etch rate and the secondary etch rate set at 2.148 µm/min and 1.746 µm/min, respectively. On the other hand, reservoirs only went through the secondary etching step and the

etch rate of the reservoirs was 2.448 µm/min, which was higher than the primary etch rate of the through-holes (i.e., 2.148 µm/min) due to the RIE-lag effect caused by the difference in feature size. By considering these effects and precisely calculating the etch rates, the desired target depths—approximately 5 µm for the through-hole layer and 25 µm for the reservoir layer—were successfully achieved (Figure 2.5).
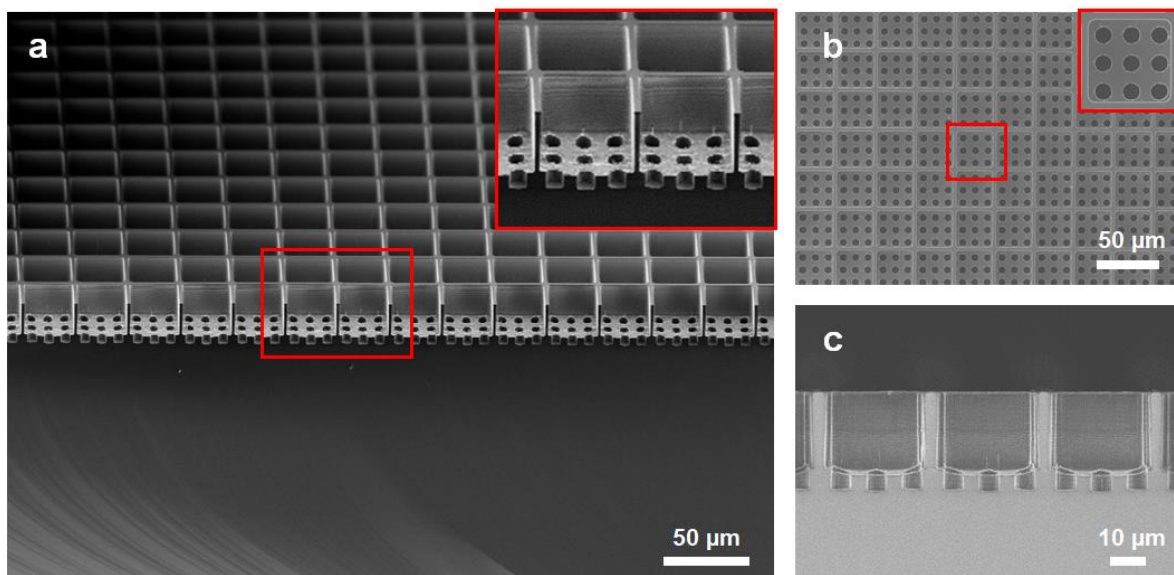
Figure 2.5. Fabrication of Si master mold. SEM images of the ice cube tray-shaped Si master mold showing a) a tilted view, b) a top view, and c) a cross-sectional view, respectively. The inset images show a magnified view of the microstructures of the fabricated Si master mold.

The final Si master mold included a base layer of through-holes with a diameter of 5.1 µm and a depth of 4.8 µm, and a secondary layer of cuboidal (i.e., ice cube tray) reservoirs with a dimension of 29 µm × 29 µm × 24.5 µm. The width of the reservoir walls and the distance between adjacent through-holes were 2.8 µm and 5 µm, respectively, meeting the target dimensions. To facilitate smooth molding and demolding in the next fabrication step (Figure

2.3c), the fabricated Si master mold was coated with a chemically inert passivation layer. Plasma-polymerization was conducted with octafluorocyclobutane (C_4F_8) as a precursor by DRIE, generating a Teflon-like polymer film with long linear $(CF_2)_n$ chains.[32]

2.4.2. Fabrication of PDMS stamp

Next, to create a reusable elastomeric stamp (i.e., a negative master mold for the fabrication of the final scaffold) that would not deform, bend, or buckle during the molding process (Figure 2.3d), polydimethylsiloxane (PDMS) was selected as the ideal material. Soft-PDMS stamps were initially tested, but these were frequently deformed during the demounting process due to the adherent nature of soft-PDMS (Figure 2.6).
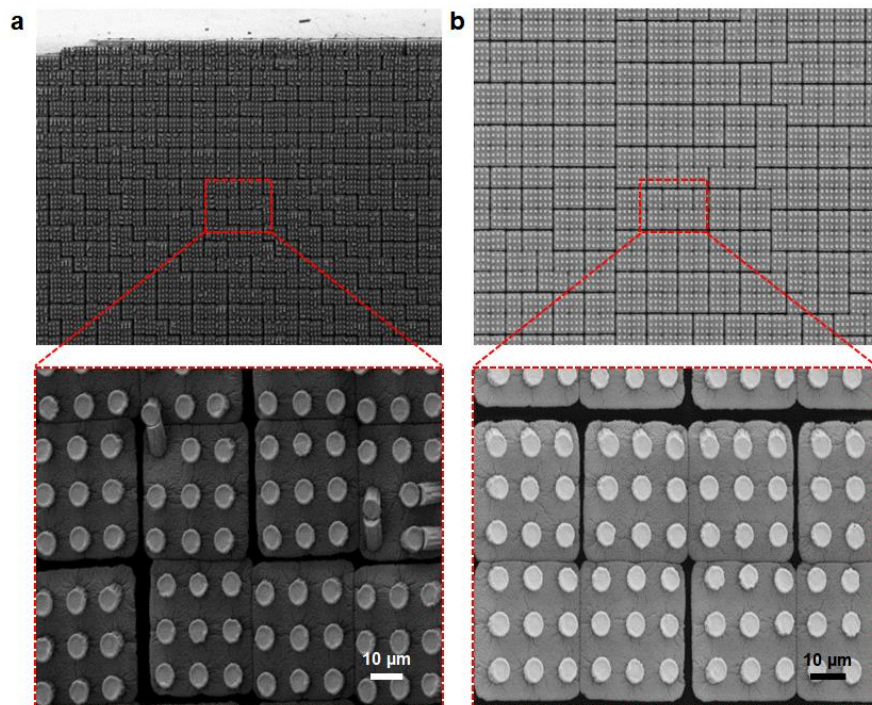
Figure 2.6. *SEM images of the microstructures of a) a soft-PDMS 10:1 (base: curing agent) stamp and b) a soft-PDMS 4:1 stamp.*

Hard-PDMS (h-PDMS) proved sufficiently strong to serve as the optimal stamp material. To create the stamp, liquid h-PDMS was poured over the fabricated Si master mold and left to cure for 12 hours at room temperature followed by 2 hours at 60 ℃. After curing, the stamp was carefully demolded from the Si master mold without large surface defects, producing a high yield (>95%) of the desired ice cube tray microstructures (Figure 2.7). The stamp surface was coated with a monolayer of hydrophobic silane (an anti-adhesive layer) under vacuum to facilitate demounting from the final PGS scaffold. The microfabrication processes for the Si master mold and h-PDMS stamp are described in greater detail in the Experimental section.
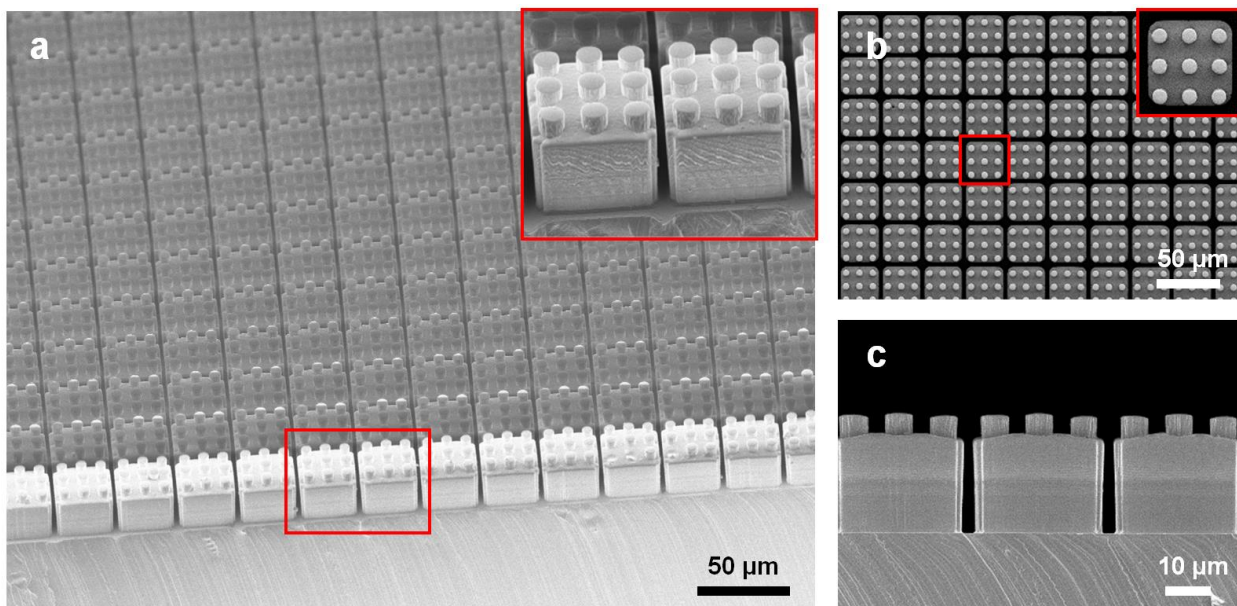

Figure 2.7. Fabrication of h-PDMS stamp. *SEM images of the ice cube tray-shaped h-PDMS stamp showing a) a tilted view, b) a top view, and c) a cross-sectional view, respectively. The inset images show a magnified view of the microstructures of the fabricated h-PDMS stamp.*

2.4.3. Fabrication of PGS scaffold

Figure 2.3e and f depict the final steps in the micromolding process for fabricating the ice cube tray PR scaffold from a PGS prepolymer with the h-PDMS stamp. First, PGS prepolymer was placed on a clean Si wafer and melted on a hotplate at 120 ℃. The micropatterned surface of the h-PDMS stamp was then immersed into the liquid PGS. A glass slide with an overlying weight of 380 g was placed atop the stamp, pressing the liquid PGS between the h-PDMS stamp and the Si wafer (Figure 2.3e) to control the scaffold thickness (Figure 2.8).
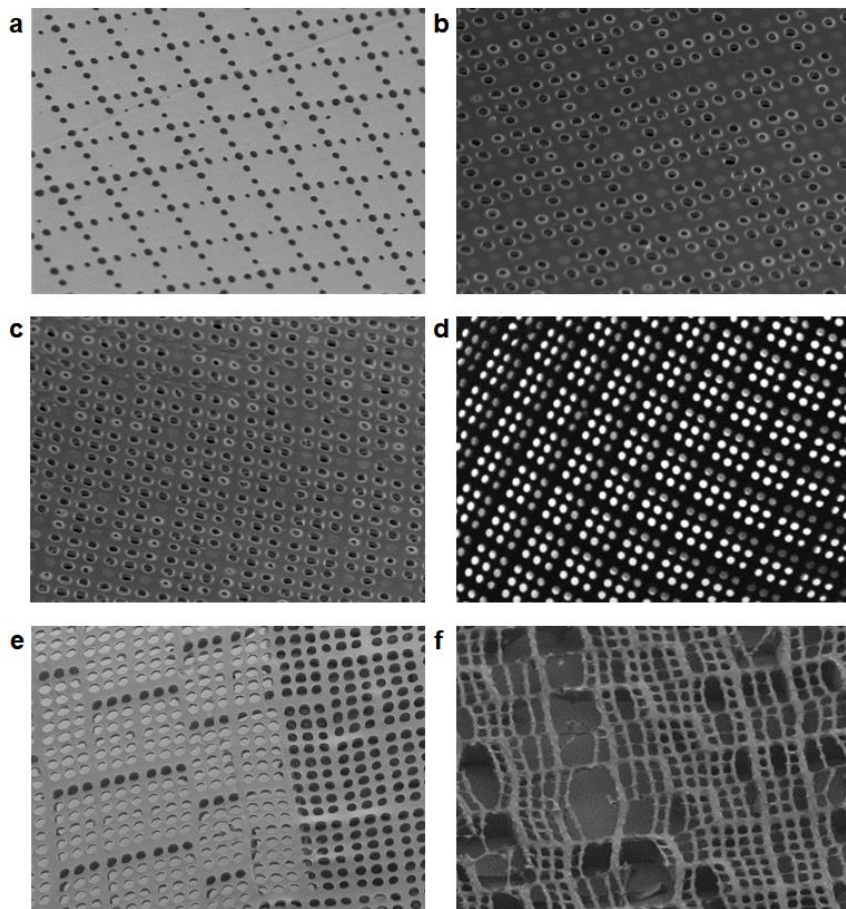
Figure 2.8. *SEM images (bottom view) of the PGS ice cube tray PR scaffolds fabricated using the molding weights of a) 120 g, b) 240 g, c) 300 g, d) 380 g, e) 580 g, and g) 780 g, respectively.*

The scaffold microfabrication apparatus was subsequently placed into a vacuum oven and cured under high vacuum (<1 mbar) at 120 °C for 3 days. Figure 2.9a shows a cured PGS scaffold between the h-PDMS stamp and the Si wafer prior to demounting. After curing was complete, the h-PDMS stamp was demounted from the Si wafer, taking care to avoid fractures of the h-PDMS ice cube tray microstructures due to the rigid nature of h-PDMS. Fabricated PGS scaffolds were evaluated via scanning electron microscopy (SEM) to screen for surface defects attributable to the demounting process.
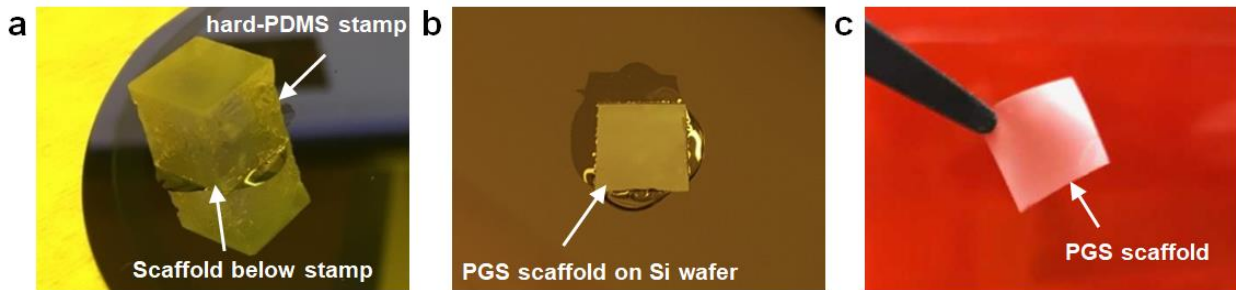
Figure 2.9. *Low magnification photographic images depicting the fabrication process of the PGS ice cube tray PR scaffold. a) h-PDMS stamp ready to be demounted from the scaffold on a Si wafer after complete PGS curing. b) A PGS scaffold on the Si wafer after stamp removal. After removing scaffold edges, the scaffold was delaminated from the Si wafer using a single edge razor blade. c) Fabricated PGS ice cube tray scaffold held with fine forceps.*

Despite careful handling, early microfabrication experiments often resulted in retention of fractured h-PDMS microstructures in the final scaffold product, rendering the h-PDMS stamp inoperable for further use (Figure 2.10).
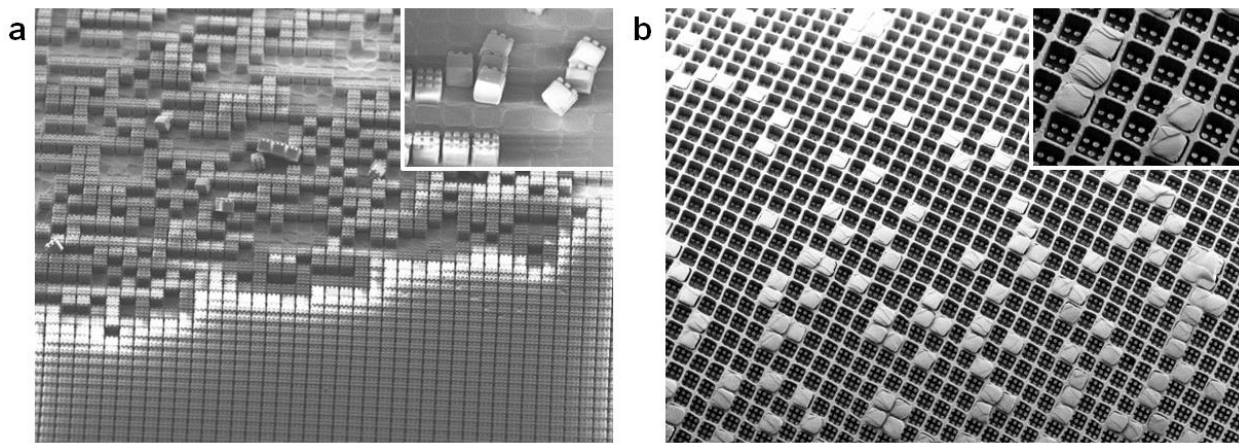
Figure 2.10. SEM images of a) a h-PDMS stamp with microstructures broken or damaged during the demounting process and b) a PGS ice cube tray PR scaffold with broken h-PDMS microstructures after stamp demounting.

To address this challenge, isopropyl alcohol (IPA) soaking was employed, as it allows polymers to swell and can facilitate release from secondary mold structures.[33] The h-PDMS stamp, cured PGS, and Si wafer were incubated in IPA at room temperature for 12 hours, allowing IPA to permeate the PGS scaffold. Using this approach, the PGS scaffold on a Si wafer could be reliably demounted from the h-PDMS stamp without surface defects or retained h-PDMS stamp microstructures (Figure 2.9b), maintaining the h-PDMS stamp surface integrity for reuse (Figure 2.11). Thereafter, the PGS scaffold was carefully delaminated from the Si wafer using a single razor blade (Figure 2.3e) and unrolled with sonication treatment in IPA. The microfabrication process was subsequently optimized to produce a scaffold with minimal biomaterial burden and sufficient structural integrity for successful delamination (Figure 2.12).
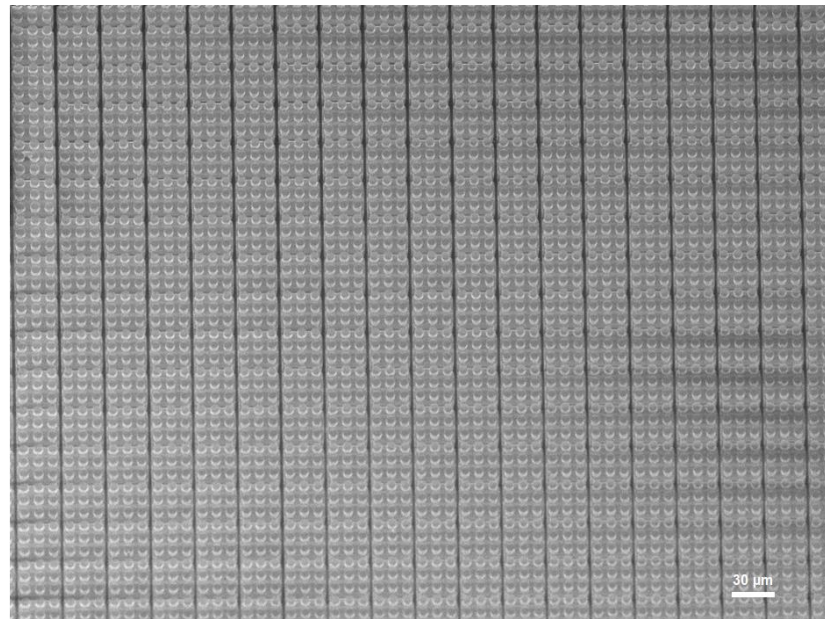
Figure 2.11. *SEM image of a h-PDMS stamp (top view) after demounting from a Si master mold in an IPA solution. Immersion in the IPA solution resulted in smooth demounting of the stamp.*
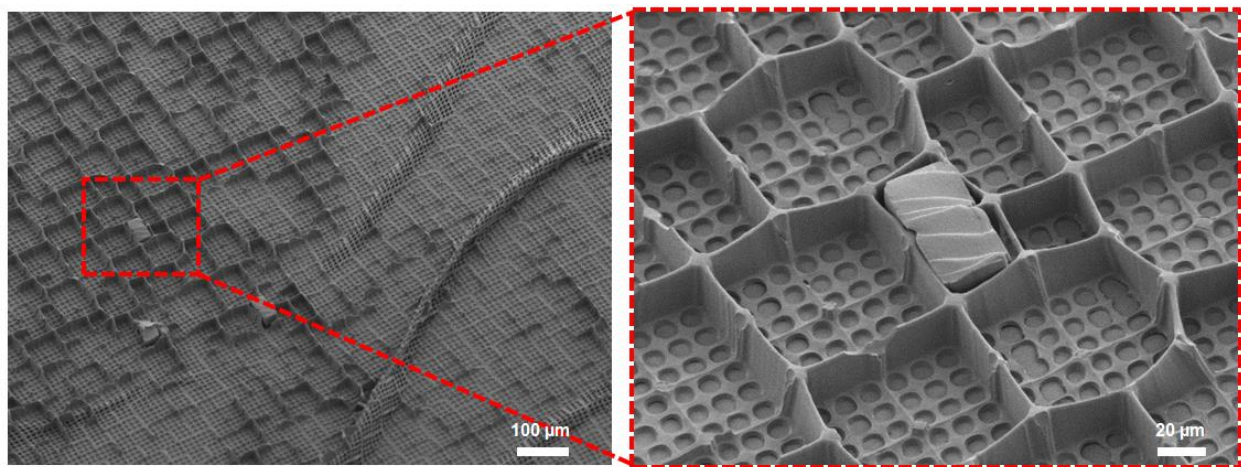
Figure 2.12. SEM images of torn PGS scaffold reservoir walls. *The PGS scaffold reservoir walls were damaged during the demounting process when spacing between wells was reduced (i.e., walls were <3 μm).*

The final micro-patterned ice cube tray scaffold is shown via a schematic (Figure 2.3f) and low magnification photography (Figure 2.9c). To assess microstructure quality and uniformity in the final product, the scaffolds were imaged with SEM; top, bottom, and cross-sectional views of the fabricated scaffold revealed precise, neat, and uniform ice cube tray reservoirs with the desired through-hole structures in the base of the scaffold (Figure 2.13).
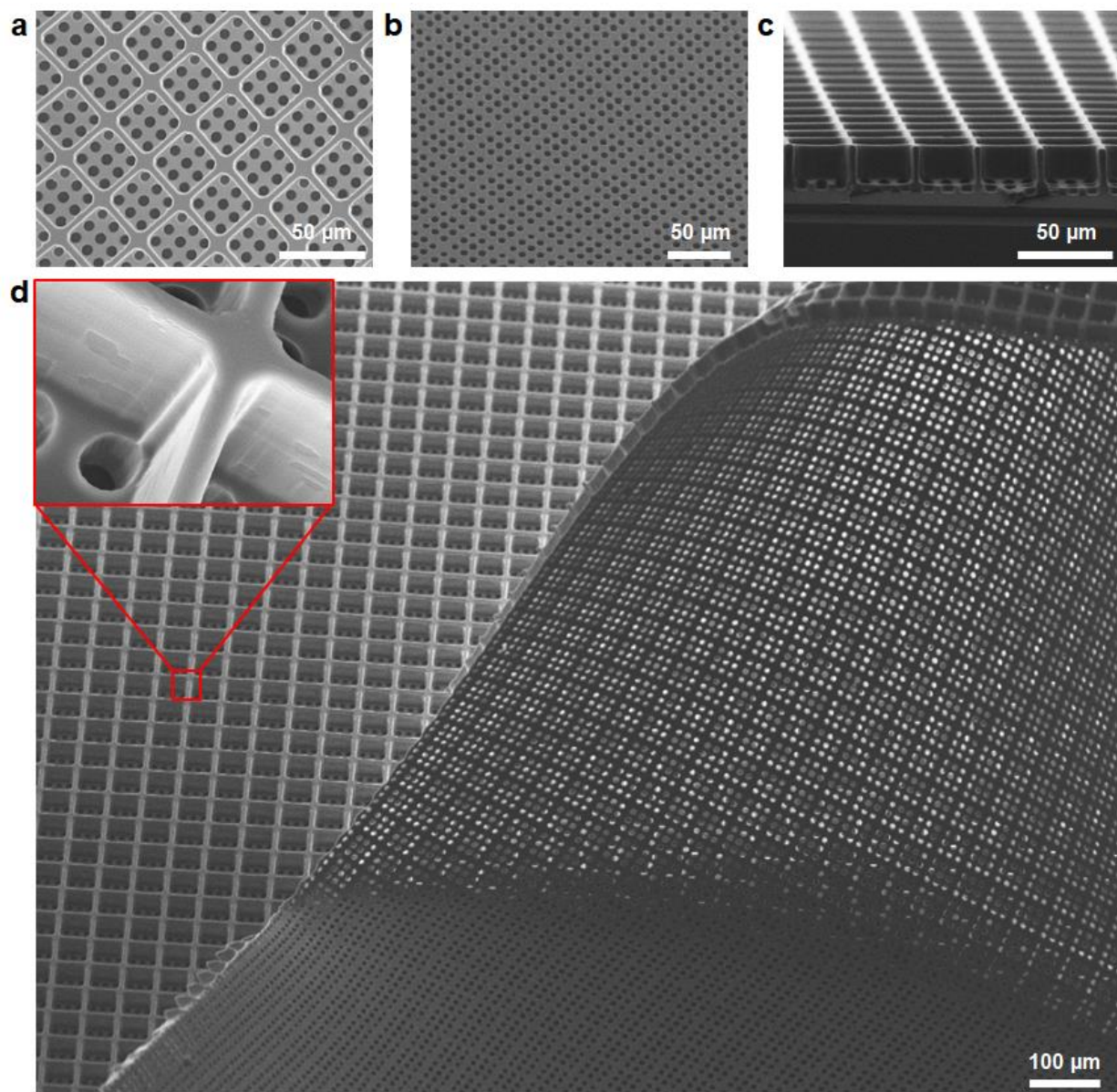
Figure 2.13. SEM images of the fabricated ice cube tray PR scaffolds showing d) a top view, e) a bottom view, and f) a cross-sectional view. g) Large area SEM image of the fabricated scaffold and a magnified view of a scaffold reservoir wall (inset).

In particular, the microstructure surfaces were smooth with no irregular or elevated edges and minimal structural defects. Furthermore, the final scaffold product had a high microstructure yield (>98%) over a large area (Figure 2.13d). A detailed description of the fabrication process for ice cube tray PGS scaffolds can be found in the Experimental section. Taken together, the optimized fabrication process for the ice cube tray design achieves a finely tuned balance between three critical and interrelated design criteria: target dimension, minimized biomaterial burden, and structural integrity.

2.4.4. Mounting PGS scaffolds on transwell inserts

To facilitate cell seeding, scaffolds were incorporated into a commercially available 12-mm polyester transwell cell culture insert (Corning® Costar® Snapwell, Sigma) prior to sterilization (Figure 2.14). To mount scaffolds into the insert, a 5-mm biopsy punch was used to create a round hole in the center of the polyester transwell membrane, which is the approximate diameter of the human macula.[14] Scaffolds were then mounted in the center of the transwell membrane and secured with soft-PDMS as an adhesive (Figure 2.14a). Transwell inserts were snapped into holders (Figure 2.14b) and placed in a 6 well plate (Figure 2.14c). Scaffolds were treated with O_2 plasma to enhance the surface hydrophilicity and thus microstructure wettability, preventing microbubbles from forming within each capture well (Figure 2.15) and promoting uniform cell seeding in the capture wells.[13, 34, 35]
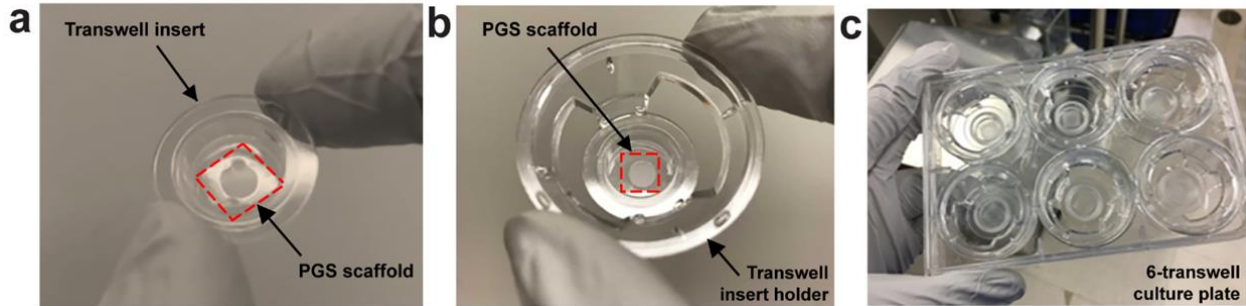
Figure 2.14. *Low magnification photographic images depicting scaffold mounting into the transwell insert. a) Transwell insert with PGS scaffold below. The outer edge of the scaffold was glued to the transwell insert with soft PDMS. The area of the transwell insert removed to mount scaffolds was 19.6 mm2 (internal diameter: 5 mm). b) Transwell insert holder with a PGS ice cube tray scaffold mounted into a transwell insert. c) 6-transwell scaffold cell culture system.*
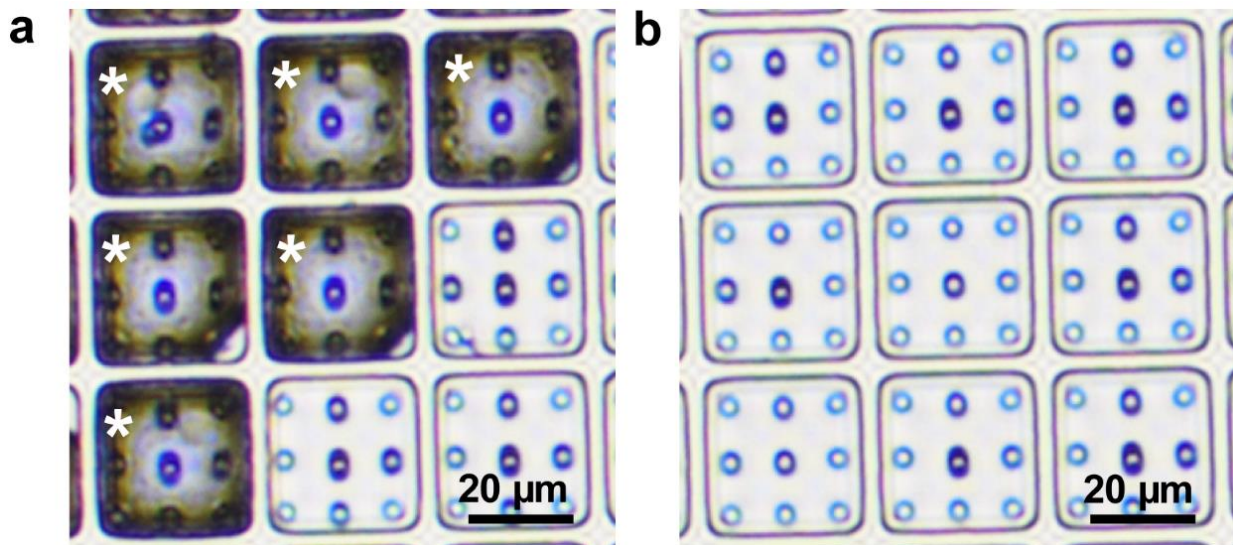
Figure 2.15. *Light microscopic images of empty PGS ice cube tray scaffolds taken a) before and b) after ethylene oxide gas sterilization, revealing no alterations to scaffold microstructures.*

2.5. Mechanical compliance of PGS ice cube tray PR scaffolds

Since the eye is spherical in shape and outer retinal scaffolds necessarily experience internal and external stresses during delivery to the SRS, an ideal PR scaffold must be not only flexible enough to conform to curved surfaces, but durable enough to withstand local stresses without structural deformation. In addition, the scaffold should return to its original form when local stresses are removed to protect and maintain proper organization of captured cells. To model this, the mechanical properties of the PGS ice cube tray PR scaffold were assessed via finite element analysis and compared to those of our original wineglass PR scaffold[13] to elucidate mechanical benefits and tradeoffs of each design (Figures 2.16 and 2.17).

To determine how the scaffolds with two different designs (wineglass vs. ice cube tray) behave under external stresses, a fixed constraint was set to a square area in the center of each design that incorporated 9 through-holes. Thereafter, 5 N of tensile force per unit area was applied to the four sides of each scaffold in the x- and y-directions. As presented in Figure 2.16, the wineglass design had high stress concentrations along the boundary of the fixed constraint, leading to a change in the shape of the scaffold. In contrast, the resulting stress was uniformly and efficiently distributed throughout the ice cube tray scaffold, without causing any appreciable deformation of the scaffold (Figure 2.17), although the ice cube tray design had a higher stress than the wineglass design due to its thinner through-hole layer (i.e., 5 vs. 10 µm), which largely determines the mechanical properties of the scaffolds because the reservoir layer only consists of very thin reservoir walls (i.e., ≤ 3 µm).
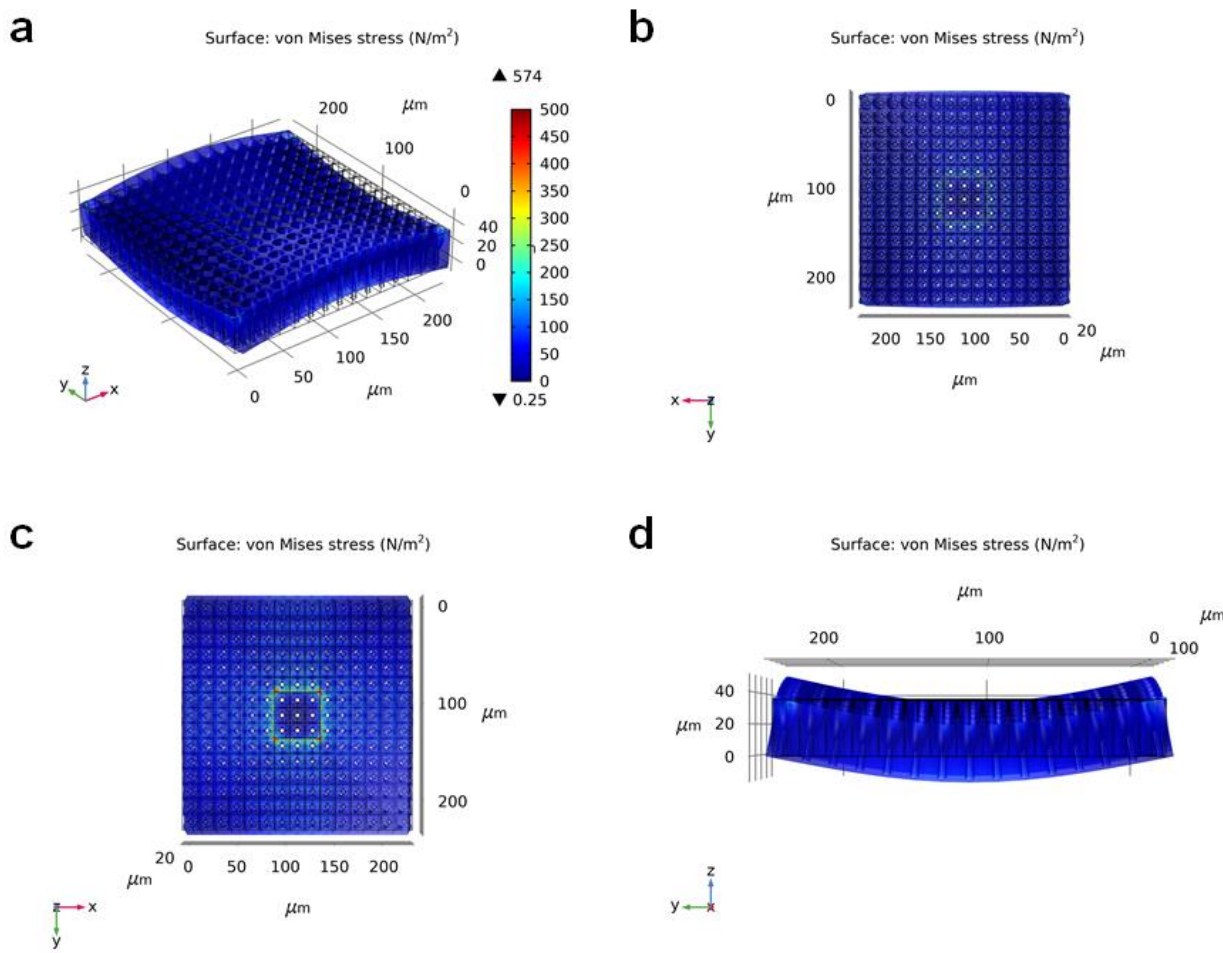
Figure 2.16. *Finite element analysis showing equivalent von Mises stress distribution in the PGS scaffolds with wineglass design under 5 N of tensile force in the x- and y-directions: a) isometric view, b) top view, c) bottom view, and d) orthogonal view. The color bar shows the von Mises stress (in N/m^2) for an applied tensile force.*
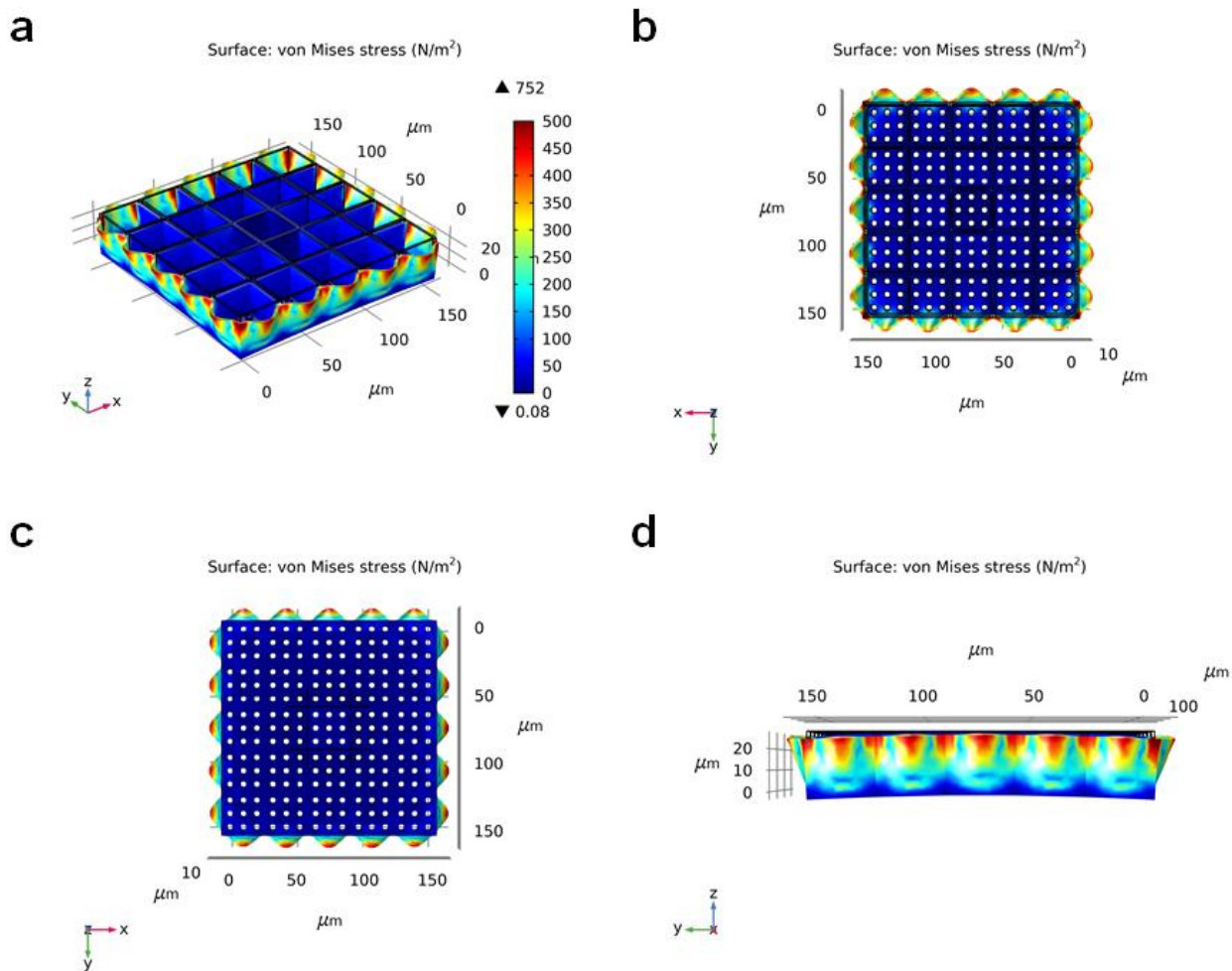
Figure 2.17. *Finite element analysis showing equivalent von Mises stress distribution in the PGS*

scaffolds with ice cube tray design under 5 N of tensile force in the x- and y-directions: a)

isometric view, b) top view, c) bottom view, and d) orthogonal view. The color bar shows the von

Mises stress (in N/m^2) for an applied tensile force.

Tensile strength and elastic modulus were also measured to assess the ice cube tray

scaffold's mechanical properties. The modulus of the ice cube tray scaffold was 1.3 MPa, and all

microstructures recovered to their original shapes after the tensile stress was removed (Figure

2.18), indicating favorable pliability for any surgical handling associated with transplantation.

These results convincingly demonstrated that the ice cube tray design has superior mechanical properties compared to the wineglass design, both in terms of uniformity of stress distribution and extent of scaffold deformation under a defined tensile stress, two factors that are key for safe and consistent scaffold delivery in vivo.
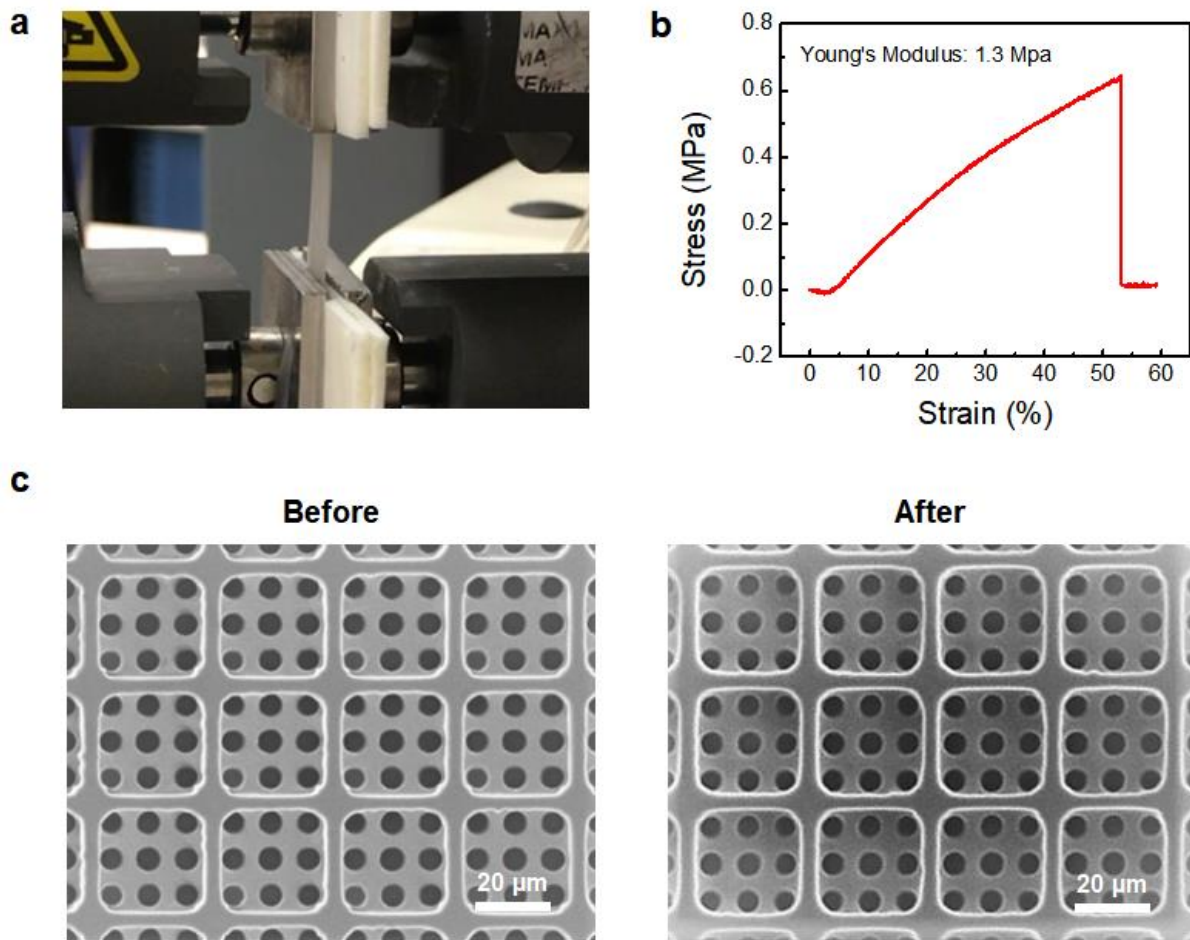
Figure 2.18. *Tensile stress test for the fabricated PGS ice cube tray PR scaffold. a) Low magnification photographic image of the PGS scaffold during a tensile stress. b) Tensile stress-strain curve of the PGS scaffold. c) SEM images comparing PGS scaffold surfaces before and after the tensile strain.*

2.6. PR cell seeding in ice cube tray scaffolds

Scaffolds were seeded with cell suspensions at several concentrations (1, 3, 5 or 7 million cells/transwell) and cultured for 5 days to assess biocompatibility and determine the minimum number of cells necessary to achieve maximal scaffold carrying capacity. Confocal imaging of fixed, immunostained scaffolds confirmed successful seeding and survival of multiple PRs in individual wells of ice cube tray scaffolds (Figure 2.19a). As shown in Figure 2.19b, maximal scaffold carrying capacity could be achieved by seeding at a concentration of 5 million cells per transwell (total area of transwell = 467 mm^2). Importantly, these experiments revealed that the ice cube tray design enabled a 3.4-fold increase in cell carrying capacity (calculated with equations 2.1 and 2.2) compared to the original wineglass-shaped PR scaffold design (Table 2.2).
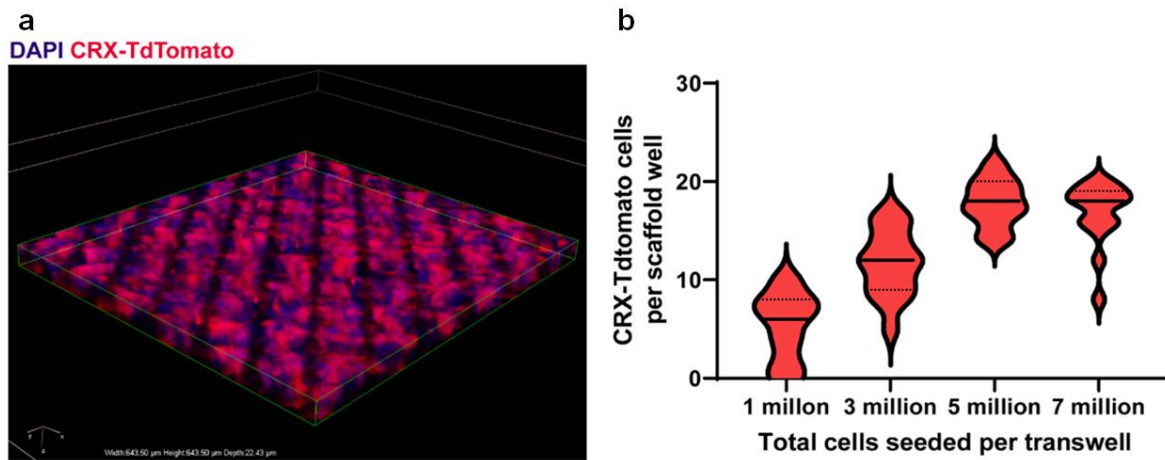
Figure 2.19. *a) 3D rendering of a scaffold (176 μm × 185 μm × 22 μm) confirms successful capture of multiple PRs (labeled in red) in individual capture wells. Cell nuclei are labeled with DAPI (blue). b) Cells were seeded onto scaffolds at varying densities to determine the minimum number required to achieve the maximum carrying capacity of CRX$^{+/tdTomato}$-PRs per well. Median (bold dashes) and quartiles (fine dashes) are shown within individual violin plots.*

Equation 2.1. *Mathematical calculation of the number of reservoirs (n_{res}) contained within the area of the single 5 mm diameter round scaffold. A_{scaf} is the area of a single scaffold (19.63 mm^2, or the area of a 5 mm diameter circular scaffold) and A_{ru} is the area of a single reservoir unit, which is defined as a square area centered in the middle of one reservoir and extending in all four orthogonal directions to a point mid-way to the center of each adjacent reservoir as shown in Figure 2.20.*

$$\mathbf{n_{res} = A_{scaf} / A_{ru}} \qquad (2.1)$$

Equation 2.2. *Estimated cell carrying capacity of a single scaffold, defined as the estimated number of PRs present within a single 5 mm diameter round scaffold. n_{PR} is defined as the average number of PRs counted in a single reservoir.*

$$\textbf{Cell carrying capacity} = \mathbf{n_{PR} \times n_{res}} \qquad (2.2)$$

	Wineglass scaffold design (Jung and Phillips et al., 2018)	Ice cube tray scaffold design
Average number of photoreceptors per capture well	1.3 ± 0.5	17.8 ± 2.4
Photoreceptors within a single scaffold [5 mm diameter or 19.63 mm^2]	1.005 x 10^5	3.412 x 10^5
Scaffold photoreceptor density [cells/mm^2] [6.0 – 20.0 x 10^4 cells/mm^2 within the macula in healthy retina]	0.512 x 10^4	1.74 x 10^4

Table 2.2. *Cell payload advantages of ice cube tray versus wineglass scaffold designs.*
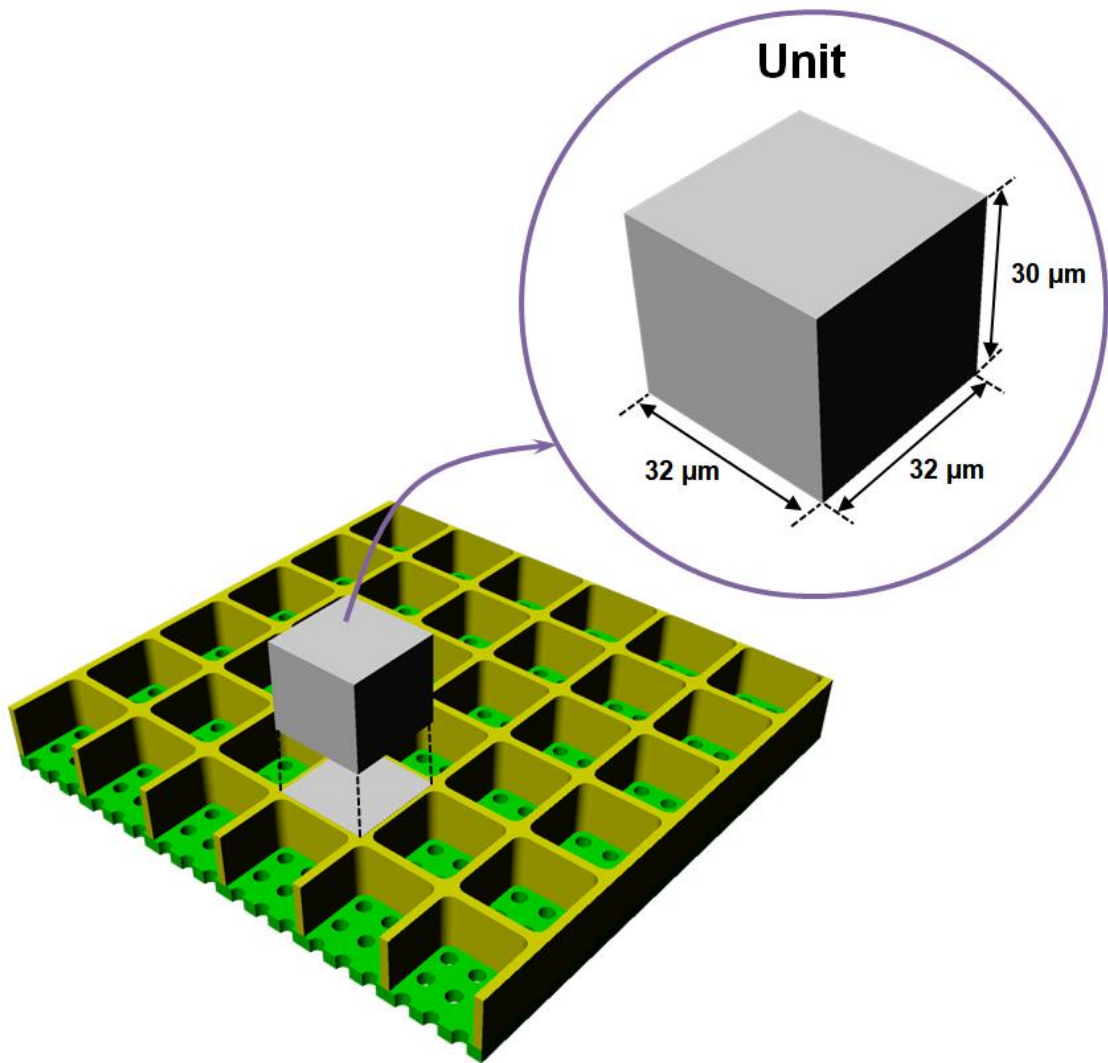
Figure 2.20. *Schematic illustration of a single reservoir unit of the ice cube tray scaffold showing its detailed dimensions.*

The differentiated PRs expressed cone- (cone arrestin; ARR3) and rod-specific (NR2E3) proteins as expected for hPSC-PRs derived from stage 2 retinal organoids (Figure 2.21).[36] The substantial increase in the cell payload capacity of the ice cube tray design, combined with its decreased overall biomaterial burden, which was 50% less for the ice cube tray design than the wineglass design (calculated with equation 2.3), further underscores its superiority (Tables 2.1

and 2.2). These results represent the highest-density capture of hPSC-PRs for any retinal scaffold described to date. Furthermore, this construct provides a means of exceeding the often-cited threshold of 150,000 PRs within a single scaffold (Table 2.2), which is the threshold theoretically needed to achieve an electroretinographic (ERG) response.[37, 38]
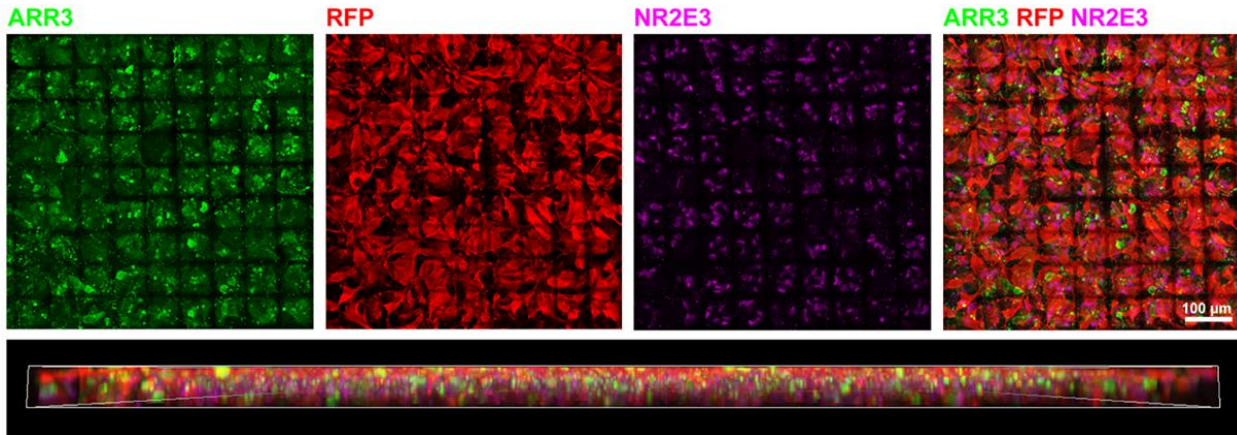
Figure 2.21. *Scaffolds seeded with CRX$^{+/tdTomato}$-PRs (RFP^{+}, red) contain both ARR3-expressing cone PRs (green) and NR2E3-expressing rod PRs (pink). A 3D lateral view of the scaffold demonstrates relatively even distribution of ARR3^{+} cones and NR2E3^{+} rods. 3D rendering is 644 μm × 644 μm × 20 μm*

Equation 2.3. *Mathematical calculation of the scaffold biomaterials volume (V$_{scaf}$) used for generating a PGS scaffold (based on a single 5 mm diameter scaffold). V$_{ru}$ is the volume of a single reservoir unit (Figure 2.20). V$_{th}$ and V$_{res}$ are defined as the volume of through-hole(s) within a single reservoir unit and the volume of a reservoir within a single reservoir unit, respectively.*

$$V_{scaf} = (V_{ru} - (V_{th} + V_{res})) \times n_{res} \qquad (2.3)$$

2.7. PR organization within PGS ice cube tray scaffold constructs

Given the importance of cell packing, organization, and polarization within the retina, particularly with regard to cones, we sought to determine whether the ice cube tray scaffold design facilitated pre-organization of hPSC-PRs within scaffold constructs. To assess PR polarity and scaffold construct organization, whole mounts of PGS ice cube tray scaffolds seeded with 5 million cells per transwell were screened for the presence of 1) outer segments (specialized light-detecting structures situated apically within PRs) and 2) presynaptic vesicles, which localize to the basal PR axon terminal (Figure 2.22).

3D reconstructions of scaffold flat mounts were analyzed to determine the primary location of outer segments and presynaptic terminals. CRX$^{+/tdTomato}$-PRs in scaffolds expressed peripherin (PRPH2) (Figure 2.22a and c), a protein crucial to the development of rod and cone outer segments[39] that contain photosensitive opsins. PRPH2$^+$ PR outer segments oriented perpendicularly to the base of the scaffold (Figure 2.22c). CRX$^{+/tdTomato}$-PRs also expressed VGLUT1, a presynaptic marker expressed within PR axon terminals (Figure 2.22b and d), which was primarily localized to the top half of the scaffold in 3D reconstructions (Figure 2.22d). Interestingly, in the wineglass design, PR axons tended to extend into the through-holes, with presynaptic markers localized at the base of the scaffold. The reversal in PR polarity seen with the ice cube tray design could be due to its substantially shorter through-hole length compared to the wineglass design (5 μm vs. 10 μm). Alternatively, the clustering of multiple PRs within a single well may provide local cell-cell interactions that are not present in the wineglass scaffold design. Regardless of the mechanism, a significant benefit of the PR polarity within the ice cube tray scaffold is the greater exposure area of donor PR axon terminals at the top of the scaffold, immediately adjacent to the dendritic terminals of host interneurons (i.e., bipolar cells). Such an

orientation not only minimizes barriers at the donor-host synaptic interface (prior to degradation of the biomaterial), it also positions the through-holes in the scaffold base to allow fluid and material exchange between the donor PRs and the host RPE and choroid as the scaffold degrades over time. Lastly, it concentrates the bulk of the biomaterial volume adjacent to the host RPE, the cell layer that plays a role in scaffold degradation within the SRS,[40] possibly due to secretion of extracellular matrix-remodeling matrix metalloproteases (MMPs).[41]
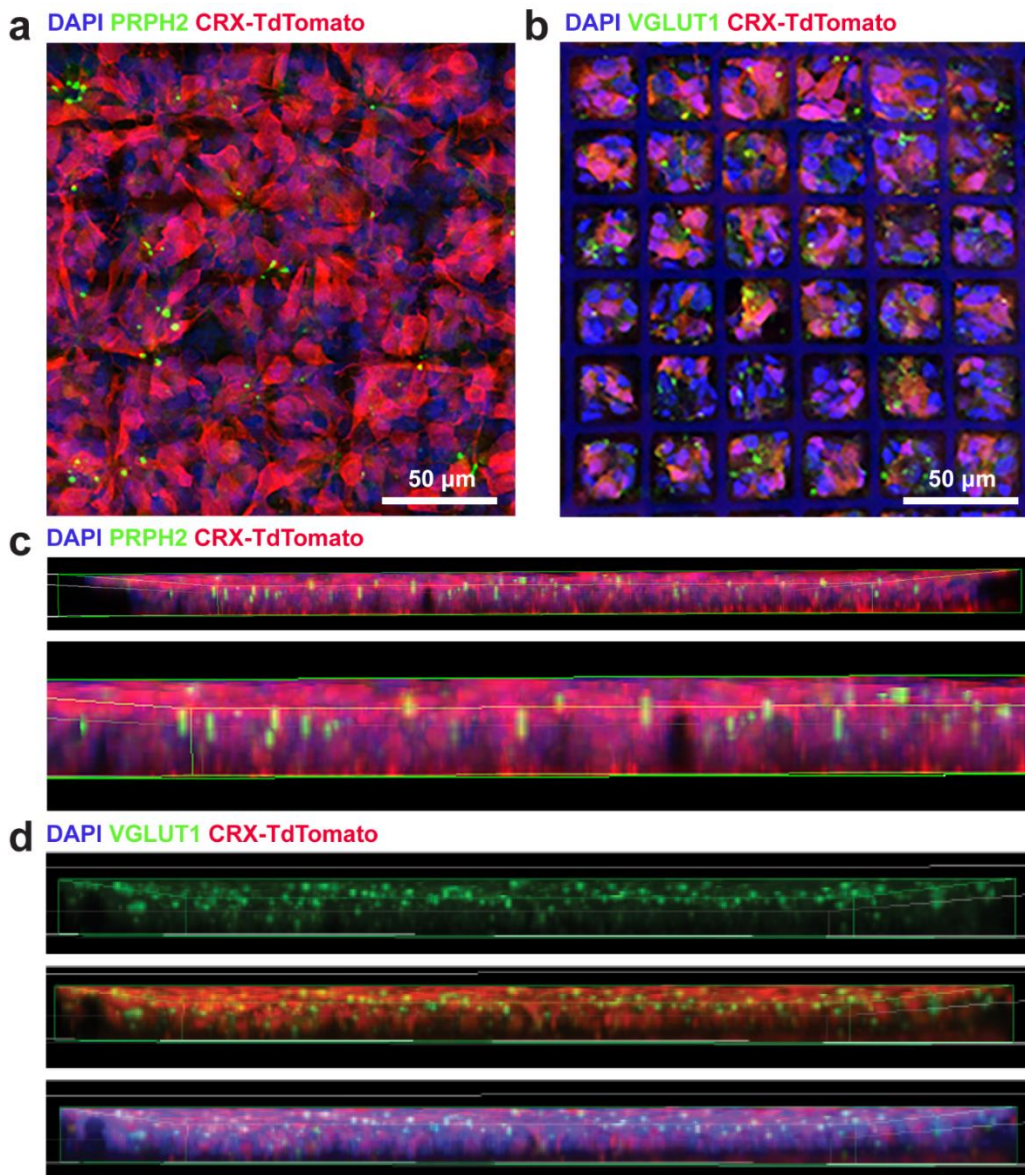
Figure 2.22. Micro-patterned ice cube tray scaffolds support prearranged orientation of seeded PRs. a, b) Maximum intensity projections of scaffold whole mounts seeded with CRX$^{+/tdTomato}$-PRs (red) revealed that PRs plated on scaffolds express PRPH2 (a, green) and VGLUT1 (b, green). DAPI-labeled cell nuclei and PGS autofluorescence are shown in blue. c) PRPH2$^+$ outer segments were often oriented perpendicular to the base of the scaffold (magnified in underlying image). d) Expression of presynaptic marker VGLUT1 (green) primarily localizes to the top portion of the scaffold. 3D renderings (c, d) are 644 µm × 644 µm × 20 µm.

2.8. Experimental section

2.8.1. Fabrication of Si master

An undoped Si wafer was used as a starting material. After a standard RCA cleaning process, an array of through-hole patterns was formed by photolithography using an AZ2020 photoresist and etched with deep reactive-ion etching (DRIE). During the DRIE process, etch/passivation cycles, etch/passivation time per cycle, plasma power, ICP power, and $SF_6/O_2/C_4F_8$ gas flows were 33/33 cycles, 10/5 sec, 11.7 W, 600 W, and 102/12/100 sccm, respectively. The diameter and depth of the etched through-holes were 5.1 µm and 11.8 µm, respectively (Figure 2.23). After removing the photoresist with organic solvents (acetone and IPA), the reservoir was formed by the same procedure used for the through-hole patterning and etching, except that the DRIE etch/passivation cycles were 60/60 cycles, respectively. For the fabricated Si master mold, the diameter and depth of through-holes were 5.1 µm and 4.8 µm, respectively, and the length, width, and depth of reservoirs were 29 µm, 29 µm, and 24.5 µm, respectively. The width of reservoir wall and the distance between adjacent through-holes were 2.8 µm and 5 µm, respectively. After the master mold was cleaned with organic solvents and

piranha solution, it was treated with oxygen plasma (Unaxis 790 RIE) for 20 sec at a plasma power of 40 W, pressure of 120 mTorr, and oxygen gas flow rate of 20 sccm to remove the remaining organic contaminants. Finally, to coat a chemically inert passivation layer on the Si master mold, plasma-polymerization was conducted with octafluorocyclobutane (C_4F_8) as a precursor by DRIE (C_4F_8 = 97 sccm, time = 1 min), generating a Teflon-like polymer film with long linear $(CF_2)_n$ chains.[32]
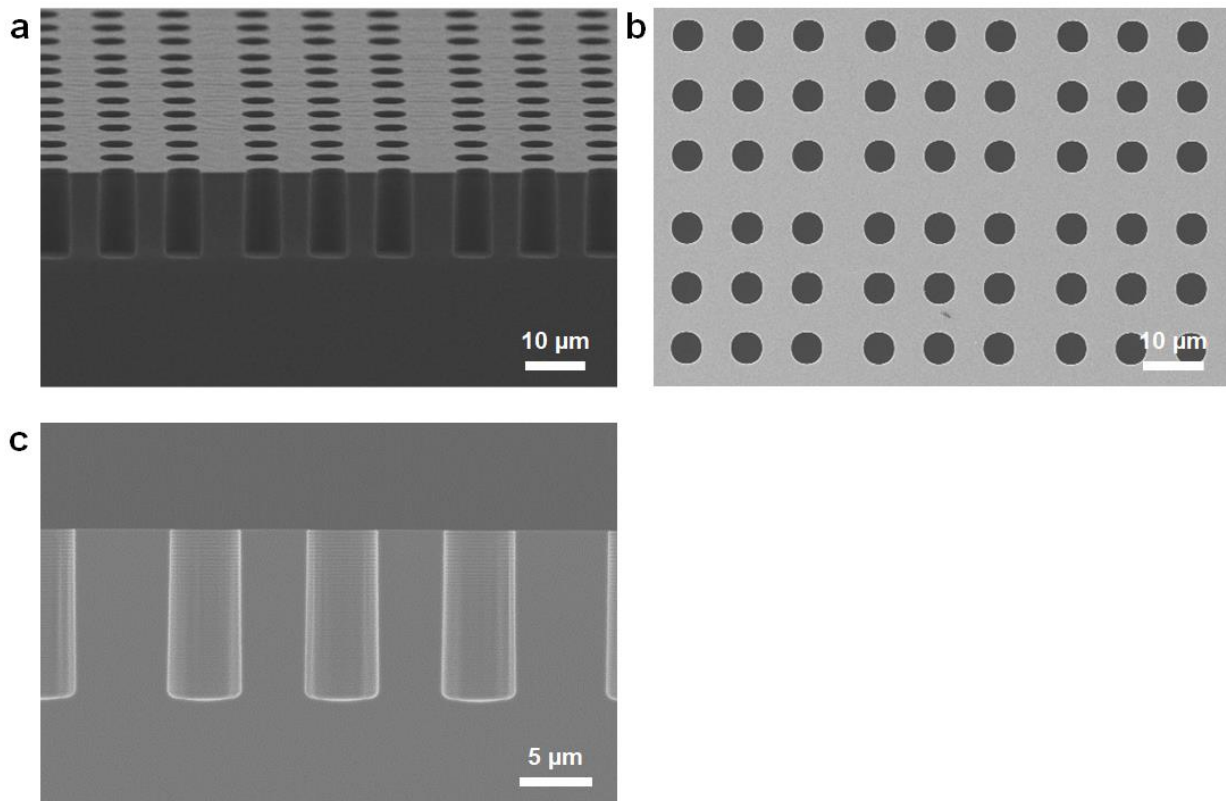
Figure 2.23. *SEM images of through-hole trenches on a Si wafer. (A) An orthogonal view. (B) A top view. (C) A cross-sectional view.*

2.8.2. Fabrication of PDMS stamp

The h-PDMS was prepared by mixing and degassing 17 g of vinyl PDMS pre-polymer (VDT-731), 90 µL of a Pt catalyst (SIP6831.2LC), 250 µL of 2,4,6,8-Tetramethyl-2,4,6,8-tetravinylcyclotetra-siloxane, and 5 g of a hydrosilane pre-polymer (HMS-301). Then, the h-PDMS mixture was poured onto the fabricated Si master mold and cured at room temperature for 12 hours, followed by 2 hours inside an oven at 60 ℃. Thereafter, the stamp was gently demolded from the master mold and cut with a single edge razor blade to obtain nine sets of $1\times1\times1$ cm^3 cubes. After the stamp was cleaned with IPA, it was treated with O_2 plasma using RIE at a plasma power of 40 W, a working pressure of 120 mTorr, and a flow rate of 30 sccm for 20 sec to facilitate subsequent hydrophobic silane coating (anti-stick coating). Then, the stamp was placed in a desiccator with a beaker containing 400 µL of (Tridecafluoro-1,1,2,2-tetrahydrooctyl)trichlorosilane (SIT8174.0) and pumped down for 12 hours at room temperature to allow the stamp's surface to be fully functionalized by the evaporated silane. Finally, the stamp was rinsed with IPA again and gently blow-dried using nitrogen.

2.8.3. PGS prepolymer synthesis

The PGS prepolymer was synthesized according to previously published protocols.[13, 26, 27] Briefly, equimolar glycerol (4.60 g, 50 mmol) and sebacic acid (10.11 g, 50 mmol) were homogenously mixed under nitrogen atmosphere for 24 hours at 120 ℃. Thereafter, the reaction pressure was reduced to <1 mbar while keeping the temperature at 120 ℃ for another 24 hours to allow further condensation polymerization. The PGS prepolymer was a white wax-like solid after it was cooled down to 20 ℃.

2.8.4. Fabrication of PGS scaffold

Approximately 10 mg of PGS pre-polymer solid was placed on a clean and pre-heated Si wafer and melted. Then, the patterned side of the h-PDMS stamp was placed against the liquid PGS on the Si wafer. This apparatus was placed in the vacuum oven (120 ℃ and <1 mbar) for 15 min to remove bubbles between the Si wafer and the stamp. Thereafter, a glass slide plus a 380-gram weight were placed on the stamp to press it against the Si wafer to control the scaffold thickness at room temperature and the apparatus was placed back into the vacuum oven and kept at 120 ℃ for 72 hours under <1 mbar for complete curing of PGS. After that, the Si wafer and the stamp were soaked together in IPA for 12 hours to gently demount the stamp from the Si wafer. Once the stamp was removed, the PGS scaffold on the Si wafer was blow-dried with nitrogen gas and carefully delaminated using a single razor blade. In order to unroll the scaffold tangled during the delamination process and remove any residues on its surface, it was soaked in an IPA solution, followed by a sonication treatment for 20 min. Finally, the PGS scaffold was transferred onto a Teflon plate using a transfer pipet and three drops of water were added on its surface to restore the swollen PGS scaffold to its original morphology. Lastly, it was carefully blow-dried with the cell reservoirs facing upward.

2.8.5. Mounting PGS scaffolds on transwell inserts

A 12-mm polyester transwell membrane with a central 5-mm hole was secured to the scaffold with PDMS. The scaffold was degassed in a desiccator for 5 min and cured at 60 ℃ for 4 hours to adhere the scaffold to the transwell membrane. Then, the PGS scaffold and transwell membrane were carefully detached from the Teflon plate and mounted in a transwell insert for cell culture. Last, for better cell capture, brief (20 sec) oxygen plasma treatment was carried out

on the top and bottom surfaces of PGS scaffold using RIE (Unaxis 790; O_2, 30 sccm; pressure, 120 mtorr; plasma power, 40 W).

2.8.6. Finite element analysis

To predict the mechanical properties of the PGS wineglass and ice cube tray scaffolds, the equivalent von Mises stress distributions were numerically solved using a finite element simulation software (Comsol Multiphysics 4.2, Comsol Ltd). A nonlinear elastic Neo–Hookean model was used to characterize the mechanical properties and the relevant material parameters used for the PGS polymer were E = 1.3 MPa, Density = 1060 kg/m^3, ν = 0.49. Here, E is Young's modulus and ν is Poisson's ratio.

2.9. Conclusion

In conclusion, we have described state-of-the-art microfabrication and micromolding processes for generating biodegradable, micro-structured, ultrathin scaffolds that support formation of a dense layer of hPSC-derived PRs. Analysis of the scaffold's mechanical properties reveal favorable advances in the uniformity of stress distribution and the extent of deformation for optimal scaffold handling in downstream surgical applications. Furthermore, in vitro experiments underscored the potential of ice cube tray scaffolds to serve as an organized delivery system for more than 300,000 hPSC-PRs in a single 5-mm diameter (19.63 mm^2) scaffold (approximately the area of the human macula, see equation 2). PGS ice cube tray PR scaffolds exhibited not only a higher cell payload capacity and decreased biomaterial burden, but also optimal donor PR orientation for integration in transplantation studies. We expect that hPSC-PRs delivered on PGS scaffolds will be better poised to survive and function post-

transplantation and will prevent or eliminate cell reflux and disorganization. Future studies will be aimed at assessing scaffold-mediated delivery in small and large animal models of outer retinal disease and damage, exploring minimally invasive surgical approaches, and optimizing manufacturing strategies for scale-up and Good Manufacturing Practice (GMP) production of PR-seeded scaffolds. In addition, the scaffold micromolding and microfabrication strategies developed here may prove useful for high-density, layered, and oriented cell replacement in other tissues throughout the body.

2.10. References

1. Lee, I.-K. *et al.* Ultrathin micromolded 3D scaffolds for high-density photoreceptor layer reconstruction. *Science Advances* **7,** eabf0344 (2021).

2. Singh, D. *et al.* A biodegradable scaffold enhances differentiation of embryonic stem cells into a thick sheet of retinal cells. *Biomaterials* **154,** 158-168 (2018).

3. Neeley, W. L. *et al.* A microfabricated scaffold for retinal progenitor cell grafting. *Biomaterials* **29,** 418-426 (2008).

4. Ahmed, T. A. E., Ringuette, R., Wallace, V. A. & Griffith, M. Autologous fibrin glue as an encapsulating scaffold for delivery of retinal progenitor cells. *Frontiers in bioengineering and biotechnology* **2,** 85 (2015).

5. Tomita, M. *et al.* Biodegradable polymer composite grafts promote the survival and differentiation of retinal progenitor cells. *Stem cells* **23,** 1579-1588 (2005).

6. McUsic, A. C., Lamba, D. A. & Reh, T. A. Guiding the morphogenesis of dissociated newborn mouse retinal cells and hES cell-derived retinal cells by soft lithography-patterned microchannel PLGA scaffolds. *Biomaterials* **33,** 1396-1405 (2012).

7. Baranov, P., Michaelson, A., Kundu, J., Carrier, R. L. & Young, M. Interphotoreceptor matrix-poly (ϵ-caprolactone) composite scaffolds for human photoreceptor differentiation. *Journal of tissue engineering* **5,** 2041731414554139 (2014).

8. Tucker, B. A. *et al.* The use of progenitor cell/biodegradable MMP2–PLGA polymer constructs to enhance cellular integration and retinal repopulation. *Biomaterials* **31,** 9-19 (2010).

9. Worthington, K. S. *et al.* Two-photon polymerization for production of human iPSC-derived retinal cell grafts. *Acta biomaterialia* **55,** 385-395 (2017).

10.   Thompson, J. R. *et al.* Two-photon polymerized poly (caprolactone) retinal cell delivery scaffolds and their systemic and retinal biocompatibility. *Acta biomaterialia* **94,** 204-218 (2019).

11.   Shrestha, A., Allen, B. N., Wiley, L. A., Tucker, B. A. & Worthington, K. S. Development of high-resolution three-dimensional-printed extracellular matrix scaffolds and their compatibility with pluripotent stem cells and early retinal cells. *Journal of Ocular Pharmacology and Therapeutics* **36,** 42-55 (2020).

12.   Yao, J. *et al.* Enhanced differentiation and delivery of mouse retinal progenitor cells using a micropatterned biodegradable thin-film polycaprolactone scaffold. *Tissue Engineering Part A* **21,** 1247-1260 (2015).

13.   Jung, Y. H. *et al.* 3D microstructured scaffolds to support photoreceptor polarization and maturation. *Advanced materials* **30,** 1803550 (2018).

14.   Polyak, S. The Retina. University of Chicago press. Chicago (1941).

15.   Curcio, C. A., Sloan, K. R., Kalina, R. E. & Hendrickson, A. E. Human photoreceptor topography. *Journal of comparative neurology* **292,** 497-523 (1990).

16.   Lujan, B. J. *et al.* Directional optical coherence tomography provides accurate outer nuclear layer and Henle fiber layer measurements. *Retina (Philadelphia, Pa.)* **35,** 1511 (2015).

17.   Yu, Y. *et al.* Developing a potential retinal OCT biomarker for local growth of geographic atrophy. *Biomedical optics express* **11,** 5181-5196 (2020).

18.   Jonas, J. B., Schneider, U. & Naumann, G. O. Count and density of human retinal photoreceptors. *Graefe's Archive for Clinical and Experimental Ophthalmology* **230,** 505-510 (1992).

19.   Prévot, P.-H. *et al.* Behavioural responses to a photovoltaic subretinal prosthesis implanted in non-human primates. *Nature biomedical engineering* **4,** 172-180 (2020).

20.   Kador, K. E. & Goldberg, J. L. Scaffolds and stem cells: delivery of cell transplants for retinal degenerations. *Expert review of ophthalmology* **7,** 459-470 (2012).

21.   Trese, M., Regatieri, C. V. & Young, M. J. Advances in retinal tissue engineering. *Materials* **5,** 108-120 (2012).

22.   Jones, I., Warner, M. & Stevens, J. Mathematical modelling of the elastic properties of retina: a determination of Young's modulus. *Eye* **6,** 556-559 (1992).

23.   Sharma, R. *et al.* Clinical-grade stem cell–derived retinal pigment epithelium patch rescues retinal degeneration in rodents and pigs. *Science translational medicine* **11,** (2019).

24.   Ghosh, F., Neeley, W. L., Arnér, K. & Langer, R. Selective removal of photoreceptor cells in vivo using the biodegradable elastomer poly (glycerol sebacate). *Tissue Engineering Part A* **17,** 1675-1682 (2011).

25. Redenti, S. *et al.* Engineering retinal progenitor cell and scrollable poly (glycerol-sebacate) composites for expansion and subretinal transplantation. *Biomaterials* **30,** 3405-3414 (2009).

26. Rai, R., Tallawi, M., Grigore, A. & Boccaccini, A. R. Synthesis, properties and biomedical applications of poly (glycerol sebacate)(PGS): A review. *Progress in polymer science* **37,** 1051-1078 (2012).

27. Wang, Y., Ameer, G. A., Sheppard, B. J. & Langer, R. A tough biodegradable elastomer. *Nature biotechnology* **20,** 602-606 (2002).

28. Hynes, S. R. & Lavik, E. B. A tissue-engineered approach towards retinal repair: scaffolds for cell transplantation to the subretinal space. *Graefe's Archive for Clinical and Experimental Ophthalmology* **248,** 763-778 (2010).

29. Zhang, H., Jackson, J. K. & Chiao, M. Microfabricated drug delivery devices: Design, fabrication, and applications. *Advanced Functional Materials* **27,** 1703606 (2017).

30. Franssila, S., Kiihamäki, J. & Karttunen, J. Etching through silicon wafer in inductively coupled plasma. *Microsystem technologies* **6,** 141-144 (2000).

31. Wu, B., Kumar, A. & Pamarthy, S. High aspect ratio silicon etch: A review. *Journal of applied physics* **108,** 9 (2010).

32. Laermer, F., Franssila, S., Sainiemi, L. & Kolari, K. Deep reactive ion etching. *Handbook of silicon based MEMS materials and technologies*. Elsevier, 2020, pp 417-446.

33. Kim, M. J., Hwang, M. Y., Kim, J. & Chung, D. J. Biodegradable and elastomeric poly (glycerol sebacate) as a coating material for nitinol bare stent. *BioMed research international* **2014,** (2014).

34. Liu, M., Wang, S. & Jiang, L. Nature-inspired superwettability systems. *Nature Reviews Materials* **2,** 1-17 (2017).

35. Jo, H., Park, H. S. & Kim, M. H. Single bubble dynamics on hydrophobic–hydrophilic mixed surfaces. *International Journal of Heat and Mass Transfer* **93,** 554-565 (2016).

36. Capowski, E. E. *et al.* Reproducibility and staging of 3D human retinal organoids across multiple pluripotent stem cell lines. *Development* **146,** dev171686 (2019).

37. Gasparini, S. J., Llonch, S., Borsch, O. & Ader, M. Transplantation of photoreceptors into the degenerative retina: Current state and future perspectives. *Progress in retinal and eye research* **69,** 1-37 (2019).

38. Pearson, R. A. *et al.* Restoration of vision after transplantation of photoreceptors. *Nature* **485,** 99-103 (2012).

39. Stuck, M. W., Conley, S. M. & Naash, M. I. PRPH2/RDS and ROM-1: Historical context, current views

and future considerations. *Progress in retinal and eye research* **52,** 47-63 (2016).

40.   Liu, Z., Yu, N., Holz, F. G., Yang, F. & Stanzel, B. V. Enhancement of retinal pigment epithelial culture characteristics and subretinal space tolerance of scaffolds with 200 nm fiber topography. *Biomaterials* **35,** 2837-2850 (2014).

41.   Alexander, J., Bradley, J., Gabourel, J. & Acott, T. Expression of matrix metalloproteinases and inhibitor by human retinal pigment epithelium. *Investigative ophthalmology & visual science* **31,** 2520-2528 (1990).

Chapter 3. Third generation honeycomb-shaped scaffolds for outer retinal layer reconstruction

3.1. Introduction

Recent engineering advances have produced an RPE scaffold (or patch), which is comprised of a fully differentiated, human embryonic stem cell (hESC)–derived RPE monolayer on a coated, synthetic basement membrane, and demonstrated the feasibility and safety of hESC-RPE scaffold transplantation as a regenerative strategy for early-stage AMD.[1, 2] Over the last few years, our research team also generated biocompatible and biodegradable PR scaffolds with arrays of 3D microstructures (i.e., "wine glass"[3] and "ice cube tray"[4]) using a thermo-curable polymer (i.e., poly(glycerol sebacate), PGS) and succeeded in creating scaffolds that support the formation of a dense layer of hPSC–derived PRs. However, as of yet, there is no study for delivering PR+RPE bilayer on a single scaffold, which is required to treat advanced AMD, the last stage of macular degeneration. Since those aforementioned scaffolds were originally only designed to deliver either PRs or RPE cells individually, a new scaffold design plus optimizations on the scaffold fabrication processes need to be further developed in order to generate a scaffold enabling the bilayered delivery of PR+RPE cells.

Here, we propose a "honeycomb"-shaped, microfabricated outer retinal scaffold, herein termed as "microscaffold," in order to achieve delivery of PR+RPE bilayer. The honeycomb design is adopted as a shape of cell capture wells loading and delivering the dual PR+RPE construct in the microscaffold to improve mechanical characteristics in regards to the maintenance of the structural integrity, which enables mass production by improving the production yield of fabrication. Furthermore, we engineer and optimize the elastomeric stamp material (i.e., polydimethylsiloxane, PDMS) to fine-tune the mechanical properties of PDMS

stamps. We also develop the scaffolding material (i.e., PGS) and the curing process to drastically speed up the manufacture of PGS scaffolds from days (via thermo-curing) to minutes (via photocuring). We describe simultaneous development and optimization of (1) the morphology (i.e., shape and sizes) of the 3D micropatterns (i.e., scaffold design), (2) the formulation and curing process of the scaffolding elastomers (i.e., materials optimization), and (3) the scaffold fabrication processes (i.e., good manufacturing practices (GMP)-compliant process development).

3.2. Scaffold design

As shown in Figure 3.1, the structure of microscaffolds is composed of two critical layers: (1) hexagonal prism-shaped cell capture wells (white) in the top layer in which seeded cells can be captured and retained, and (2) cylinder-shaped fluid channels (orange) in the bottom layer which are employed to support RPE functions such as water, waste, and metabolite transports during the scaffold degradation.

For efficient cell capture and retention, the microscaffolds were designed by considering the following parameters: (1) Each honeycomb-shaped cell capture well should have enough volume and depth (i.e., ~ 40 µm) to fit all of the seeded cells (i.e., PRs and RPE cells) and minimize cell migration outside of the wells. (2) The diameter of each cylindrical fluid channel should be narrow enough (i.e., ≤ 5 µm) to prevent the cells from slipping through the channels. (3) The wall width of the cell capture wells should be thin enough (i.e., ≤ 4 µm) to keep the cells from sitting on the top of the walls. (4) Since the microscaffolds contain/carry a considerable amount of cells (over 100 cells per well), the thickness of the scaffold base (i.e., fluid channel layer) should be thick enough (i.e., ~ 10 µm) to make the scaffolds rigid so that surgeons can easily

handle the scaffold constructs during transplantation procedures. (5) An aspect ratio of the cell capture wells (i.e., the ratio of their width to their depth) can significantly affect the scaffold micromolding processes.[5] For instance, the microstructures of a PDMS stamp with a high aspect ratio (i.e., > 1) can be broken while demolding the stamp from a Si master (Figure 3.2). Thus, the side length of cell capture wells should be long enough (i.e., > 40 μm) to reduce its aspect ratio under 1.
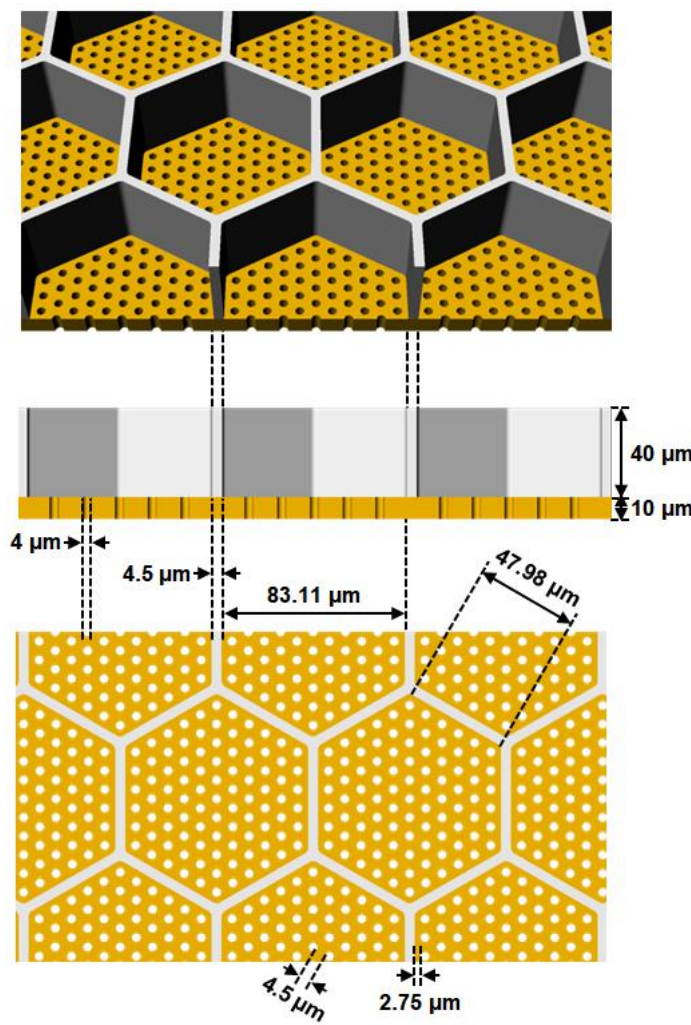

Figure 3.1. *Schematic illustration of the honeycomb-shaped microscaffold. Detailed dimensions of the fluid channel layer (white in color) and the cell capture well layer (orange in color) are as shown.*
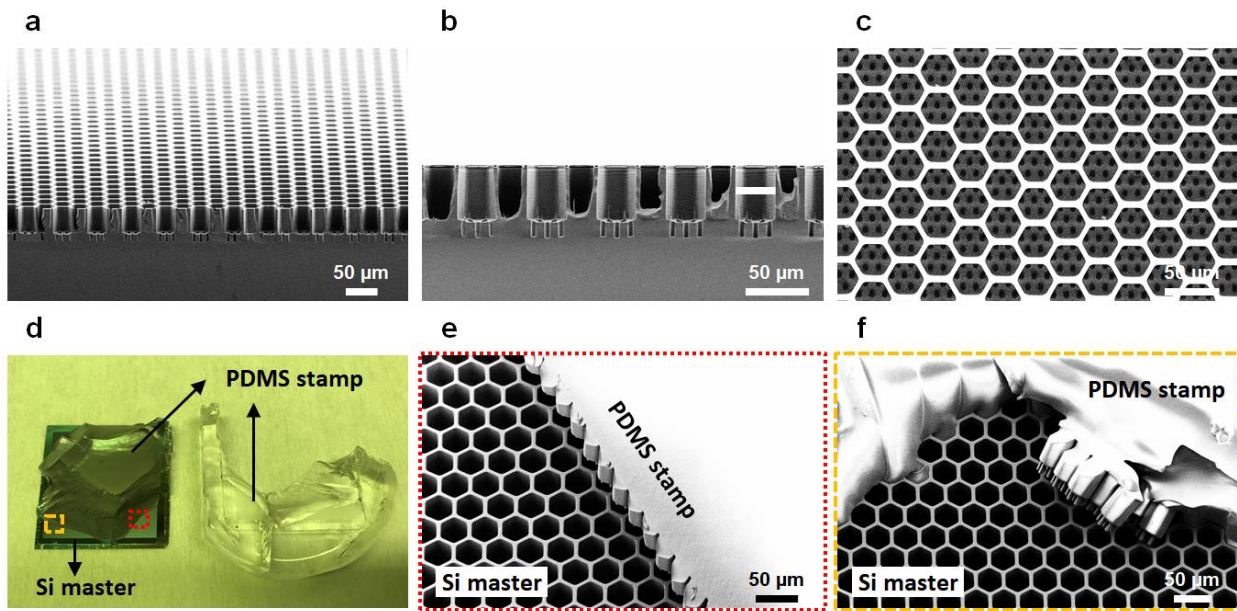
Figure 3.2. *a-c) SEM images of a honeycomb-shaped Si master with an aspect ratio of 2.94 (The side length and depth of a cell capture well are 13.62 μm and 40 μm, respectively): a) orthogonal view, b) cross-sectional view, and c) top view. d) Low-magnification photographic image depicting the demolding failure of the PDMS stamp from the Si master. e,f) SEM images of the PDMS stamp and Si master showing the broken microstructures of the PDMS stamp after demolding due to its high aspect ratio.*

3.3. Scaffold manufacturing process

Figure 3.3 shows the procedure of creating a Si master, a PDMS stamp, and a PGS microscaffold. Essentially, the fabrication process flow for making honeycomb-shaped microscaffolds is similar to that of making our previous ice cube tray-shaped PR scaffolds.[4] However, it was found that the changes in morphology and size of the scaffold caused a lot of issues in each scaffold fabrication step. Thus, we newly developed and further optimized the

microfabrication and micromolding techniques by introducing new fabrication processes (e.g., stamp delamination process), and re-engineering process parameters (e.g., time and temperature) and molding materials (e.g., hybrid-PDMS and photocurable PGS) to address the challenges that occurred while producing the newly designed scaffold.
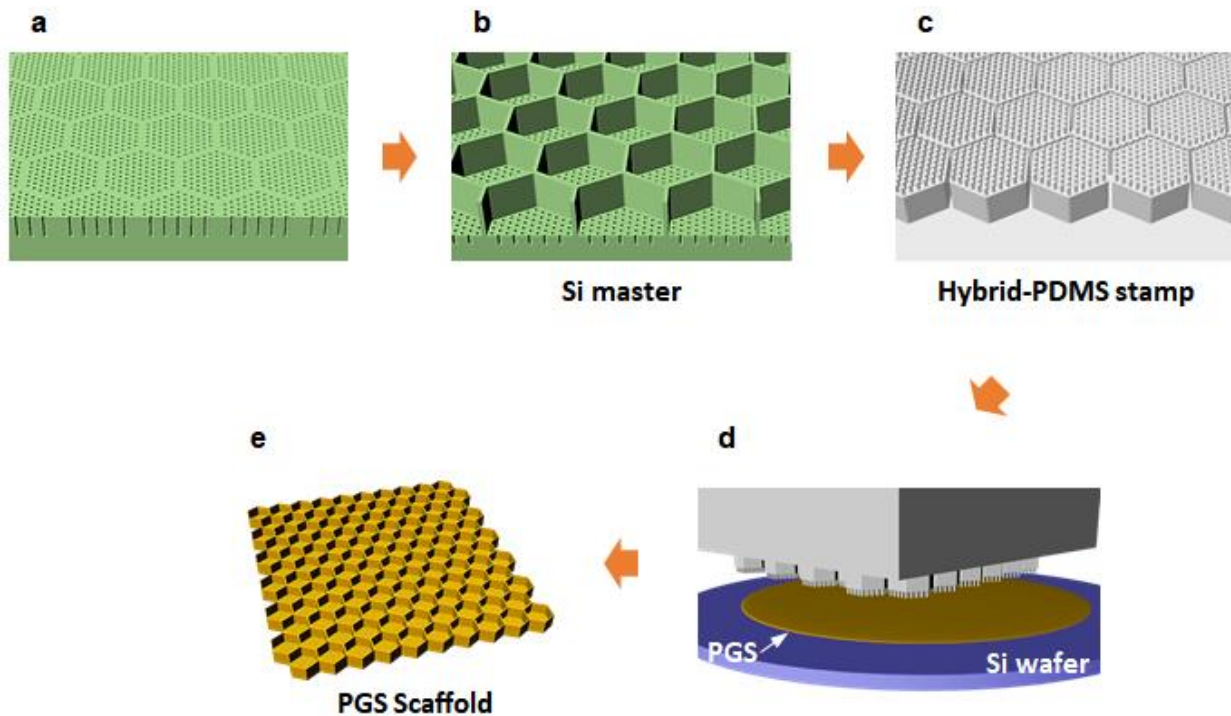
Figure 3.3. *Schematic of the procedure for generating a Si master, a hybrid-PDMS stamp, and a photocurable PGS-based microscaffold. a) Fluid channel- and b) cell capture well-etching processes for creating a Si master. c) Hybrid-PDMS stamp demolded from the Si master. d) The hybrid-PDMS stamp is mounted on liquid PGS on a Si wafer, and after photocuring of the PGS, the stamp is demounted from the scaffold by a sonication in IPA solution. e) Completed honeycomb-shaped microscaffold.*

3.3.1. Fabrication of Si master

In this study, the honeycomb-shaped microscaffold was designed to have deeper cell capture wells (~40 µm in depth) than our previous ice cube tray PR scaffold (~25 µm in depth).[4] In order to produce the Si master for the honeycomb-shaped microscaffold, we increased the deep reactive ion etching (DRIE) cycles to form deeper wells for cell capture. However, this resulted in shallow fluid channels (~3 µm), which is far shallower than our target depth (~10 µm) of the fluid channels (Figure 3.4).
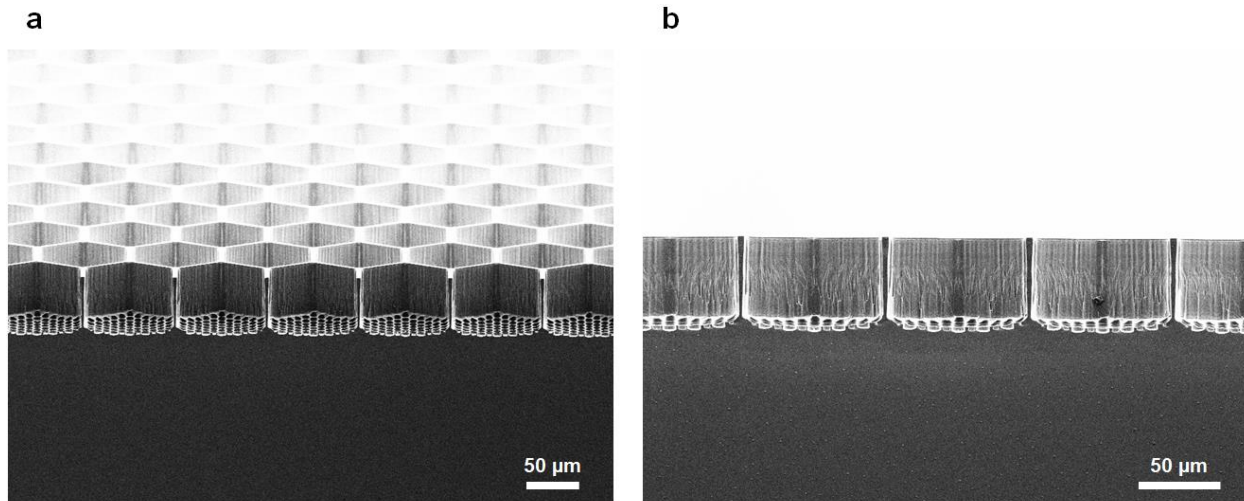
*Figure 3.4. SEM images of the fabricated Si master with shallow fluid channels (~3 µm): a) orthogonal view and b) cross-sectional view.*

To resolve this problem, deeper trenches of the fluid channels were alternatively made before etching the cell capture wells. However, unexpectedly, this alternative approach caused another issue. The photoresist (AZ2070; negative resist) in the fluid channel trenches was not

completely removed during the development process, defining the cell capture well patterns, and remained in the trenches (Figure 3.5) as the trenches were too deep (28 µm in depth) and narrow (4 µm in diameter).
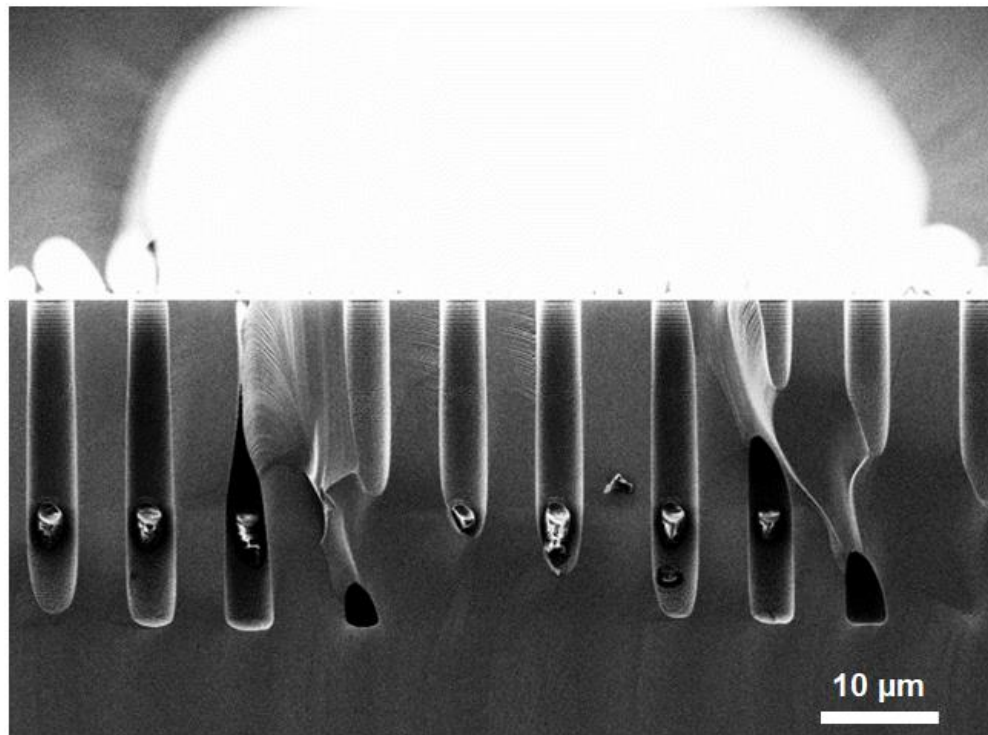
Figure 3.5. *SEM image of fluid channel trenches on a Si wafer. Photoresist residues still remained in the fluid channel trenches after the photoresist development process (40 sec of development time).*

In order to completely get rid of the remaining photoresist in the trenches, the development process time needs to be increased, but in reality, increasing the time may cause the over-development of photoresist, which negatively affects the line width[6] (e.g., the wall width of the cell capture wells would become thinner so that the scaffold could be easily torn during

micromolding processes). Therefore, we further optimized the process parameters of photolithography to address this challenge. To be specific, we deliberately over-exposed the photoresist to the ultraviolet (UV) light (365 nm) and substantially increased the processing time (1 min to 3 min) and temperature (110 ℃ to 120 ℃) of the post-exposure bake. With this optimization, we finally succeeded in drastically increasing the development process time (40 sec to 480 sec) without affecting the line width, and ultimately removing the remaining photoresist residues in the fluid channel trenches (Figure 3.6). Additionally, we conducted some extra processes, including a hard-bake (130 ℃, 2 min), a CF4 Si etching (20 sec), and an oxygen plasma treatment (1 min), to ensure that there is no remaining photoresist in the trenches before the cell capture well-etching process.
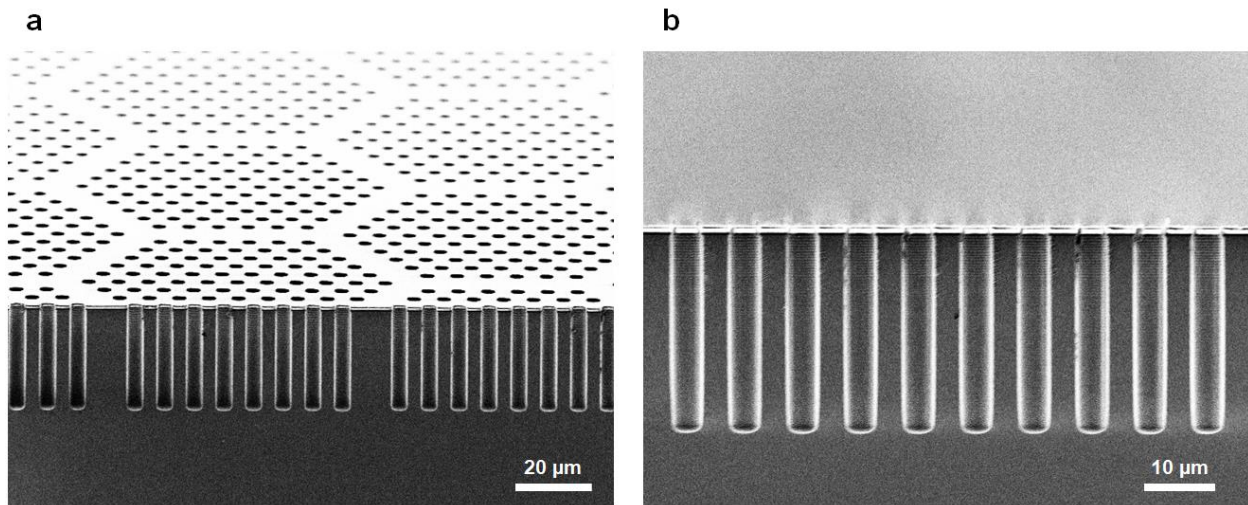

Figure 3.6. *SEM images of fluid channel trenches on a Si wafer showing a) a orthogonal view and b) a cross-sectional view, respectively. The remaining photoresist residues in the fluid channel trenches were completely removed by increasing the development time from 40 sec to 480 sec.*

Figure 3.7 shows scanning electron microscopy (SEM) images of the resulting Si master. The Si master was free of defects and had clean surfaces in its microstructures. The dimensions of the key features of the fabricated Si master were as follows: (1) The diameter and depth of the fluid channels were 4.1 μm and 10.2 μm, respectively. (2) The side length and depth of the cell capture wells were about 48.1 μm and 40.1 μm, respectively. (3) The wall width of the cell capture wells was 4.5 μm and the distance between adjacent fluid channels was 4.5 μm. For an efficient micromolding process to create a PDMS stamp in the next fabrication step, a Teflon-like polymer film with long linear $(CF_2)_n$ chains, was coated on the Si master by DRIE-mediated plasma-polymerization of octafluorocyclobutane (C_4F_8).[7] Thus, the Si master surface became chemically inert and hydrophobic. The detailed fabrication processes for generating the Si master are described in the experimental section.
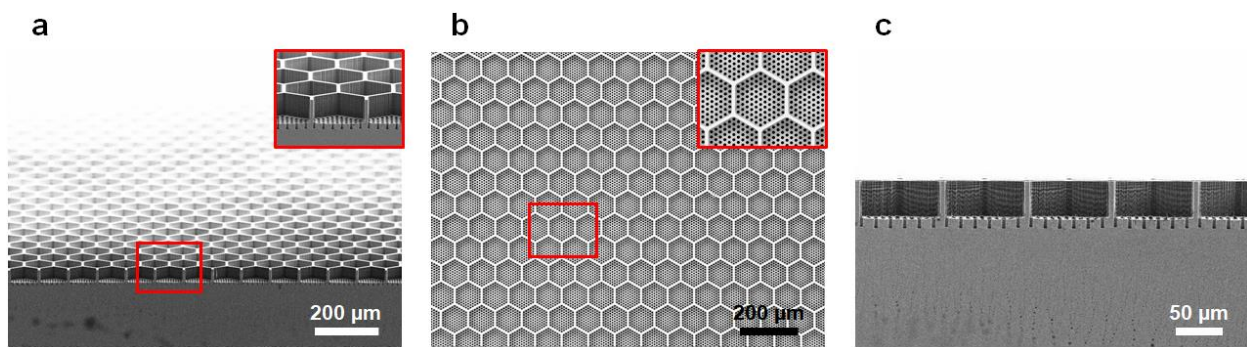

Figure 3.7. *SEM images of the fabricated Si master showing a) a tilted view, b) a top view, and c) a cross-sectional view, respectively. The inset images show a magnified view of the microstructures of the fabricated Si master mold.*

3.3.2. Fabrication of PDMS stamp

PDMS stamps in soft lithography should not only be mechanically stable for a successful

micromolding process (e.g., it should not be broken while demolding the stamp from the Si master or overly crooked by the pressure caused by weights when making the scaffold), but also be able to form a conformal contact with a substrate to make the fluid channels of the scaffolds fully open. Thus, two characteristics, stiffness and elasticity, need to be considered simultaneously and finely attuned to make a stamp with appropriate mechanical properties for a perfect micromolding process. In this work, hard-PDMS (SYLGARD® 184), which had been used in our previous work, was used as a stamp material to create a stamp that is not deformed during a micromolding process. Figure 3.8a presents an SEM image of the hard-PDMS stamp demolded from the Si master. Unlike the successful demolding of the stamp in our previous work, demolding the stamp from the new Si master with honeycomb design failed. The micropillars of the hard-PDMS stamp were broken while demolding due to both the brittle nature of the hard-PDMS and the high aspect ratio (~2.49) of the micropillar structures which make the micropillars prone to fracture during the demolding process. Because the aspect ratio of the micropillars is crucial to maintain the scaffold's desirable dimension for the delivery of dual PR+RPE construct, we sought to tune the mechanical properties of the stamp materials. We hypothesized that a hybrid-PDMS can be formed by curing a mixture of the hard-PDMS and the soft-PDMS, given the fact that both types of PDMS undergo the same mechanism for chemical crosslinking under catalysis of Karstedt's catalyst. Therefore, the hybrid-PDMS was alternatively employed as a stamp material, and parameters including the mixing ratio of the hard-PDMS and the soft-PDMS, the curing time, and the curing temperature were optimized to get the desired mechanical characteristics of the PDMS stamp (Figure 3.8b-h). Since in our preliminary study, it was found that the hard-PDMS is very sensitive to heat when it is cured (e.g., the hard-PDMS became too brittle when cured at 60 ℃ for 2 hours), the hybrid-PDMS was first cured at room temperature,

and then cured at higher temperatures in an oven. The empirically determined optimal mixing ratio, curing temperature, and curing time were 1:4 (hard-PDMS:soft-PDMS) and 25 ℃ for 12 hours followed by 60 ℃ for 2 hours, respectively.
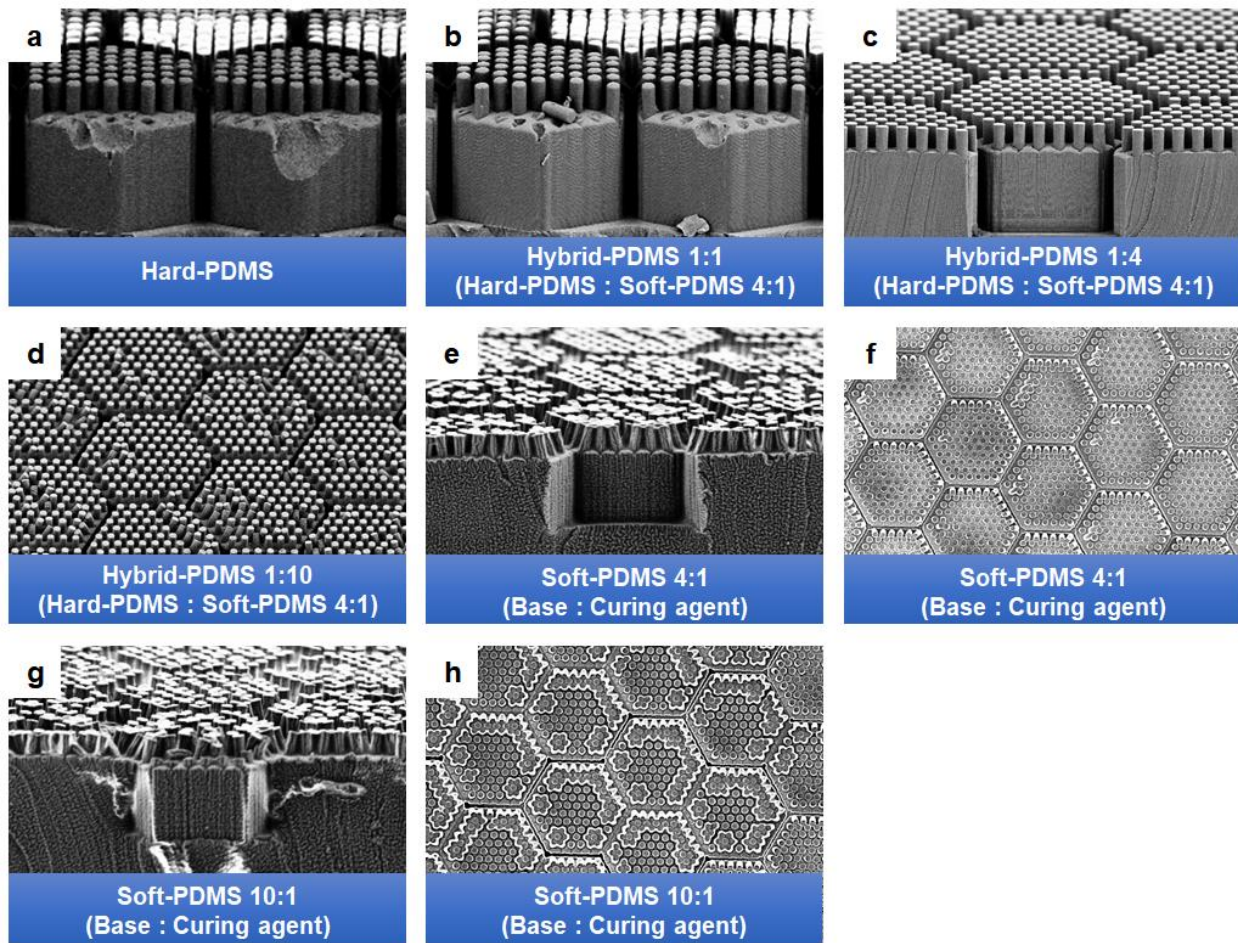
Figure 3.8. *a) SEM image of a hard-PDMS stamp. SEM images of hybrid-PDMS stamps with mixing ratios of b) 1:1, c) 1:4, and d) 1:10 between hard-PDMS and soft-PDMS, respectively. SEM images of a soft-PDMS stamp with a mixing ratio of 4:1 (base : curing agent) showing g) a tilted view and f) a top view, respectively. SEM images of a soft-PDMS stamp with a mixing ratio of 10:1 (base : curing agent) showing g) a tilted view and f) a top view, respectively.*

From the further assessment of the mechanical properties of each stamp material (Figure 3.9 and Table 3.1), the hybrid-PDMS 1:4 showed the most appropriate mechanical properties (Young's modulus: 1.46 Mpa and elongation at break: 60.5 %) in terms of stiffness and elasticity for micromolding processes.
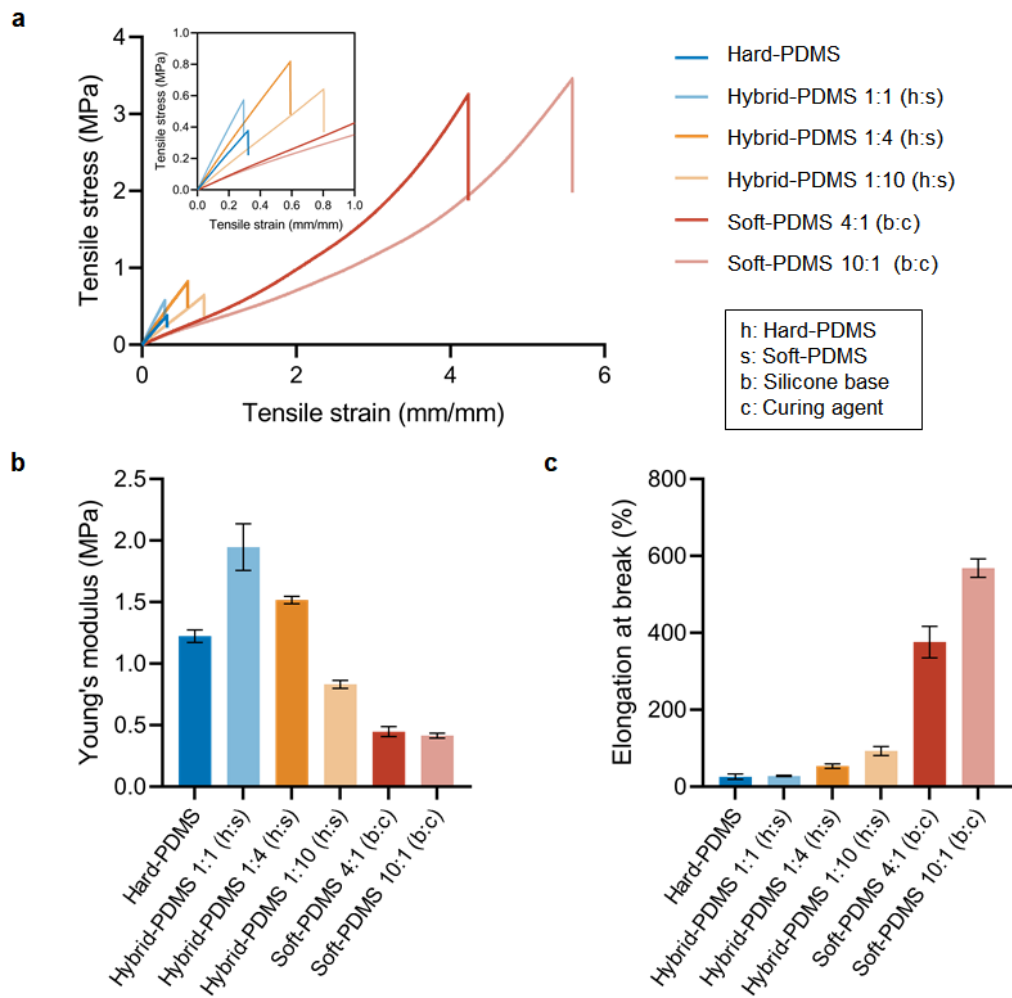

Figure 3.9. *Mechanical tests of Hybrid-PDMS. (a) The stress-strain curves of the hybrid-PDMS prepared with different ratios of the hard-PDMS to the soft-PDMS. Three replicates were measured for each formulation and (b) the Young's modulus and (c) the elongation at break were calculated. The formulation details were listed in Table 3.1.*

PDMS #	Stamp materials	Status of stamp's microstructures after demolding a stamp from a Si master	Young's modulus (Mpa)	Elongation at break
1	Hard-PDMS	The stamps were brittle and lacked sufficient elasticity so that some of the micro-pillars were broken while demolding	1.22	26%
2	Hybrid-PDMS 1:1 (Hard-PDMS : Soft-PDMS 4:1)	The stamps were too stiff and lacked sufficient elasticity so that some of the micro-pillars were broken while demolding.	1.95	28%
3	Hybrid-PDMS 1:4 (Hard-PDMS : Soft-PDMS 4:1)	The stamp showed an appropriate level of stiffness and softness for molding processes	1.52	53%
4	Hybrid-PDMS 1:10 (Hard-PDMS : Soft-PDMS 4:1)	The stamp was somewhat soft, thus some of stamp's micro-pillar structures attached to each other	0.83	93%
5	Soft-PDMS 4:1 (Base : Curing agent)	The stamp was quite soft and sticky, therefore many micro-pillars of the stamp were attached to each other	0.45	376%
6	Soft-PDMS 10:1 (Base: Curing agent)	The stamp was too flexible and sticky, so that the honeycomb microstructures of the stamp were attached to each other	0.42	568%

Table 3.1. *Comparison of the mechanical properties of PDMS materials with different mixing ratios.*

Figure 3.10 shows the SEM images of the successfully fabricated hybrid-PDMS stamp. The stamp was successfully demolded from the Si master without leaving any defects or notable residues on its microstructures. After demolding, the stamp's surface was treated with oxygen plasma using reactive ion etching (RIE) to facilitate the subsequent hydrophobic and anti-stick silane coating. The detailed process for generating the hybrid-PDMS stamp is described in the experimental section.
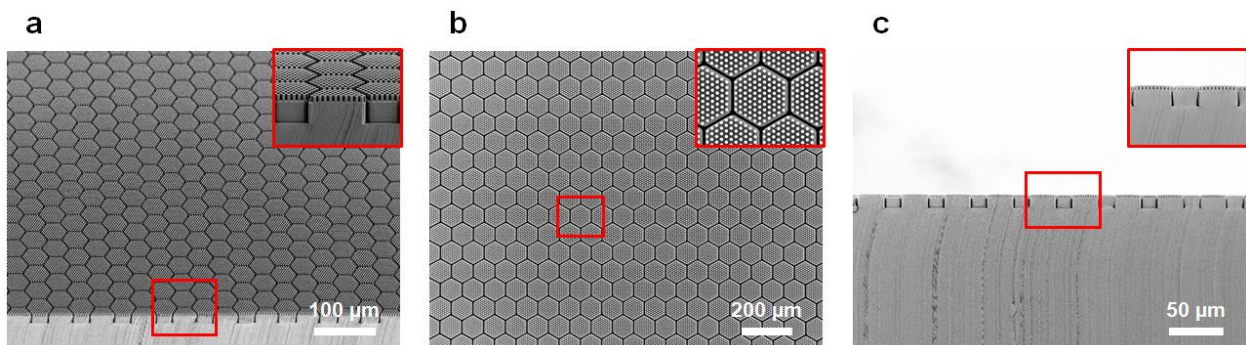
Figure 3.10. *SEM images of the fabricated hybrid-PDMS stamp showing a) a tilted view, b) a top view, and c) a cross-sectional view, respectively. The inset images show a magnified view of the microstructures of the fabricated hybrid-PDMS stamp.*

3.3.3. Preparation, optimization, and characterization of photocured PGS

PGS is a biocompatible and biodegradable polyester elastomer with good manufacturability and sufficient mechanical strength.[8, 9] Our previous scaffolds with wine-glass and ice-cube tray designs were thus fabricated using PGS as their scaffolding material.[3, 4] However, during the micromolding process, the original PGS prepolymer (i.e., the uncured PGS with low molecular weight) needs to be cured at 120°C and under high vacuum for 3-4 days to allow complete polycondensation. This thermo-curing process is time-consuming and requires high temperature and high vacuum, which may limit its scale-up manufacturability. We thus hypothesized that by conjugation of photocurable groups to the PGS prepolymer, we would be able to cure the PGS by UV, which does not need to be cured at a high temperature and a high vacuum and can drastically reduce the curing time from days to minutes.[10-12] As shown in Figure 3.11a, methacrylate groups were selected for photocuring of PGS via photo-initiated free-radical polymerization. Compared with other photocurable groups, methacrylate groups offer better chemical stability than acrylate groups and do not need the addition of thiolate molecules, unlike

norbornene groups. The photocurable PGS prepolymer was synthesized by esterification between methacrylic anhydride and hydroxyl groups on the PGS prepolymer. The chemical structure of the photocurable PGS prepolymer was verified by 1H-NMR with methacrylation of ~20% (Figure 3.12).
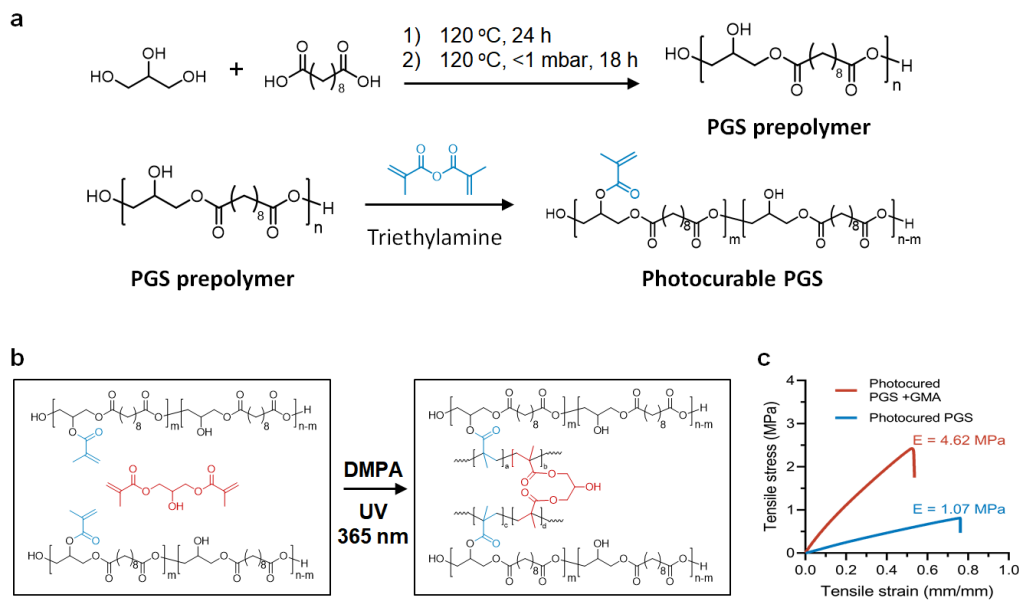

Figure 3.11. *Synthesis and characterization of the photocurable PGS prepolymer and photocured PGS. a) The synthesis schemes of the photocurable PGS prepolymer. The PGS prepolymer was first synthesized by polycondensation of glycerol and sebacic acid. Thereafter, the photocurable PGS prepolymer was synthesized by esterification between hydroxyl groups on PGS and methacrylic anhydride. b) Under UV at 365 nm and initiated by DMPA, the photocurable PGS prepolymer can be efficiently cured within 5 minutes,[11] with or without the addition of GMA. c) Stress-strain curves of the photocured PGS with or without 10 wt% of GMA. The result indicated that the addition of GMA significantly increased the Young's modulus of the photocured PGS from 1.07 MPa to 4.62 MPa due to its higher crosslinking density.*
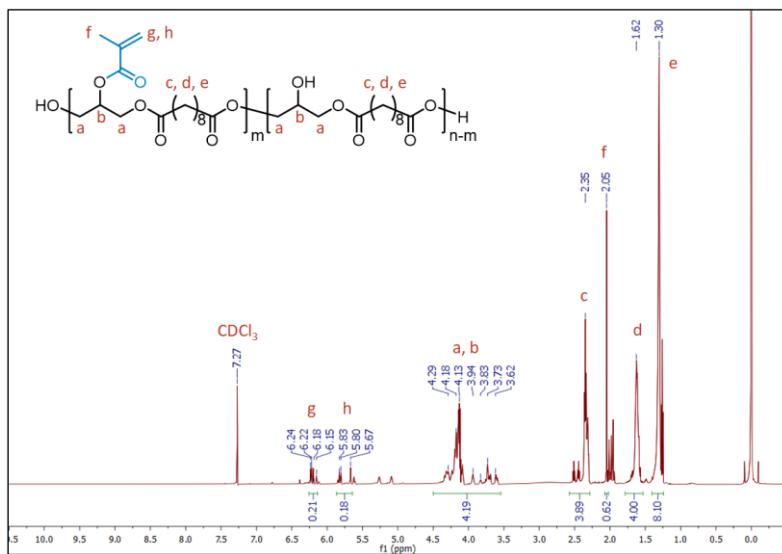
Figure 3.12. *1H-NMR spectrum of the photocurable PGS prepolymer. The degree of methacrylation was determined at 20%.*

Under UV (365 nm, 10 mW/cm^2), the photocurable PGS can be efficiently cured with the existence of 2,2-dimethoxy-2-phenylacetophenone (DMPA, the photoinitiator) (Figure 3.11b).[11] However, in our preliminary study, it was found that the photocured PGS was not as tough as the thermo-cured PGS, leading to difficulties in demounting the stamp from the scaffold without causing defects on the scaffold's microstructures (Figure 3.13a). Therefore, to enhance the mechanical strength of the photocured PGS, glycerol dimethacrylate (GMA) was blended with the photocurable PGS prepolymer prior to the photocuring process to increase the crosslinking density.[13, 14] The GMA was selected because it is highly unlikely to affect the biocompatibility and biodegradability of the photocured PGS scaffold due to the fact that the degradation products of GMA are the same as those of photocurable PGS. The optimal blending ratio of GMA was empirically determined, and 10 wt% of GMA showed satisfactory

mechanical properties of the photocurable PGS as a scaffolding material (Figure 3.13b-d). Mechanical tests revealed that the GMA significantly increased the Young's modulus of the photocured PGS from 1.07 MPa to 4.62 MPa and decreased the elongation at break of the photocured PGS from 76% to 52% (Figure 3.11c).
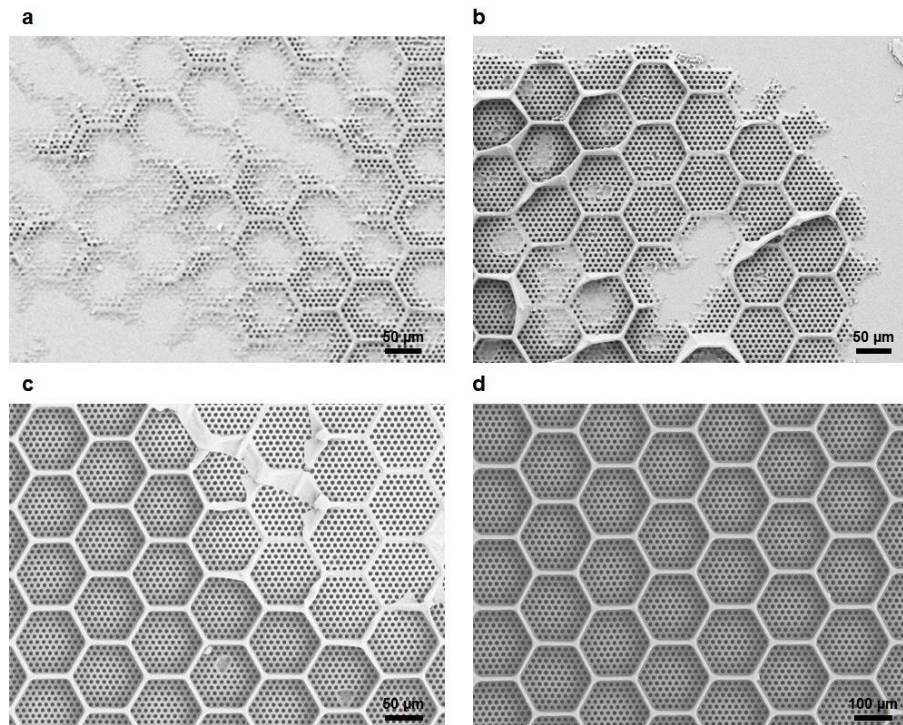
Figure 3.13. *SEM images of the photocured PGS scaffolds fabricated using photocurable PGS prepolymer blended with a) 0 wt% of GMA, b) 2.5 wt% of GMA, c) 5 wt% of GMA, and d) 10 wt% of GMA, respectively. The photocured PGS without GMA was not as tough as the original thermo-cured PGS, so that considerable defects were made on the scaffold microstructures after demounting the stamp from the scaffold. The addition of GMA gradually improved the integrity of the scaffolds' microstructures and 10 wt% of GMA led to the successful fabrication of scaffolds without leaving apparent defects on the scaffold microstructures.*

3.3.4. Fabrication of photocured PGS microscaffolds

Despite the outstanding mechanical properties of the photocurable PGS, an issue occurred while generating the photocurable PGS microscaffolds, which was that some of the honeycomb-shaped cell capture wells were torn while manually demounting the stamps from the scaffolds (Figure 3.14).
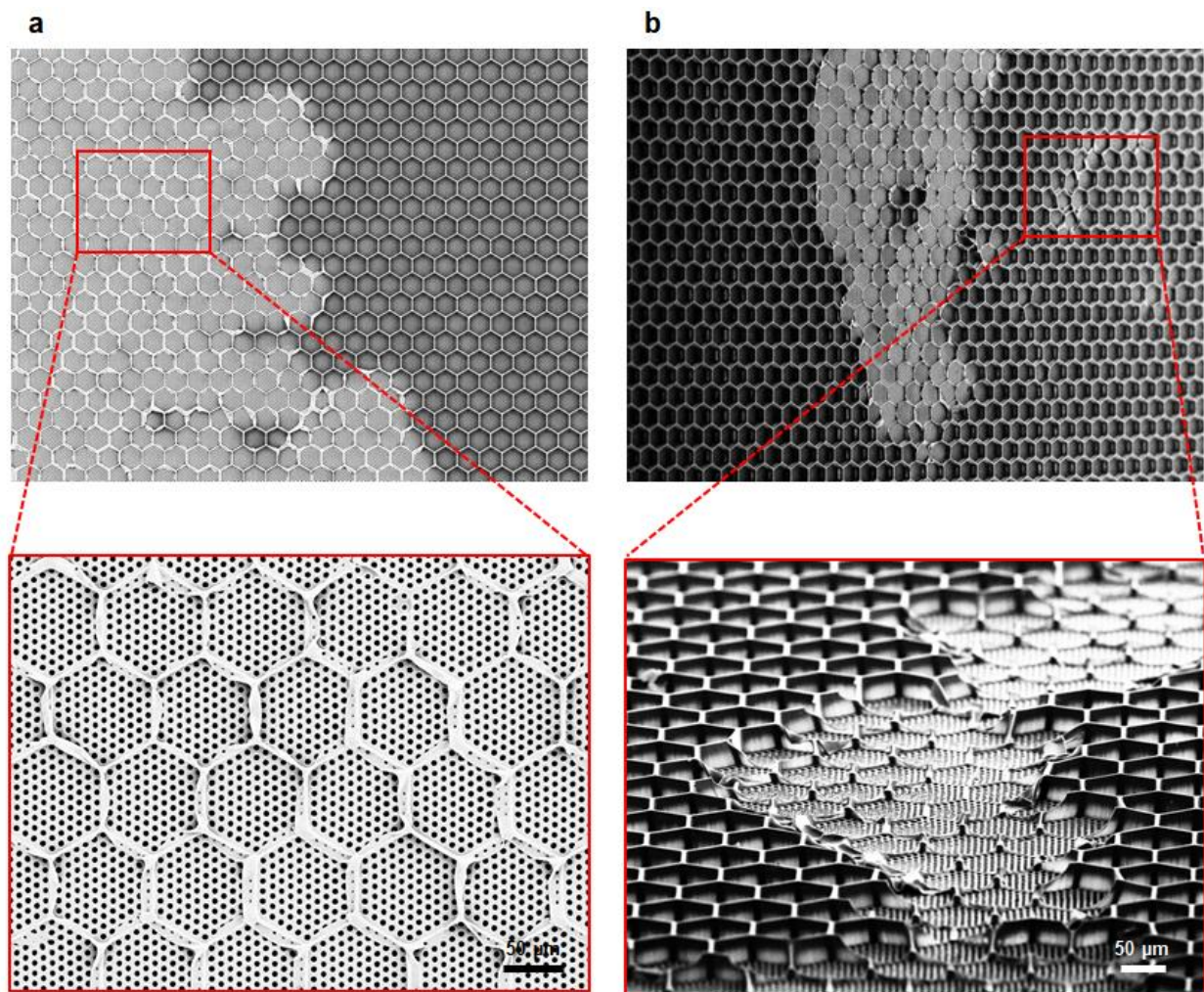

Figure 3.14. SEM images of the fabricated microscaffold with some of its cell capture wells torn after manually demounting the stamp from the scaffold: a) top view and b) tilted view.

Considering that all of the cell capture wells of the ice cube tray-shaped PGS scaffolds, which were fabricated in a similar size (L/W/H = 50/50/40 µm) to the microscaffolds in order to compare the production yield of scaffolds, were torn after demounting (Figure 3.15), we were able to see that the honeycomb microstructures certainly contributed to the demounting process.
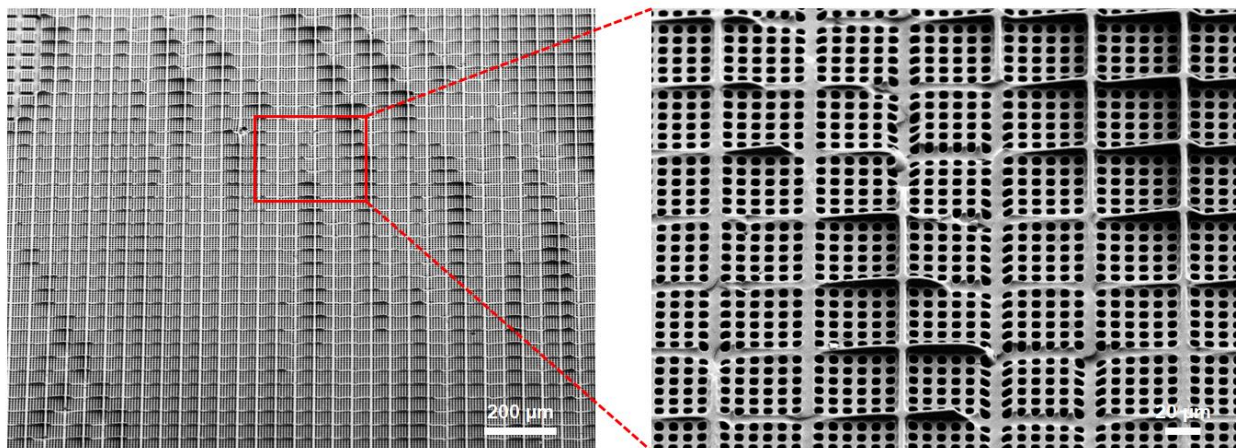
Figure 3.15. *SEM images of the ice cube tray-shaped scaffold with all of its cell capture wells torn after manually demounting the stamp from the scaffold: a) top view and b) tilted view.*

Having said that, however, since manually demounting the stamps from the scaffolds cannot ensure the sustainable production of scaffolds with a high yield, a new stamp demounting method−stamp cutting processes followed by a sonication-treatment in isopropanol (also known as isopropyl alcohol or IPA)−was introduced. Figure 3.16 describes the procedures of demounting a hybrid-PDMS stamp from a photocured PGS microscaffold.
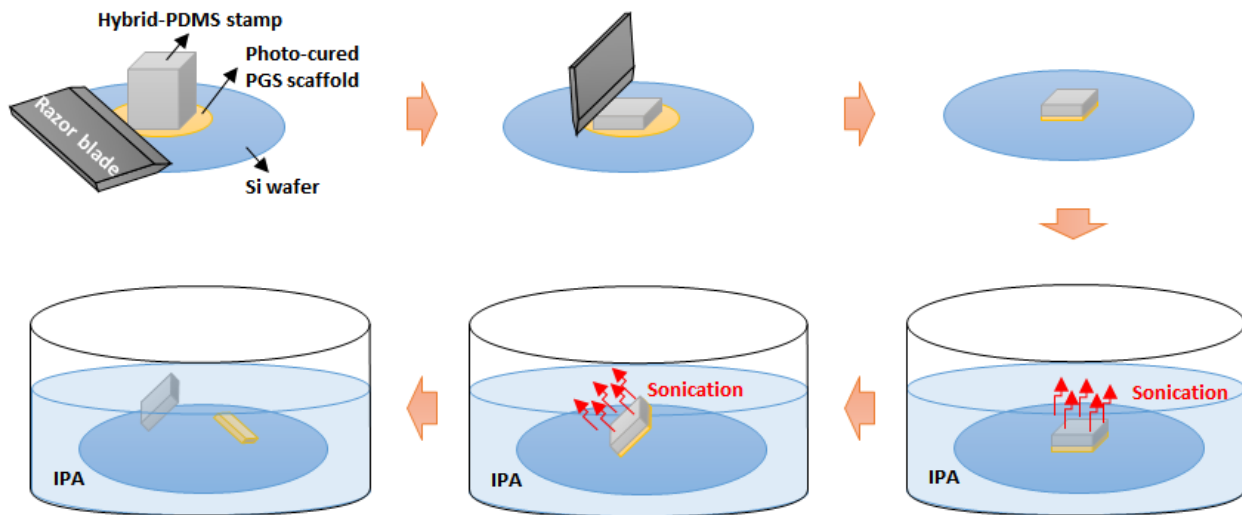
Figure 3.16. *Schematic illustration of the new stamp demounting method. In order to facilitate the scaffold delamination, the stamp was cut horizontally and then vertically using a razor blade, followed by a sonication-treatment in isopropanol for 4 hours.*

First, the stamp on the scaffold was cut horizontally to make it thinner so that the stamp can be more easily demounted from the scaffold during the sonication process in isopropanol. Then, the four sides of both the stamp and scaffold were vertically cut and removed to let the isopropanol more quickly permeate the PGS polymer so that the PGS scaffold can be smoothly detached from the Si wafer during the sonication process in isopropanol. Then, the whole apparatus (i.e., Si wafer, microscaffold, stamp) was immersed in isopropanol and sonication-treated for 4 hours. Within the first 2 hours, both the microscaffold and stamp were separated from the Si wafer, and then the microscaffold was demounted from the stamp within the next 2 hours. Figure 3.17 shows the SEM images of the successfully fabricated microscaffold. The honeycomb microstructures of the microscaffold were intact over a large area after having been delaminated from a stamp, and the production yield of the microscaffolds was over 87%, which

was much higher than the production yield (~ 62 %) of the similar-sized ice cube tray PGS scaffolds. A detailed description of the fabrication process for photocurable PGS microscaffolds can be found in the experimental section.
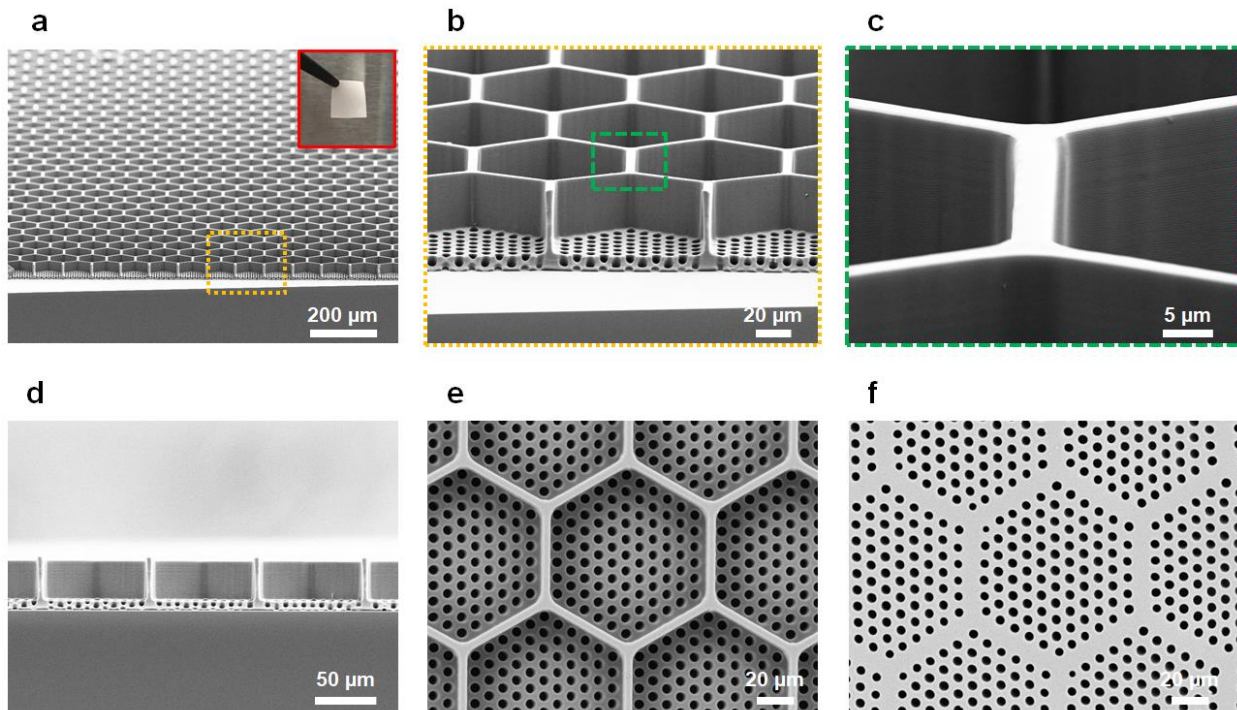
Figure 3.17. SEM images of the fabricated microscaffold: a) tilted view (the inset shows a low-magnification photographic image of the fabricated microscaffold held with a tweezer), b) magnified view of the scaffold, c) magnified view of the wall of a scaffold cell capture well, d) cross-sectional view, e) top view, and f) bottom view.

3.4. Cell seeding in photocured PGS microscaffolds

3.4.1. RPE cell seeding in scaffolds

In order to demonstrate the feasibility of the fabricated microscaffolds, cells were seeded in the scaffolds. First, to determine the optimal cell seeding density for the RPE layer, which is the

minimum number of RPE cells per transwell required to achieve the maximum cell carrying capacity of the scaffold while still leaving an appropriate well volume for subsequent PR seeding, laminin-coated scaffolds were seeded with RPE cell suspensions at different concentrations (4×10^5 and 7×10^5 cells per transwell) and cultured for 5 days. Figure 3.18 shows the microscopic images of the microscaffolds that were seeded with RPE cells. As shown in Figure 3.18a, uniform cell distribution was achieved by seeding at a concentration of 4×10^5 cells per transwell. On the other hand, when the scaffolds were seeded with a concentration of 7×10^5 cells per transwell, RPE cells started to aggregate each other (the dark area in Figure 3.18b).
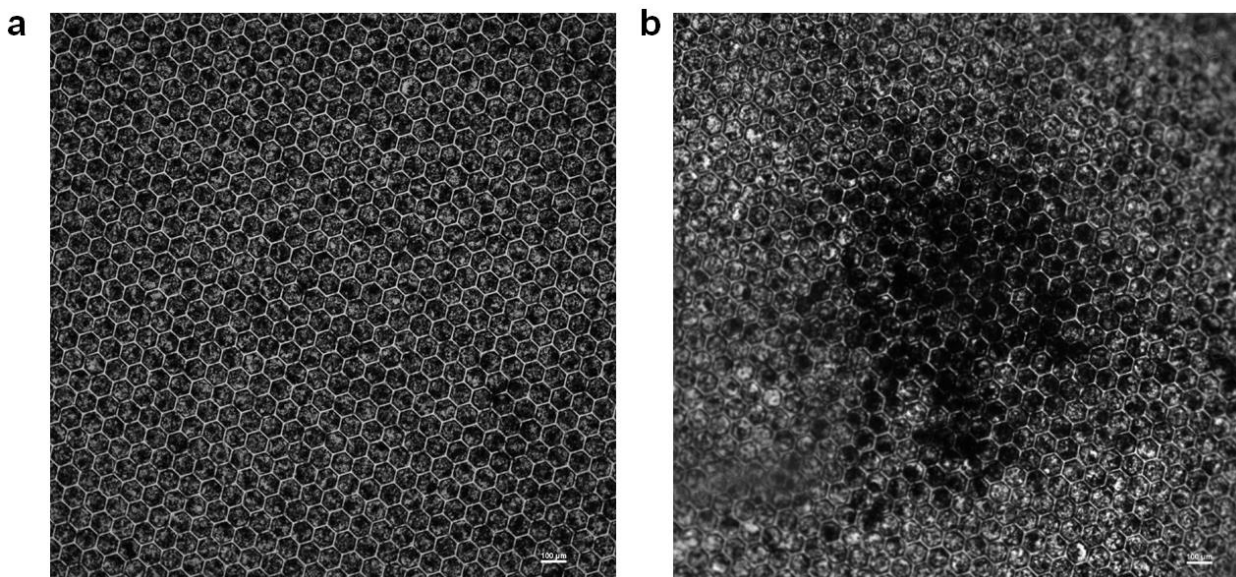
Figure 3.18. Microscopic images of the microscaffolds seeded with RPE cells at different concentrations: a) 4×10^5 RPE cells per transwell and b) 7×10^5 RPE cells per transwell.

Figure 3.19 shows the morphology of RPE cells visualized by immuno-fluorescent staining using RPE-specific markers (i.e., MITF, ZO-1). As shown in the Figure 3.19b, the RPE cells seeded on a scaffold were cultured in a highly organized fashion and formed a monolayer. The

morphology of the RPE cells was similar to that of the RPE cells seeded on a transwell (Figure 3.19a). Furthermore, as shown in Figure 3.19c, when the microscaffold was seeded with the concentration of 4×10^5 RPE cells per transwell, it had enough empty spaces on the top of the RPE cells for the subsequent PR seeding.
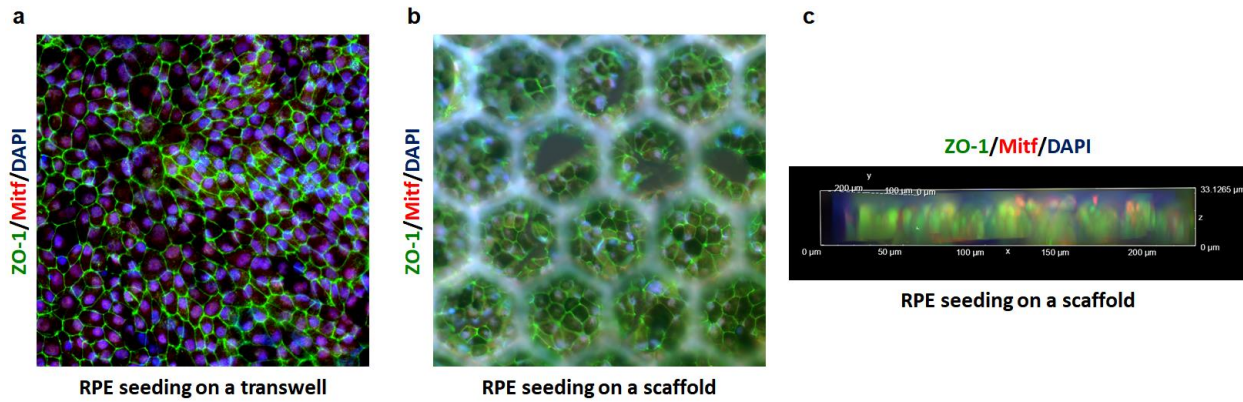
Figure 3.19. *Microscopic images of the RPE cell seeded on a) a transwell and b) a scaffold. c) A 3D lateral view of the scaffold demonstrating even distribution of RPE cells.*

3.4.2. Dual RPE+PR cell seeding in scaffolds

After optimizing the RPE cell seeding density, PRs were seeded onto the RPE monolayer in the scaffolds. Based on our preliminary study, two concentrations (1 million and 3.5 million PRs per transwell) were selected as potential optimal PR cell seeding densities and were tested. As shown in Figure 3.20a, when the scaffold was seeded with 1 million PRs per transwell, the PRs were uniformly distributed over the whole scaffold area. Contrastingly, when the scaffold was seeded with 3.5 million PRs per transwell, cell aggregations were observed in some areas of the scaffold (Figure 3.20b).
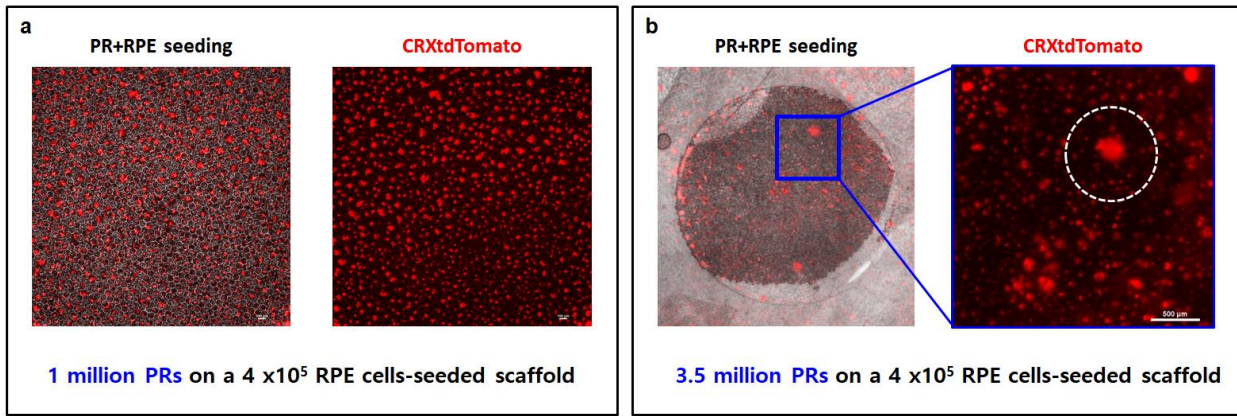
Figure 3.20. *Microscopic images of the microscaffolds seeded with a) 1 million and b) 3.5 million PRs per transwell on a RPE-seeded scaffold.*

Figure 3.21 shows the images of the microscaffolds seeded with 4×10^5 RPE cells per transwell followed by 1 million PRs per transwell attained via an immunofluorescent staining. Both cell types (PRs and RPE cells) were observed in each cell capture well of the microscaffold. Furthermore, both cells were uniformly distributed over the whole scaffold area. In order to determine whether the microscaffold facilitates the preorganization of hPSC-PRs within the scaffold constructs, PRs are currently being further cultured. As a future work, to assess PR polarity and scaffold construct organization, whole mounts of the microscaffold seeded with 4×10^5 RPE cells per transwell and 1 million PRs per transwell will be screened for the presence of (i) outer segments (specialized light-detecting structures situated apically within PRs) and (ii) presynaptic vesicles, which localize to the basal PR axon terminal. 3D reconstructions of scaffold flat mounts will also be analyzed to determine the primary location of outer segments and presynaptic terminals.
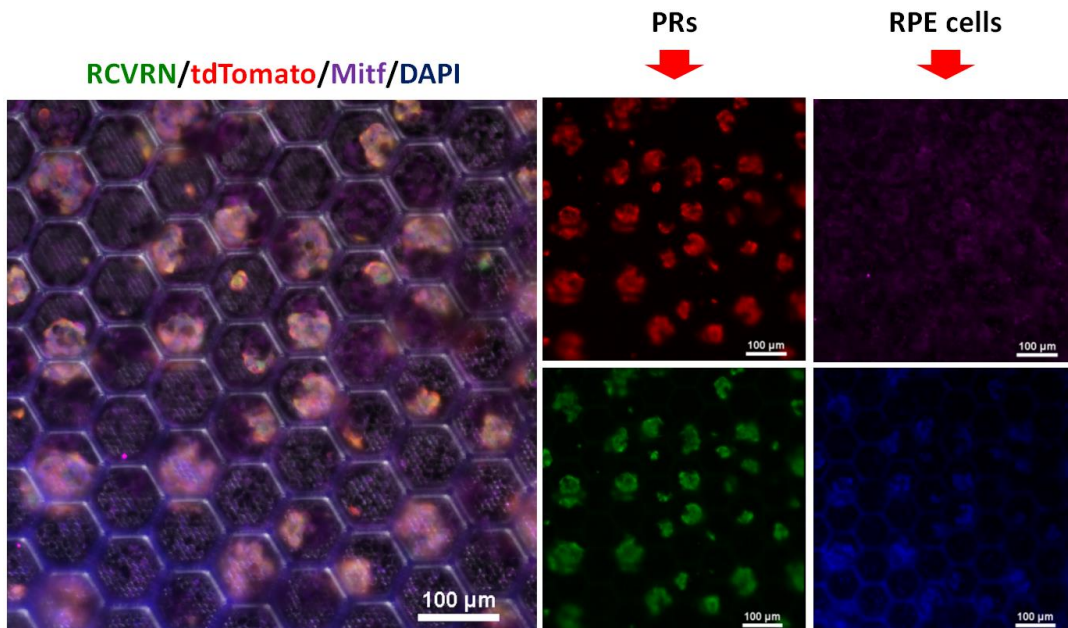
Figure 3.21. Microscopic images of the PR+RPE cells seeded on a microscaffold. Both cell types (PRs and RPE cells) are observed in the same scaffold wells through an immunostaining for RCVRN (PR-specific marker) and Mift (RPE-specific marker).

3.5. Experimental section

3.5.1. Fabrication of Si master

On a clean Si wafer, an array of hexagonal circle patterns for the fluid channels was defined using a photolithography (AZ2020) process and etched with a DRIE process. During the DRIE, etch/passivation cycles, etch/passivation time per cycle, plasma power, ICP power, and $SF_6/O_2/C_4F_8$ gas flows were 93/93 cycles, 10/5 sec, 11.7 W, 600 W, and 102/12/100 sccm, respectively. The diameter and depth of the etched fluid channels were 4.1 µm and 28.2 µm, respectively (Figure 3.6). After removing the photoresist on the Si wafer with organic solvents (i.e., acetone and isopropyl alcohol) and piranha solution, hexagonal grid patterns for the cell

capture wells were formed via a photolithography (AZ2070) process. During the photolithography, the processing time of UV exposure was 48 sec and the processing time and temperature of the post-exposure bake were 3 min and 120 ℃, respectively. After the development process of photoresist using a chemical developer (AZ 917) for 12 min (1 min 30 sec × 8 times, separately), a subsequent hard-bake (130 ℃, 2 min) was carried out to toughen the photoresist, so that it could endure against the plasma etching during the DRIE process without any loss. Then, a CF_4 plasma treatment (CF_4 gas, 40 mTorr, 250 W, 40 sec) followed by oxygen plasma treatment (O_2 gas, 120 mTorr, 100 W, 1 min) was conducted to remove any remaining organic contaminants on the surface of Si wafer. Thereafter, the cell capture wells were created by the same procedure that was utilized for generating the fluid channels, except for the DRIE etch/passivation cycles (104/104 cycles). After the DRIE, the Si master was cleaned with organic solvents and a piranha solution and treated with oxygen plasma for 20 sec at plasma power of 40 W, pressure of 120 mTorr, and O_2 gas flow rate of 20 sccm to remove the remaining organic contamination. Lastly, the fabricated Si master was coated with a Teflon-like polymer film, a chemically inert passivation layer, using a DRIE (C_4F_8 = 97 sccm, time = 1 min) to make the surface of the Si master hydrophobic.

3.5.2. Fabrication of PDMS stamp

A soft-PDMS precursor was first prepared by mixing and degassing 22.4 g of silicone elastomer base and 5.6 g of curing agent (Dow Sylgard 184 silicone elastomer kit). Then, the hard-PDMS was fabricated by mixing 6.8 g of vinyl PDMS prepolymer (VDT-731), 36 µL of a Pt catalyst (SIP6831.2LC), 100 µL of 2,4,6,8-Tetramethyl-2,4,6,8-tetravinylcyclotetra-siloxane,

and 2 g of a hydrosilane pre-polymer (HMS-301). Next, 7 g of the hard-PDMS precursor was poured into the prepared soft-PDMS, mixed for 7 min, and degassed in a vacuum desiccator for 10 min to remove bubbles from inside the hybrid-PDMS mixture. The mixture was then poured onto the resulting Si master and cured at room temperature for 12 hours, followed by an extra curing session in an oven at 60 ℃ for 2 hours. After curing, the hybrid-PDMS stamp (2 cm × 2 cm × 0.6 cm size) was peeled off from the Si master using a metal tweezer and cut with a razor blade to obtain four sets of 1 cm by 1 cm by 0.6 cm cubes. Then, the stamps were cleaned by gently spraying isopropanol onto their surface and carefully blow-dried with nitrogen. In order to facilitate a hydrophobic silane coating (anti-stick coating) in the next step, the stamps were pretreated with oxygen plasma using RIE (plasma power: 40 W, working pressure: 120 mTorr, flow rate: 30 sccm, and processing time: 20 sec). Thereafter, the opposite side of the stamps' micro-patterned surface was attached onto a glass slide to protect the surface of the opposite side from being covered by the silane coating for an efficient UV curing process of PGS through the stamps. Lastly, this apparatus (i.e. four stamps on a glass slide) was placed in a desiccator with 400 µL of trichlorosilane (SIT8174.0) and degassed for 12 hours at room temperature to allow the stamps' surface to be fully covered with evaporated silane.

3.5.3. Synthesis of PGS prepolymer

Equimolar glycerol (9.20 g, 100 mmol) and sebacic acid (20.2 g, 100 mmol) were added in a 100-mL Schlenk flask and mixed at 120℃ under nitrogen for 24 hours. Thereafter, the pressure was reduced to 0.1 atm for 30 minutes to evaporate the moisture, and further reduced to 1 mbar using the vacuum pump for 18 hours at 120℃ to allow polycondensation. The prepolymer was a

white wax-like solid after cooling down to 20°C and used for thermo-curing or following synthesis without any purification.

3.5.4. Synthesis of photocurable PGS prepolymer

PGS prepolymer (5.0 g, 19.4 mmol repeating units) was dissolved in anhydrous DCM (50 ml) containing 4-methoxyphenol (1000 ppm, 5.0 mg) and triethylamine (2.70 mL, 19.4 mmol). Methacrylic anhydride (1.44 mL, 9.7 mmol) was added dropwise (1-2 droplets/s) into the PGS prepolymer solution while stirring in an ice bath for 1 h. Then, the reaction was continued at 20°C in the dark for 24 h. An additional 4-methoxyphenol (1000 ppm, 5.0 mg) was added to the reaction solution. The reaction mixture was then repeatedly precipitated in diethyl ether (250 mL) and redissolved in DCM (50 mL) for three cycles. Thereafter, the crude product solution in DCM was washed with saturated brine (pH 3-4, adjusted with 1 M HCl) three times and dried with anhydrous $MgSO_4$ overnight with the existence of 4-methoxyphenol (500 ppm, 2.5 mg). After the removal of $MgSO_4$ and solvents, the photocurable PGS was collected and stored at −20 °C. The chemical structure of the photocurable PGS prepolymer was characterized by 1H-NMR (400 MHz, solvent: $CDCl_3$).

3.5.5. Fabrication of photocurable PGS microscaffolds

A tube containing photocurable PGS prepolymer blended with GMA (10 wt%) and DMPA (1 wt%) was placed in a vacuum oven (60 °C and <1 mbar) for 20 min in order to melt the photocurable PGS formulation. Then, approximately 10 mg of the mixture was put on a micro-patterned surface of four hybrid-PDMS stamps via a syringe and degassed in the vacuum oven at 60 °C for 30 min to remove bubbles inside the photocurable material. Thereafter, the stamp was

flipped over and then put against a clean Si wafer. Next, this apparatus (i.e., Si wafer, photocurable material, and stamps) was subsequently placed into the vacuum oven and degassed under a high vacuum (<1 mbar) at 60 ℃ for 1 hour to get rid of any bubbles between the stamps and the Si wafer. During this degassing process, the vacuum oven was vented with nitrogen gas every 10 min to facilitate the removal of bubbles. Then, a 5 by 5 inch quartz plate followed by weights totaling 3,120 g (Figure 3.22) were placed on the stamps at room temperature with the stamps' surface (i.e., the opposite side of the stamps' micro-patterned surface) unblocked by the weights for the UV curing process of the PGS through the stamps. Then, the whole apparatus was placed back into the oven at 60 ℃ for 10 min to liquefy the photocurable material, so that the fluid channels could be fully opened by the pressure caused by the weights. After that, the apparatus was placed into a UV curing chamber and cured by UV light (wavelength at 365 nm, 10 mW/cm^2) in a nitrogen atmosphere at room temperature for 1 hour to allow complete photocuring. After curing, the apparatus was left at room temperature for 12 hours to completely dry any remaining solvents in the photocured PGS that were not fully evaporated during the degassing and curing process. Then, the stamps were cut horizontally using a razor blade to make them thinner (i.e. ~ 1 mm thickness), so that, in the next fabrication step, the PGS scaffolds could be easily delaminated from the stamps by a sonication process in isopropanol where polymers are swollen. The apparatus was then immersed in isopropanol and sonication-treated for 4 hours. For the first 2 hours, both the PGS scaffolds and the stamps were detached together from the Si wafer, and for the last 2 hours, the PGS scaffolds were delaminated from the stamps. The delaminated PGS scaffolds were transferred onto a Teflon plate using a transfer pipet, and a few drops of DI water were applied onto the surface of the scaffolds to make the swollen scaffolds reinstate to their original shape. Finally, the PGS scaffolds were carefully blow-dried

with a nitrogen gas (Figure 3.23a).

Weight per stamp	Top view	Bottom view
740 g		
780 g (Optimized weight)		
820 g		
900 g		
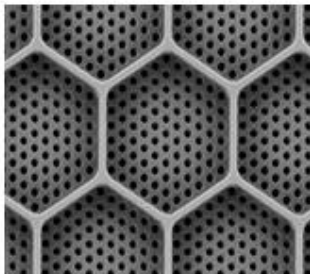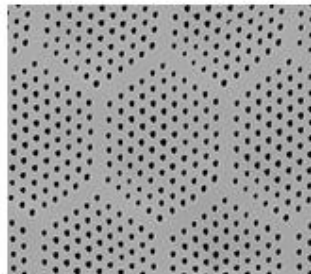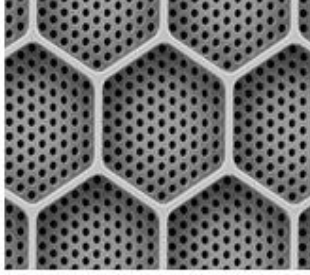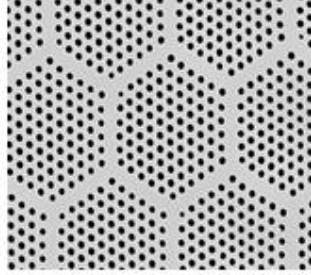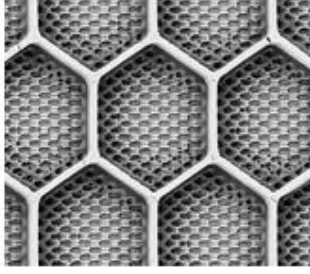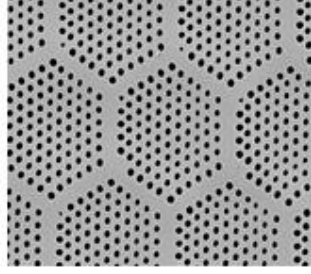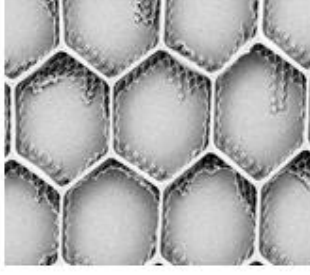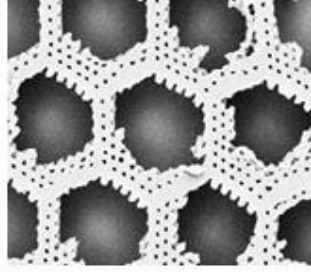
Figure 3.22. SEM images of the microscaffolds fabricated with different molding weights.
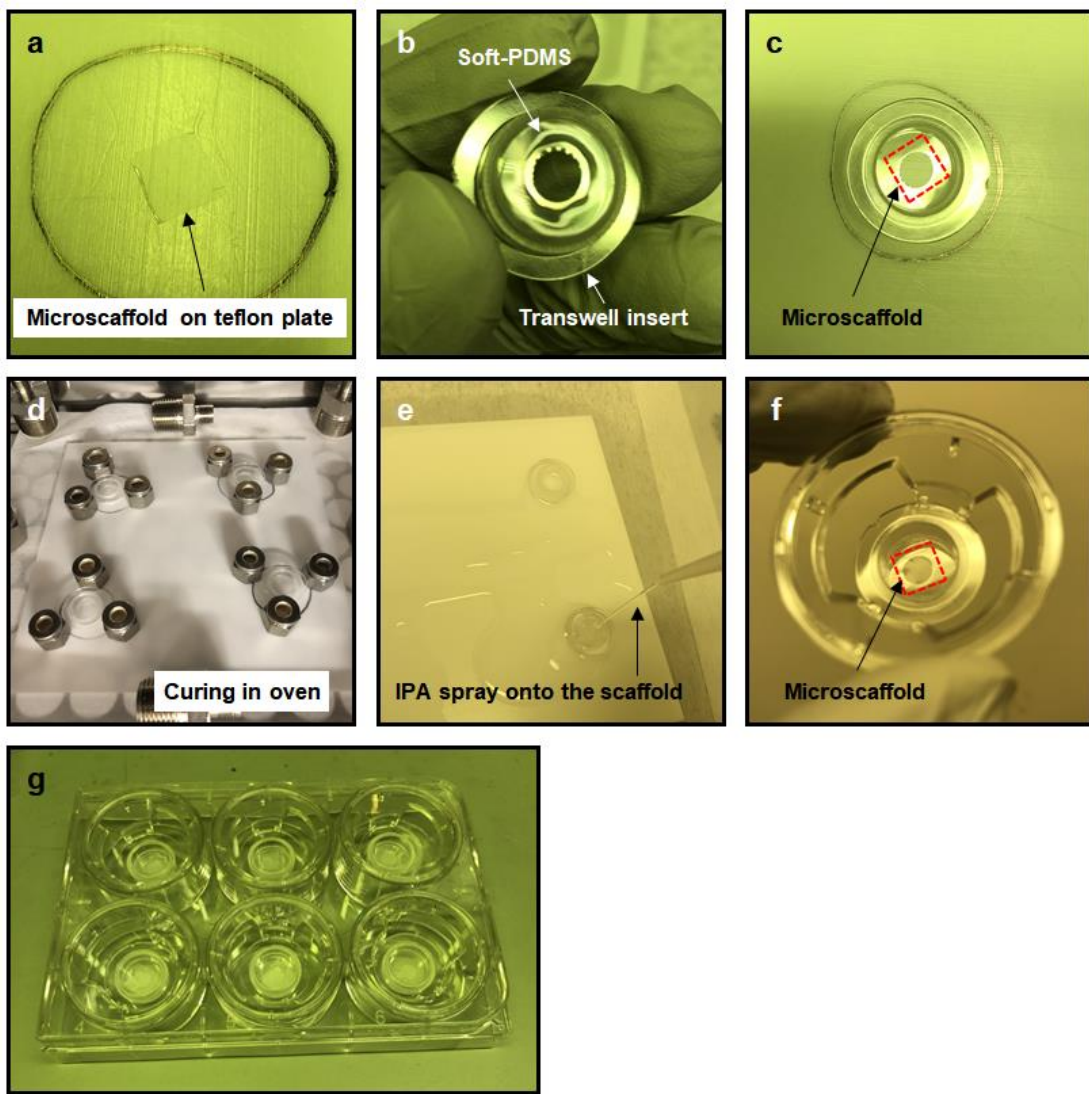
Figure 3.23. *Low-magnification photographic images showing the mounting process flow of a microscaffold on a transwell insert. a) 0.8 cm squared microscaffold placed on a Teflon plate, b) Liquid soft-PDMS is applied to the transwell insert along with the punched hole (5 mm in diameter or 19.63 mm^2). c) The transwell insert is placed onto the microscaffold on a Teflon plate and d) cured in an oven at 60°C for 4 hours. e) IPA solution is sprayed on the microscaffold for facilitating the detachment of the transwell insert and scaffold. f) The detached scaffold and transwell insert are embedded in a transwell insert holder and g) mounted on a 6-well cell culture plate.*

3.5.6. Mounting microscaffolds on transwell inserts

First, a thin porous polyester membrane of a transwell insert was punched using a biopsy punch with a diameter of 5 mm. Then, as a glue, liquid soft-PDMS was prepared by mixing the Dow Sylgard 184 silicone elastomer base and curing agent (4:1) and was applied to the transwell insert along with the punched hole (Figure 3.23b). Next, the transwell insert was aligned and placed onto the microscaffold prepared on a Teflon plate (Figure 3.23c) and then cured in an oven at 60 ℃ for 4 hours (Figure 3.23d). After curing, isopropanol was sprayed on the microscaffold to make it swollen (Figure 3.23e) and both the transwell insert and microscaffold were carefully detached from the Teflon plate. Then, the transwell insert was snapped into place in a transwell holder for cell culture use (Figure 3.23f). Figure 3.23g shows six microscaffolds mounted on the in vitro transwell co-culture system. In order to activate the scaffold surface and promote thorough laminin coating and uniform cell capture, brief oxygen plasma treatment (O_2 gas, 20 sccm, 120 mTorr, 40 W, 40 sec) was conducted on the top and bottom surfaces of the microscaffold.

3.5.7. Tensile test

The PDMS with different mixing ratios of the hard-PDMS to the soft-PDMS were made under the optimal curing conditions (25 ℃ for 12 hours followed by 60 ℃ for 2 hours) as films with ~1.8 mm in thickness, respectively. The films were then cut with a dumbbell-shaped (ASTM D638 Type V) die, with three replicates for each sample. Tensile tests were carried out using a pre-tension of 0.1 N and an extension rate of 10 mm min^{-1} (Instron, 5848, with a 50 N load cell). The stress-strain curves were recorded and Young's moduli were calculated.

3.5.8. Scaffold seeding and maintenance in culture

Stage 2 organoids (D120 of differentiation) were dissociated enzymatically with papain and seeded onto gas-sterilized scaffolds precoated with laminin 521 (human recombinant Laminin 521, BioLamina) in Hanks' balanced salt solution with calcium and magnesium for cell seeding experiment. Approximately 300 ul of RDM and 10% FBS were used to plate cells onto scaffolds. Scaffolds were kept undisturbed for the first 24 hours after seeding to promote cell adhesion, then progressively changed to RDM and 2% FBS media for scaffold maintenance. Scaffolds were cultured for up to 5 days and fed with RDM and 2% FBS on a daily basis.

3.6. Conclusion

In this work, the microfabrication and micromolding processes for creating the honeycomb-shaped outer retinal scaffolds that support the reconstruction of organized PR tissues in combination with RPE cells have been described. In order to generate the 3D complex honeycomb microstructures within a biocompatible and biodegradable PGS film, new microfabrication techniques and micromolding skills were introduced, and processing parameters and molding materials for the scaffold fabrication were further optimized. Moreover, it was demonstrated that the photocurable PGS, employed as a scaffolding material, drastically reduced the curing time of PGS from 3-4 days to just 1 hour and the honeycomb microstructures of the scaffolds substantially improved the production yield (~ 87 %) of the scaffold fabrication compared to the similar-sized ice cube tray PGS scaffolds (~ 62 %). The in-vitro cell seeding experiments demonstrated the feasibility of the microscaffolds acting as a delivery system for hPSC-derived PR+RPE bilayer. All the results reported in this study strongly support that the developed microscaffolds have a great potential to advance disease modeling and can provide

treatment options for patients with a wide range of macular injuries (e.g., blunt force or laser damage to the macula), as well as retinal degenerative diseases like AMD.

3.7. References

1.   Sharma, R., Bose, D., Maminishkis, A. & Bharti, K. Retinal pigment epithelium replacement therapy for age-related macular degeneration: Are we there yet? *Annual review of pharmacology and toxicology* **60,** 553-572 (2020).

2.   da Cruz, L. *et al.* Phase 1 clinical study of an embryonic stem cell–derived retinal pigment epithelium patch in age-related macular degeneration. *Nature biotechnology* **36,** 328-337 (2018).

3.   Jung, Y. H. *et al.* 3D microstructured scaffolds to support photoreceptor polarization and maturation. *Advanced materials* **30,** 1803550 (2018).

4.   Lee, I.-K. *et al.* Ultrathin micromolded 3D scaffolds for high-density photoreceptor layer reconstruction. *Science Advances* **7,** eabf0344 (2021).

5.   Jackson, M. J. Manufacturing High Aspect Ratio Microstructures. *Micro and Nanomanufacturing* 99-142 (2007).

6.   Paik, S. *et al.* Near-field sub-diffraction photolithography with an elastomeric photomask. *Nature communications* **11,** 1-13 (2020).

7.   Laermer, F., Franssila, S., Sainiemi, L. & Kolari, K. Deep reactive ion etching.   *Handbook of silicon based MEMS materials and technologies*. Elsevier, 2020, pp 417-446.

8.   Wang, Y., Ameer, G. A., Sheppard, B. J. & Langer, R. A tough biodegradable elastomer. *Nature biotechnology* **20,** 602-606 (2002).

9.   Rai, R., Tallawi, M., Grigore, A. & Boccaccini, A. R. Synthesis, properties and biomedical applications of poly (glycerol sebacate)(PGS): A review. *Progress in polymer science* **37,** 1051-1078 (2012).

10.   Yeh, Y.-C., Highley, C. B., Ouyang, L. & Burdick, J. A. 3D printing of photocurable poly (glycerol sebacate) elastomers. *Biofabrication* **8,** 045004 (2016).

11.   Yeh, Y.-C., Ouyang, L., Highley, C. B. & Burdick, J. A. Norbornene-modified poly (glycerol sebacate) as a photocurable and biodegradable elastomer. *Polymer Chemistry* **8,** 5091-5099 (2017).

12.   Pashneh-Tala, S. *et al.* Synthesis, characterization and 3D micro-structuring via 2-photon polymerization of poly (glycerol sebacate)-methacrylate–an elastomeric degradable polymer. *Frontiers in Physics* **6,** 41 (2018).

13.   Podgórski, M. Thermo-mechanical behavior and specific volume of highly crosslinked networks based on glycerol dimethacrylate and its derivatives. *Journal of thermal analysis and calorimetry* **111,** 1235-1242 (2013).

14.   Avci, D. & Mathias, L. J. Synthesis and photopolymerizations of new hydroxyl-containing dimethacrylate crosslinkers. *Polymer* **45,** 1763-1769 (2004).

Chapter 4. Conclusions and Future Directions

Tens of millions of people worldwide are affected by retinal diseases like AMD or have had accidents that permanently damage the light-sensitive PRs and/or RPE cells within their outer retinas that enable vision. As the human body is not capable of regenerating those cells and there are currently no treatments for restoring retinal tissue damaged by disease or trauma, there is a need for treatment options for retinal diseases which degenerate PR cells and ultimately lead to blindness.

In this dissertation, stem cell delivery scaffolds for regenerative therapy have been discussed. The goal was to engineer the stem cell delivery scaffolds for regenerative therapy using microfabrication and micromolding techniques. In chapter 1, background knowledge regarding degenerative retinal diseases, hPSC technology, current status of retinal cell replacement therapy, and 3D scaffold fabrication techniques have been reviewed. In chapters 2 and 3, "ice cube tray-shaped PR scaffolds" and "honeycomb-shaped outer retinal scaffolds" were discussed in detail. In these chapters, the specific aims were to 1) design the scaffold architectures, 2) fabricate the scaffolds using microfabrication (i.e., photolithography) and micromolding (i.e., soft lithography and replica molding processes) techniques, and 3) access the scaffolds in vitro using hPSC-derived PRs and/or RPE cells. The developed scaffolds offered several advantages that previously-designed scaffolds were not able to provide. To be specific, the ice cube tray-shaped PR scaffolds, presented in Chapter 2, had the highest-density capture of hPSC-PR cells among any other retinal scaffolds described to date and supported a substantially reduced biomaterial burden (i.e., 50% less than the previous wineglass design scaffold). Furthermore, the scaffolds exhibited optimal donor PR orientation for integration in transplantation studies. The honeycomb-shaped outer retinal scaffolds, described in Chapter 3, demonstrated the feasibility of

delivering a PR+RPE bilayer and also provided a remarkably high production yield of scaffolds over 85 %. We expect that these cell-scaffold composites will allow for controlled, precise, localized delivery of cells to the subretinal space and also will prevent or eliminate cell reflux and migration.

Future works will be aimed at evaluating scaffold-mediated delivery in small and large animal models of outer retinal disease and damage, exploring minimally invasive surgical approaches, and optimizing scaffold designs, materials, and manufacturing strategies for mass production and commercialization of the stem cell delivery scaffolds. For example, when it comes to the scaffold design, a two-tiered cell capture well design, as shown in Figure 4.1, can be considered as an alternative to further improve the production yield of scaffold fabrication by decreasing the aspect ratio of cell capture wells, and also to solve another potential problem, which is the partial mixing of PRs and RPE cells after plating; hence, some parts of the cells could not be physically organized well. With regard to this matter, the two-tiered cell capture well scaffolds can offer much more organized cell constructions by physically separating the layers of PRs and RPE cells. In addition, new materials also can be employed to visualize the scaffolds during surgery or transplantation. Since the PGS scaffolds are semi-transparent, it is difficult to localize them when loading into the transplantation device and during surgery where the scaffolds are placed in the subretinal space. Covalently conjugating a biocompatible dye onto the PGS prepolymer can provide visibility for the otherwise transparent scaffolds. The dyes which already have been approved for intraocular procedures, such as indocyanine green or fluorescein, can be selected and used for this purpose.

Once the performance of stem cell delivery scaffold is verified, cost aspects of producing a scaffold also should be taken into consideration for mass production and commercialization of

the scaffold. A scale-up of the scaffold's manufacturing process will be crucial for mass production and the fabrication of an unlimitedly reusable Si master will be the key for the successful commercialization of the scaffold because it takes up the greatest portion of costs in producing a scaffold. Further experiments to determine the optimal batch size for scaffold product need to be done.

Lastly, the microfabrication and micromolding techniques developed through this project can be used to create a diverse array of micro- and nanoscale structures with complex geometries to support cell transplantation elsewhere in the body beyond the retina. For instance, microfabricated scaffolds with highly organized microstructures can be utilized for the application of stem cell hair restoration which is an innovative hair transplant procedure that can encourage the growth of one's own, natural hair using human body's stem cells.
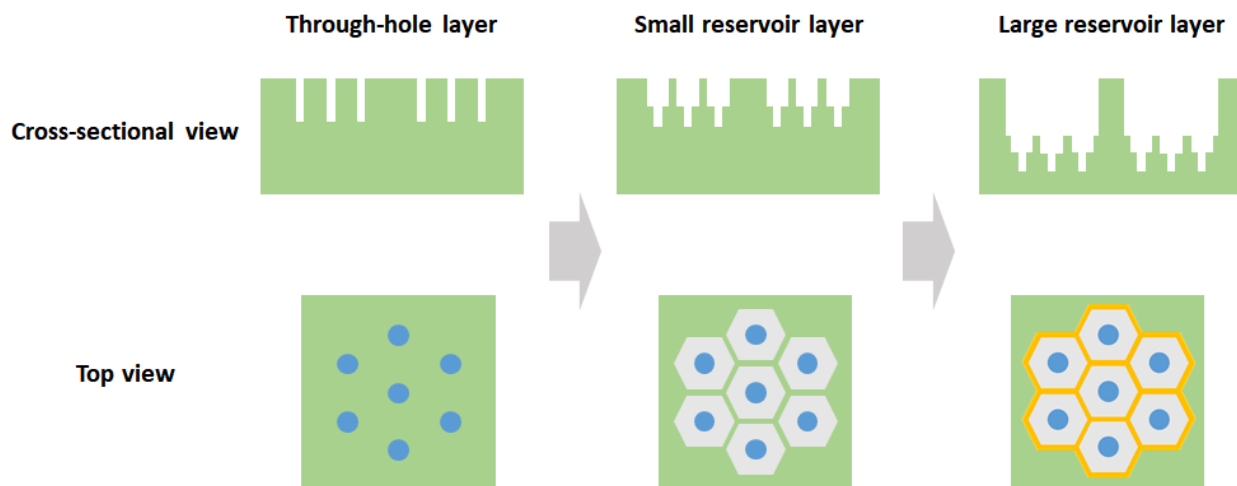

Figure 4.1. *Schematic illustration of the fabrication process for making a Si master of two-tiered cell capture well scaffolds.*